Abstract

HOFFMAN, BENJAMIN CARL. Electronic Disorder in Organic Semiconducting Films Observed with Kelvin Probe Force Microscopy. (Under the direction of Dr. Daniel Dougherty)

This work is a study into electronic disorder within organic semiconducting (OSC) films from a scan-probe perspective. Organic electronics are an exciting technology poised for use in next generation devices with unique applications such as transparent displays and ultrathin flexible solar cells. Understanding and mapping electronic disorder in OSC has a high degree of relevance towards recognizing the properties of charge trapping that hinders transport and diminishes device performance. Evidence of surface potential inhomogeneity is identified by using Kelvin probe force microscopy (KPFM) to measure the contact potential difference (CPD) between probe and sample. OSC films are grown via organic molecular beam deposition (OMBD) to create well-ordered crystals with precise control of nominal thickness. Further research methods involve the study of diffraction peaks from grazing-incidence wide-angle x-ray scattering (GIWAXS) for crystallographic analysis as well as use of a probe station for transfer characteristics of fabricated thin film transistors.

Initial research into this subject involved thin films of the novel organic molecule 2,8-diflouro-5,11-bis(triethylsilylethynyl)-anthradithiophene (diF-TES-ADT) that were grown on silicon substrates with a native oxide layer and analyzed with GIWAXS and KPFM. The crystallography of the films is that of a uniform (001) orientation. Variations in surface potential in diF-TES-ADT crystallites are observed to be unique from variations in the substrate.

Nevertheless, surface potential variations in thick films are influenced by chemical passivation of the substrate and so the source of CPD variations are assigned to be intrinsic defects. Chemical treatment and processing methods control the growth kinetics which are linked to charge traps locally distorting the surface potential in OSC films.

To continue the research into identifying charge trapping in ultra-thin films, 1.5 monolayer thick films of α-sexithiophene (6T) were grown on silicon substrates with a thick oxide layer to compare the surface potential of the first monolayer with that of the bilayer. The temperature of the substrate during film growth was varied and found to influence the interlayer surface potential contrast. Higher temperature samples have a bilayer with CPD above that of the monolayer, while lower temperature samples have a bilayer with CPD below that of the monolayer. GIWAXS data collected shows that the lower temperature sample has no observed out-of-plane order which we identify as the source of interlayer trapping formed between the first and second monolayers of the 6T films.

The final project into the specifics of disorder involves using ultrathin films of 6T in an operational transistor with grounded source-drain electrodes to study the influence of gate bias on surface potential. Using the mean and standard deviation of CPD for a series of gate biases, the trap density of states (DOS) is calculated directly while allowing for the quantification of spatial variations. CPD histograms from the series of images illustrate the screening of deep traps as the transistor is turned on. While in the ‘off’ regime the images are electrostatic, after transitioning to the ‘on’ state the images show instability after threshold voltage. This dynamic ‘on’ state offers a unique view of shallow trap states being filled and then thermally released.

© Copyright 2017 Benjamin Carl Hoffman

All Rights Reserved

Electronic Disorder in Organic Semiconducting Films Observed with Kelvin Probe Force Microscopy

by
Benjamin Carl Hoffman

A dissertation submitted to the Graduate Faculty of
North Carolina State University
in partial fulfillment of the
requirements for the degree of
Doctor of Philosophy

Physics

Raleigh, North Carolina
2017

APPROVED BY:

Daniel Dougherty Committee Chair	Harald Ade
Karen Daniels	Brendan O'Connor

Table of Contents

List of Figures ……………………………...………..………………………… v

Chapter 1: Background and Motivation ………………………………………. 1

Section 1.1: Introduction to Organic Semiconductors ……………………….……… 1

Section 1.1.1: Organic Molecular Solids …………………………………...…. 1

Section 1.1.2: Organic Semiconducting Devices …………………………..…. 5

Section 1.2: Charge Transport and Electronic Disorder …………………………… 9

Section 1.2.1: Organic Field Effect Transistor ………………….…………… 9

Section 1.2.2: Charge Transport in Disordered Systems ………….………. 15

Section 1.2.3: Trap States and Electronic Disorder ……….………..……. 19

Section 1.3: References ……………………………………………………………….. 23

Chapter 2: Experimental Methods and Instrumentation …………..…….. 26

Section 2.1: Scanning Probe Microscopy ……………………………………………. 26

Section 2.1.1: Atomic Force Microscopy ……………………………..…… 26

Section 2.1.2: Kelvin Probe Force Microscopy …………………….…….. 31

Section 2.1.3: Determining Trap DOS Using KPFM ……………………..… 34

Section 2.2: Film Growth …………………………………………………..……… 37

Section 2.2.1: Substrate Prep ………………………………………………… 38

Section 2.2.2: Transistor Electrode Fabrication ………………….……….. 41

Section 2.2.3: Organic Molecular Beam Deposition ………………….…….. 42

Section 2.3: Other Analysis Methods ……………………………………..…. 47

Section 2.3.1: Grazing-Incidence Wide-Angle X-ray Scattering …………... 47

Section 2.3.2: Probe Station ……………………………………..……… 47

Section 2.4: References …………………………………………..………… 49

Chapter 3: Intrinsic Charge Trapping Observed as Surface Potential Variations in diF-TES-ADT Films ………………………………….…… 50

Section 3.1: Introduction ………………………………………….………….. 51

Section 3.2: Experimental Methods ……………………………..…………… 55

Section 3.3: Results and Discussion ………………………………………..… 58

Section 3.4: Summary and Conclusions ……………………………..……… 66

Section 3.5: Supporting Information ………………………………….……….. 68

Section 3.6: References …………………………………………………….… 70

Chapter 4: Temperature Controlled Interlayer Disorder in Ultrathin Films of α-Sexithiophene …………………………………………..………… 75

Section 4.1: Introduction ……………………………………..………… 76

Section 4.2: Experimental Methods ……………………………..…………… 77

Section 4.3: Results and Discussion ……………………………….……… 79

Section 4.4: Summary and Conclusions ……………………………….……….. 86

Section 4.5: References ………………………………………………………………….. 88

Chapter 5: Shallow Charge Trap Instability After Transistion in a 2-Dimensional Organic Field Effect Transistor ……………..……………………….. 93

Section 5.1: Introduction ……………………….……………………………….……. 94

Section 5.2: Experimental Methods ……………………..………………….………… 98

Section 5.3: Results and Discussion …………………………………………….... 101

Section 5.4: Summary and Conclusions ………………..……………………………. 106

Section 5.5: Supporting Information …………………….………………………… 108

Section 5.6: References ……………………………….……………………….. 109

Chapter 6: Conclusions and Outlook ……………..………………………. 113

Section 6.1: References ……………………………….……………………….. 116

Appendix A: Glossary of Key Terms ………………………….………….. 119

Appendix B: MATLAB Code for DOS Analysis in Chapter 5 ………..… 123

List of Figures

Figure 1.1: Line diagrams for the small organic molecules pentacene and diF-TES-ADT taken from references [8] and [4] of Chapter 1 …………………………………………..……….……… 3

Figure 1.2: HOMO and LUMO bands separated by an energy gap describing a typical semiconducting material ………………………………………………….…..…………………. 5

Figure 1.3: Simple schematic of a bottom-gate contact OFET …….………….….…………….. 10

Figure 1.4: (Left) Transfer characteristics the 6T OFET featured in Chapter 5 with linear fit to determine mobility. (Right) Second derivative of transfer characteristics used to calculate threshold voltage ……………………………………………………………………………….. 13

Figure 2.1: Schematic diagram of amplitude modulation atomic force microscopy. This figure is taken from reference [2] of Chapter 2 ……………………………………………………….. 27

Figure 2.2: Photograph of the MFP-3D AFM used for sample topography and electrical characterization ……………………………………………………………………………… 29

Figure 2.3: Band diagram outline of classic Kelvin Probe. This figure is taken from reference [2] of Chapter 2 ……………………………………………………………………………….. 32

Figure 2.4 – Photograph of water droplet on bare substrate and substrate passivated with HMDS. Contact angle measurement is indicated with red lines ……………………………………... 40

Figure 2.5: (Left) Picture of shadow mask for Au/Cr deposition of source drain electrodes. (Right) Visible light microscope image (x5) of OFET channel ……………………………….. 41

Figure 2.6: Photograph of box chamber used for OMBD process. Photograph of crucible wrapped in tungsten wire ……………………………………………………………….… 43

Figure 2.7: (Left) Picture of substrate heater. (Right) Results of heater calibration under vacuum. The data is well fit by a power law ………………………………………………………..… 46

Figure 3.1: A characteristic GIWAXS result of a thick film (~ 100 nm) with HMDS-treated substrate. Simulated scatter points of known crystal orientation, displayed as red crosses, suggest a uniform (001) orientation ………………………………………………………………….. 58

Figure 3.2: (2 μm)^2 (a) topography and (b) surface potential images of diF-TES-ADT crystallites on a native SiO_2 substrate grown via organic molecular beam deposition. Part (c) is a histogram of surface potential image (b) with separate data sets of intensity for the substrate and the molecule. The points indicate the true data, while the solid line is a single Gaussian peak fit to the data ………………………………………………………………………………………. 59

Figure 3.3: Images (a) and (b) are topography scans, whereas (c) and (d) are surface potential images of complete diF-TES-ADT coverage of silicon substrate. Images (a) and (c) correspond to films grown on an untreated substrate, whereas (b) and (d) are films grown on a substrate treated with HMDS. All images display 1 μm scale bars ……………………………………… 61

Figure 3.4: Histogram of surface potential values for a set of compiled KPFM scans. The HMDS-treated substrate (untreated) data displayed by black (red). The boxes indicate the true data, while the solid line is a single peak Gaussian fit to these points ………………………… 63

Figure 3.5: Individual surface potential histograms that comprise Figure 3.4 in the main text. The data from each scan was distributed into 5 mV bins …………………………………..... 68

Figure 4.1: $(10\ \mu m)^2$ images (a) and (b) are topography and the corresponding surface potential scans are (c) and (d). The sample grown on 70 °C substrate are (a) and (c) while the 120 °C substrate sample is shown in (b) and (d) ………………………………………………………….. 80

Figure 4.2: In-plane GIWAXS data of 6T grown with different substrate temperatures; red data points for the 70 °C sample and black points for 120 °C sample. The blue lines indicate the values associated with the β and LT (020) phases of 6T ………………………………………. 82

Figure 4.3: 2D WAXS data associated with the 70 °C sample (a) and the 120 °C sample (b) .. 83

Figure 4.4: (a) and (b) are histograms of surface potential data shown in figures (1c) and (1d), respectively, with data separated between the 1st and 2nd monolayers. (c) and (d) are schematics of the proposed model to explain the shifts in surface potential …………………..………… 84

Figure 5.1: (a) Schematic of bottom-gate contact transistor geometry with AFM probe. (b) Transfer curve demonstrating operational transistor with measured threshold voltage. (c) Example topography image from featured scan series ………………………………...……. 98

Figure 5.2: Observed surface potential at a given gate bias dependence relative to threshold voltage. The black data points are the mean and standard deviation of each individual KPFM scan. The red line is the exponential DOS fit described in Equation 5.4. The inset graph is the DOS computed directly from the average CPD values using Equation 5.2 ………………….. 101

Figure 5.3: (a) Extended graph of measured average surface potential at each gate bias. (b) Compiled histograms of 20 images, each, where the green (blue) points correspond to the green (blue) highlighted points in (a). (c) and (d) are representative $(8\ \mu m)^2$ surface potential images matching the red and yellow diamonds in (a), respectively ………………………………..….. 103

Figure 5.4: (a), (b), and (c) are 10x40 μm^2 images of topography, phase, and CPD, respectively, characterizing the length of the OFET channel at $V_G = 0V$ ……………………………….…. 108

Chapter 1

Background & Motivation

1.1 Introduction to Organic Semiconductors

1.1.1 Organic Molecular Solids

Our advances in electronic technology build on previous work, making the rate of change that these developments occur exponential (ergo Moore's Law). Technology has become inseparable from our everyday lives. It seems ever more apparent that this progress has not reached its end. As our consumption of energy and resources expands to meet the need of an ever more technologically advanced society, those concerned with the future often question the sustainability of the path that we are on. The study of organic molecular systems has already garnered much excitement for its possibilities in low-energy device fabrication, and is becoming integrated into such diverse fields as physics, chemistry, material sciences engineering, and even textiles and manufacturing. My goal with this research is to better understand the origins and influences of charge trapping, with an eye to optimizing charge transport, in the hopes of furthering the viability of sustainable manufacturing using organic products.

Usage of the word organic is a direct reference to the field of organic chemistry where many advances in molecular synthesis have been made. These advances are foundational for the development of new materials. Organic molecules are typically made from elements belonging to the first two rows of the periodic table, particularly C, N, S, and O. Materials from assembled

organic molecules are held together by weakly bound, noncovalent interactions. One example of the complexities introduced by these weakly bound molecules is that free electrons in these materials are not observable as discrete particles as one might imagine. Their existence cannot be decoupled from their surrounding environment. This can be understood by considering a single extra charge added to the center of a molecular lattice. The orbitals in near proximity polarize with the new field inhibiting the charge's mobility and increasing its effective mass. This free electron can now be described as a quasiparticle polaron.[1]

The most defining characteristic used in organic molecular systems is π-conjugation which enables charge carriers to become delocalized. In terms of chemical line diagrams π-conjugation is depicted as alternating single and double bonds, but in actuality what is occurring is more of a sharing of bonds where different atoms each contribute equally. An illustrative example to understand the concept of π-conjugation is the simple benzene ring. At the core of its molecular structure is 6 carbon atoms, each with three sp^2 hybridized orbitals and a remaining p_z orbital. The three sp^2 orbitals extend out in planar fashion 120° relative to one another and form σ-bonds with their nearest neighbors, two carbon atoms and a hydrogen atom. The remaining p_z orbital at the site of each carbon atom has two lobes that stick out perpendicularly to the σ-bonds. Each of these p_z orbitals overlaps with its neighbor on either side and, in this way, they all form a bond across the entire molecule. Charges shared with these overlapping p_z orbitals form π-bonds and are considered to be delocalized; this is π-conjugation. Structures like this are often referred to as aromatic and are considered to be very stable. With charges delocalized across each molecule, the next step is to consider two benzene rings stacked parallel. Now the π-bonds from

each benzene ring overlap with the neighboring molecule to form a π-π stack allowing charges to hop from one molecule to the next. Improving the π- π interaction between molecules is a major mission for optimized charge transport over multiple molecules. These are the basic ideas behind how conduction is possible in these organic molecule and polymer systems.

Another relevant species of organic molecule worth mentioning at this point is the thiophene structure. Similar to benzene with the exception of a sulfur atom substituted for two of the carbon atoms. Thiophene is the basic structure in molecule α-sexithiophene (6T) and also the widely-used polymer poly(3-hexylthiophene-2,5-diyl) (or more commonly known as P3HT). For detailed coverage of the properties of 6T and relevant literature, see the studies described in Chapter 4 and 5. DiF-TES-ADT, the subject of Chapter 3, also has two thiophenes as part of its molecular structure.

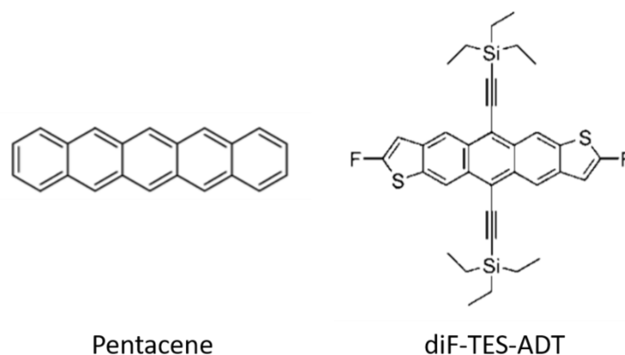

Figure 1.1: Line diagrams for the small organic molecules pentacene and diF-TES-ADT taken from references [9] and [5] of Chapter 1.

The design and modification of organic molecules towards specific purposes and bulk properties involves methodical experimentation. Consider the two molecular structures depicted in Figure 1.1; pentacene and diF-TES-ADT. Using organic chemistry to optimize organic

molecules can traced through the evolution from pentacene to the creation of diF-TES-ADT (short for 2,8-diflouro-5,11-bis(triethylsilylethynyl)-anthradithiophene). The latter molecule was designed by Dr. John Anthony et al.[2] and is illustrative on how molecules can be carefully designed to improve devices. This not the only organic molecule consciously designed to fit a specific purpose, but it is illustrative of the process and is the species studied in Chapter 3. In this picture, one begins with the small molecule pentacene, which has been the subject of numerous studies. Bulky sidechains are added to the molecular structure to improve the solubility for eased processability.[3] Another function of these sidechains is to inhibit edge-to-face molecular interactions. Face-to-face molecular interactions are preferred for the bulk crystal structure due to increased π-orbital overlap. After adding bulky sidechains to the molecular structure, the pentacene backbone of the molecule is then replaced with anthradithiophene which was shown to dramatically increase carrier mobility.[4] Finally, the anthradithiophenes are fluorinated on one end in order to further enhance the rapid crystallization necessary for solution based deposition[2]. Each of these molecular substitutions are systematically tested and shown to increase the desired device characteristics. The final product is a robust molecule that has been studied in single crystal[5] and spun-cast[6] thin-film transistors. Further iterations from John Anthony's lab are still being actively studied by the organic electronics community.[7]

The configuration of the valence electrons is often the defining characteristic of the properties of a bulk material. Regardless, to date there is no tractable general formula to describe the bulk electronic properties of a material based on its constituent molecules. This is confounded by the plethora of possible molecules that can be designed and created. One need

only consider a few review articles[8, 9] of the organic electronics field to see how many molecules and their derivatives are being actively studied. This wide variety of molecules implies near infinite possibilities for the interplay of electronic and geometric structure. What seems at first an insurmountable problem is actually an opportunity for incredible discovery and design. Every aspect of the development of these materials from their fabrication processes to their final device properties can be tuned to specification.

1.1.2 Organic Semiconducting Devices

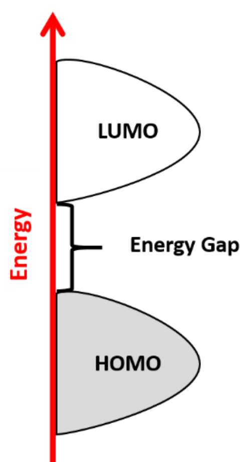

Figure 1.2: HOMO and LUMO bands separated by an energy gap describing a typical semiconducting material.

What defines a semiconductor is the position of the Fermi level with respect to the energy bands of the material.[10] Consider the band diagram depicted in Figure 1.2. For inorganic semiconductors, these two bands are called the valence and conduction band. For organic semiconducting (OSC) materials, the bands are more accurately described as the highest occupied molecular orbital (HOMO) and lowest unoccupied molecular orbital (LUMO). In

between the two bands is an energy gap, or band gap, that is energetically unfavorable for electrons to occupy. A metal has a Fermi level that is positioned within an energy band, therefore the charges are not locked into specific states. This gives energy space available for electrons to move in and flow freely through the material. Insulators have a Fermi level positioned in between energy bands so that charges are locked into specific states and a great deal of energy is involved to excited. Semiconductors also have a Fermi level in the band gap, but the band gap is smaller than in a traditional insulator. This allows for the Fermi level to be manipulated, usually by an applied field, and moved into one of the bands, changing the electronic properties from an insulator to a conductor. For semiconducting devices, the Fermi level is usually not in the center of the band gap, but closer to either the HOMO or the LUMO so that the conduction can be induced with a low field. If the Fermi level is close to the HOMO (LUMO) then the material is commonly identified as p-type (n-type), respectively. This terminology is adapted from the field inorganic semiconductors which are frequently doped with impurities to adjust their electronic properties. OSC films often have a Fermi level that is close to the HOMO or LUMO without having to intentionally dope the material. Both n-type and p-type OSC films are possible depending on the chosen molecule. P-type is the more studied of these two and used for the more detailed studies that make up Chapters 3-5. Ambipolar OSCs are also possible, where the band gap is small enough to access either the HOMO or the LUMO.

Among the possible commercial applications of these OSC materials are sensors, displays, imagers, and complex logic circuits.[11] Device application is among the most significant reasons behind the motivation to develop our understanding of these materials. Among the many

OSC devices that are being studied actively in research labs only those most relevant to this work will be described here.

Transistors are the building block for modern electronics. The transistor itself is a device with, usually, 3 terminals; source, drain, and gate. Source and drain are contacts across which current can be passed and the crucial third electrode, the gate, controls the on or off states of the transistor. If no gate bias is applied, then the transistor is considered to be off and *no current* can pass between the source and drain. If instead a sufficient gate bias is applied, then the transistor is turned on and *current can* be conducted between the source and drain. Transistors using OSC materials can be made using an ultrathin active layer. In fact, complex circuits using only a single monolayer of organic molecules as the active channels have been made in recent years.[12] OSC transistors are particularly useful to study transport physics, but their commercial value is for conjoined use with light-emitting diodes to create displays that completely use organic materials. A more thorough treatment of organic field effects transistor operational principles is given in section 1.2.2.

Some of the most attractive OSC devices for commercial production are optoelectronics. These devices are based around the conversion of electricity into light - organic light-emitting diodes (OLEDs) - or of light into electricity - organic photovoltaics (OPVs). Both OPV and OLED systems usually involve the interplay between more than one molecule species. In an OPV device the driving physical phenomena is the photovoltaic effect where an incoming photon excites a charge from the HOMO to the LUMO. This process creates an exciton, an electron bound to a hole, that must be dissociated for the charge to be able to escape to the

electrodes. Much study is focused on mitigating recombination which lowers the power conversion efficiency of OPV devices.[13] OLEDs on the other hand work towards enhancing recombination.[14] The physical process driving their functionality is photoluminescence, where charges are introduced into the active layer which then emits photons. Although OPVs and OLEDs are not studied specifically in this work, the focus is on fundamental charge trapping and electronic disorder of OSC material, which makes it applicable to any OSC device operating from charge transport. Furthermore, when it comes to using OSC materials for devices, it is these devices that yield the most excitement for commercial applications.

OSC materials are not destined to be sole replacement for the silicon base that our modern electronics are designed with. Instead they have the potential to be a supplementary material to suit specific needs. Carrier mobility of inorganic semiconductors far surpasses that of the most sophisticated OSC due to weak π-orbital overlap between molecules compared to more electronically coupled ionic bonds. What OSCs *can* offer to the commercial market is advances in large-area displays, solid state lightning, structural flexibility, and low-energy fabrication processes. The low-energy processability of these materials is a point that attracts many to this topic.[15] Since many of these materials are solution processable the method of fabrication involves low temperatures and can be designed for large area deposition. Active study into solutions for fabrication, such as hydrocarbon solvents for OPV fabrication[16], shows how the tunability of the fabrication parameters can be developed with the parallel goals of being economically viable and also oriented towards a sustainable energy future. Nevertheless, commercial viability is still limited by the fundamental complexities of charge transport in these

systems and also their degradation in air and sensitivity to water which leads to short operational lifetimes.[17] It is the former point that further study of electronic disorder can address.

1.2 Charge Transport and Electronic Disorder

A major problem in charge transport is the loss of energy through a medium. This energy loss is amplified by charge trapping (also known as electronic disorder), which catches charges as they traverse a field and allows for the energy to dissipate before it reaches its endpoint. Transport in Organic Semiconducting materials (OSCs) specifically is dictated by weak interactions between molecules and subject to high levels of electronic disorder. My research is a study into the fundamental mechanics of charge trapping in OSCs. Further understanding of the condensed matter physics informs better methodology to develop devices.

1.2.1 Organic Field Effect Transistor

Organic field effect transistor (OFETs) are important devices for the field in that they are ideal for studying charge transport but also because they are the key component in circuits to be used commercially. There are many different geometries that organic transistors can be made into, but the one used for this work, particularly in Chapter 5, is the bottom-contact style where source and drain electrodes are deposited onto a dielectric interface and then the active layer is deposited after.

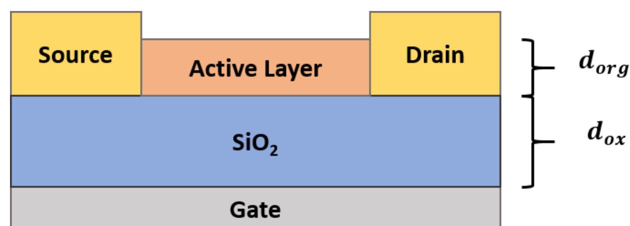

Figure 1.3: Simple schematic of a bottom-gate contact OFET.

Figure 1.3 shows the common bottom-gate contact OFET geometry. Source and drain electrodes are deposited onto the dielectric interface. The active layer is composed of the organic semiconducting film that spans from source to drain and is deposited on top of the insulating dielectric, often SiO_2. The gate electrode is opposite the active layer across this dielectric. Channel length is defined as the span between these two electrodes as depicted in Figure 1.3 and the width of the channel is perpendicular to this length. Similar to the description in section 1.1.2, the active channel accumulates charge when a sufficient gate bias is applied which creates a conducting channel allowing current to flow from source to drain.

It is important to realize that when a transistor turns on it is *not* the bulk of the active layer that percolates charges from source to drain. Charges in the channel induced by the gate are concentrated in close proximity to the dielectric, primarily in the first layer, and any molecules further than a few monolayers from this interface do not contribute to charge transport in any observable way. Consider the work by Dinneli et al. where layer by layer growth of α-sexithiophene was analyzed with respect to the observed mobility of a transistor[18]. In their study, they found charge mobility can be measured even when there is less than one monolayer of coverage, presumably because there can be percolation pathways accessible to charge carriers even without complete coverage, and there is an increase in mobility with respect to coverage

until around the completion of the second monolayer. With the addition of subsequent layers, measured out to 10 monolayers, the average mobility remains unchanged. It is this understanding of charge transport occurring near the interface which enables active layers that are only a single monolayer in thickness. From a scanned probe perspective, it also makes paramount the study of ultrathin films as to best observe the mechanics behind charge transport in OFETs.

There is a wide variety of different techniques to characterize transistors with novel experiments always being developed. There are two common I-V curves that are shown to depict the characteristics of an operational OFET; output characteristics and transfer characteristics[1]. Output characteristics are obtained by applying a constant gate voltage and then varying the drain-source voltage. It is from the output characteristics that the separation between the linear regime and saturation regime is defined. Transfer characteristics are obtained by applying a constant drain-source voltage and then varying the gate voltage. Carrier mobility and threshold voltage are the most common two parameters that are extracted from transfer characteristics. The following will outline common methods to obtain these parameters.

Carrier mobility is often thought of as the primary quantity of value when it comes to characterizing an OFET. Almost without exception, the carrier mobility is expressed in the units cm^2/Vs. The most common equation, to be derived in the following, to extrapolate mobility from an I-V curve has a very succinct form. This should not misrepresent the fact that our current understanding of the charge kinetics involved is still considered incomplete and this mobility approximation is popular for it ease of use, not for its complete generality. Only the linear regime will be considered here because it is the regime more relevant to later chapters. A similar

derivation of mobility for the saturation regime can be found in the seminal work on semiconductor device physics by Sze and Ng[19]. A simple formula for carrier mobility is easily derived through expressing the current flow from source to drain,

$$I_{DS} = \frac{Q}{t}(WL) \qquad (1.1)$$

where Q is the area charge density, t is the travel time of the charge, W is the width of the channel, and L is the length of the channel. Next, the electron mobility in solid-state physics is defined by the equation,

$$v_{drift} = \frac{L}{t} = \mu\,\mathrm{E} = \mu\,\frac{V_{DS}}{L} \qquad (1.2)$$

$$t = \frac{L}{\mu\,\mathrm{E}} = \frac{L^2}{\mu\,V_{DS}} \qquad (1.3)$$

where v_{drift} is the average drift velocity of the charge, μ is the mobility, and E is the applied field. The next consideration is that the charge, Q, is formed by the gate bias, V_G, applied across the dielectric in terms of capacitance.

$$Q = C_{ox}(V_G - V_{th}) \qquad (1.4)$$

where C_{ox} is the capacitance of the oxide, and V_G is offset by the threshold voltage, V_{th}. Equations 1.3 and 1.4 can now be substituted into equation 1.1 to arrive at the expression,

$$I_{DS} = \frac{W}{L} C_{ox}\mu(V_G - V_T)V_{DS} \qquad (1.5)$$

A more thorough derivation of the source-drain current yields the following well-known equation[19],

$$I_{DS} = \frac{W}{L} C_{ox}\mu[(V_G - V_T)V_{DS} - \frac{{V_{DS}}^2}{2}] \qquad (1.6)$$

Which simplifies to the same as Equation 1.5 with the assumption that $V_D << (V_G - V_{th})$. The final step to calculate mobility is to take the derivative of I_{DS} with respect to V_G in order to calculate the transconductance[19], which assumes that the V_{DS} is fixed.

$$g_m \equiv \frac{\partial I_{DS}}{\partial V_G} = \frac{W}{L} C_{ox} \mu V_{DS} \qquad (1.7)$$

or

$$\mu = g_m \frac{L}{W} \frac{1}{C_{ox} V_{DS}} \qquad (1.8)$$

Several major approximations involving uniformity of charge were made to derive this expression for mobility which may not be precisely accurate. Regardless, this is a very common equation for calculating mobility from transfer characteristics perhaps more than anything for its ease of use. One needs simply know the geometry of the transistor bed, measure the transfer characteristics, fit a linear slope to the data, and then compute a mobility.

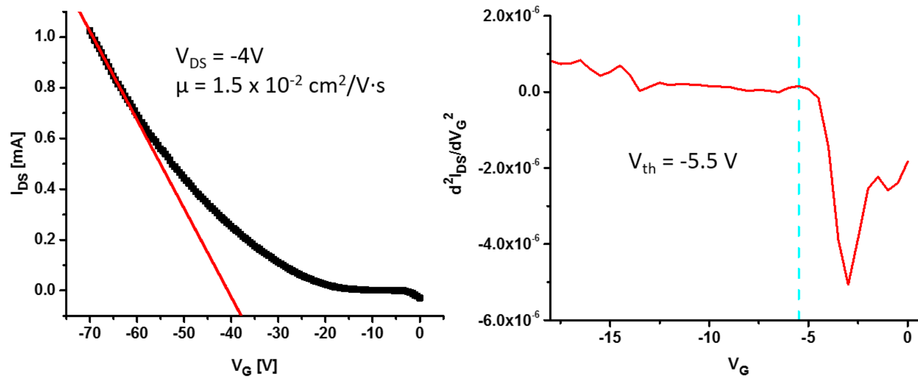

Figure 1.4: (Left) Transfer characteristics the 6T OFET featured in Chapter 5 with linear fit to determine mobility. (Right) Second derivative of transfer characteristics used to calculate threshold voltage.

Figure 1.4 (Left) shows a typical transfer curve, taken from a sample used for Chapter 5, with a linear fit incorporated to calculate mobility. From the over-simplified assumptions underlying this method for calculating mobility, researchers tend to overestimate the true mobility of the OFET.[20] This is a contentious subject in the community and in the future more accurate mobility models will need to be developed.

Threshold voltage is another very important parameter for modeling transistor characteristics. A brief definition of threshold voltage is the gate bias beyond which a conducting channel forms in the active layer.[1] There are many different methods with which to extract the threshold voltage of a FET[21] and they all calculate slightly different values even for the same transistor. There seems to be little agreement in the device community on the best way to calculate threshold voltage or even what the threshold voltage physically means[22]. Common methods include assigning an arbitrary current, extrapolating linear fits, taking integrals, and other exotic functions.[21]

For the purposes of my work, the second-derivative method appears to be the most successful at accurately determining the threshold voltage[23]. The idea with this method is to track the rate change of the transconductance with respect to gate bias and identify the maximum value. The gate bias at the value is identified as the threshold voltage. To put it simply, take the second derivative of a transfer curve and look for the first, largest peak after 0V. See Figure 1.4 (Right) for an example using a 6T FET used for Chapter 5. This method is fairly consistent for calculating reasonable threshold voltages, but the second-derivative output is very noisy and one

could easily misidentify the correct threshold voltage if they do not have another method to cross analyze with.

1.2.2 Charge Transport in Disordered Systems

With the basic understanding of how charges can become delocalized across a molecule, covered in Section 1.1.1, the next step is to better understand how these individual molecules that are weakly bound to one another can transfer charge over great distances. What follow here are some the fundamental transport models necessary to understand how charges travel in disorder OSC materials.

The tight binding model is a simple quantum mechanical approach that leads to the basic physics behind why charge transport in a weakly bound system is possible. For brevity, only the 1-dimensional solution will be derived here. Similar methods can be applied to derive higher dimension solutions, but the implications of this formalism are the same. The proof begins by considering a 1-dimensional chain of interacting orbital sites, defined by the displacement vector R, where only the two directly adjacent orbital sites influence the wavefunction at each site. It should be clarified that these adjacent lattice points may interact through the Hamiltonian, but we will assume that the wavefunction of each individual point is orthogonal to only itself. This nearest neighbor and tight-binding approximation is one of the major assumptions that this proof will make, the other is that the chain of molecules has a regular periodicity, defined by the lattice constant a, in their relative positions in space. If we consider an independent electron in a crystal lattice of ions represented by the Schrodinger equation with a periodic potential then the wavefunction can be expressed as a Bloch wave with the form,[10]

$$|\,\psi\,\rangle \;=\; e^{ikR_i}\sum_i |\,\phi_i\,\rangle \qquad (1.9)$$

By assuming that only the nearest neighbors contribute to the wavefunction at any given lattice site, we can expand the wavefunction according to:

$$|\,\psi\,\rangle \;=\; e^{ik(R-a)}\,|\,\phi_{(R-a)}\,\rangle + \; e^{ikR}\,|\,\phi_R\,\rangle + \; e^{ik(R+a)}\,|\,\phi_{(R+a)}\,\rangle \qquad (1.10)$$

Let us now consider the time independent Schrodinger equation projected onto a single lattice site, ϕ_R,

$$\langle\,\phi_R\,|\,\widehat{\mathrm{H}}\,|\,\psi\,\rangle \;=\; \langle\,\phi_R\,|\,\mathrm{E}\,|\,\psi\,\rangle \;=\; \mathrm{E}\,\langle\,\phi_R\,|\,\psi\,\rangle \qquad (1.11)$$

The right-hand side of equation 1.11 simplifies with our assumed wavefunction, equation 1.10, and the tight binding assumption that only the wave function is spatially localized.

$$\langle\,\phi_R\,|\,\psi\,\rangle \;=\; e^{ik(R-a)}\,\langle\,\phi_R\,|\,\phi_{(R-a)}\,\rangle + \; e^{ikR}\,\langle\,\phi_R\,|\,\phi_R\,\rangle + \; e^{ik(R+a)}\,\langle\,\phi_R\,|\,\phi_{(R+a)}\,\rangle$$

$$\mathrm{E}\,\langle\,\phi_R\,|\,\psi\,\rangle \;=\; \mathrm{E}\left[\,e^{ik(R-a)}\,(0) + \; e^{ikR}\,(1) + \; e^{ik(R+a)}\,(0)\right] = \mathrm{E}\,e^{ikR} \qquad (1.12)$$

The left-hand side of equation 1.11 does not simplify quite so succinctly unless the exact Hamiltonian is defined. We can circumvent this problem by identifying the physical meaning of the wavefunction overlap and substituting place holder values for empirically observable parameters. The two substitutions will be termed the on-site energy, α, and the transfer or hopping integral, β.

$$\alpha \;\equiv\; \langle\,\phi_R\,|\,\phi_R\,\rangle \qquad (1.13)$$

$$\beta \;\equiv\; \langle\,\phi_R\,|\,\phi_{(R-a)}\,\rangle \;=\; \langle\,\phi_R\,|\,\phi_{(R+a)}\,\rangle \qquad (1.14)$$

We can now expand the left-hand side of equation 1.11 with the assumed waveform equation 1.10 and substitute in these new terms.

$$\langle \phi_R \mid \hat{\mathrm{H}} \mid \psi \rangle = e^{ik(R-a)} \beta + e^{ikR} \alpha + e^{ik(R+a)} \beta = e^{ikR} \alpha + e^{ikR} \beta (e^{-ika} + e^{ika})$$

$$\langle \phi_R \mid \hat{\mathrm{H}} \mid \psi \rangle = e^{ikR} \alpha + e^{ikR} \beta \left(e^{-ika} + e^{ika} \right) \qquad (1.15)$$

Now we can combine equation 1.12 with equation 1.15 to realize,

$$\mathrm{E}\, e^{ikR} = e^{ikR} \alpha + e^{ikR} \beta \left(e^{-ika} + e^{ika} \right)$$

$$\mathrm{E}(k) = \alpha + 2\beta \cos(ka) \qquad (1.16)$$

where the last step uses Euler's formula to transform the exponential function into a simple trigonometric. The simple model derived here can be complicated by considering the physical situation on which the model is to be modeled. For now, it is sufficient to note that Equation 1.16 is a powerful tool to understand the band structure of solids.

With this understanding of how charge transport occurs despite a low transfer integral for each molecule, let us question the assumption that the chain of atoms having a regular periodicity does not reflect the disordered morphology of OSC systems. Polymer systems in particular are largely amorphous with only localized crystalline regions. In disordered systems hopping models help to rationalize how transport can be possible with significant disorder. Two different types of related disorder have been identified: diagonal and off-diagonal. Diagonal disorder is considered to be variations in the energy of the HOMO or LUMO, the onsite energy assigned to be α in the tight-binding model. Off-diagonal disorder is defined as fluctuations in the strength of inter-molecular coupling, the transfer integral identified as β in the tight-binding model.
Building off of the tight-binding model, we will consider α and β to be random Gaussian distributions instead of fixed constants and assign them to the parameters σ, for the onsite disorder, and Σ, for the off-diagonal disorder. First, let us assume that hopping is the primary

mode for transport between molecules. If a charge is transferred from one molecule to another, the molecule with the lower on-site energy will usually end up with the charge. It is possible though for a charge in a lower state to be excited from the lower state to the higher state given thermal fluctuations. The approximate hopping rate, κ, for this to happen can be approximated by the Miller-Abrahams expression, [24]

$$\kappa = \nu_0 e^{-2\beta R} e^{\frac{-\Delta\alpha}{kT}} \qquad (1.17)$$

where ν_0 is the attempted hopping frequency, β is the electronic overlap, Δα is the on-site energy difference between molecules, and kT is the thermal energy. The first exponential in equation 1.17 is associated with a decrease in electronic coupling with distance the second exponential is a Boltzmann factor for a phonon-assisted upward jump in energy.[9, 25] This formalism was originally developed to describe inorganic semiconductors but is widely used to describe hopping transport in OSC literature. The transport model developed by Bässler and coworkers based on this line of reasoning, often called the Gaussian disorder model (GDM), is one of the most highly cited transport models for it generality and impact on the field[26]. From these assumptions, Bässler used a Monte Carlo simulation to arrive at the following empirical equation to express mobility,[27]

$$\mu = \mu_0 \exp\left[-\left(\frac{2\sigma}{3kT}\right)^2\right] \exp\left\{ C\left[\left(\frac{\sigma}{kT}\right)^2 - \Sigma^2\right]\sqrt{\mathrm{E}} \right\} \qquad (1.18)$$

where C is a constant to be determined empirically. Using Equation 1.18 one has a general understanding of how disorder and electric fields affect mobility. Despite the Bässler models wide acceptance in the OSC research field it does not incorporate all of the subtleties of

electronic-coupling between molecules and some of its base assumptions are actively debated in the community.[26]

The last transport model detailed here is called multiple trap and release (MTR). This theory developed from the understanding that mobility is trap-limited. Trapped charges occupy localized states and therefore to not contribute to mobility. Furthermore, they can act as scattering centers for mobile charges and exacerbate electronic disorder by constricting percolation pathways.[25] MTR model is based on the concept of a band of localized states that exists near the conduction band or HOMO. Free carriers in the HOMO drift according to the strength of the electric field and random Brownian motion[26], but as they travel they occasionally drop into a localized state. If the trap state is near the HOMO, the typical ambient kinetic energy of phonons at room temperature is $k_BT \approx 0.025$ eV, then they can be thermally excited back into the HOMO and act as free charges again. This trap and release described by MTR can occur multiple times to a charge carrier as it percolates through an OSC system.

1.2.3 Trap States and Electronic Disorder

The pathway for charge carriers to be transported from molecule to molecule is both across space and energy[25]. Electronic disorder in OSC systems prevents optimal charge transport from being achieved and is related to threshold voltage instability. Thus, traps states are a topic of great interest to the organic electronics community. Trap states will be discussed mostly in the context of transistors, but they are also important for other devices operations, such as their connection with the open circuit voltage in OPV devices.[28]

The localized band as opposed to the transport band was discussed in the overview of MTR model in the previous section. Density of states (DOS) of the localized band, referred herein as the trap DOS, can be measured empirically by a variety of methods,[29] typically with an OFET device. There is much debate over how to describe the trap DOS states.[26] The two common forms of DOS as a function of energy, g(E), is that of either a Gaussian distribution

$$g(E) = \frac{N_t}{\sigma\sqrt{2\pi}}\exp(-\frac{(E-E_0)^2}{2\sigma^2}) \qquad (1.19)$$

or an exponential distribution

$$g(E) = \frac{N_t}{E_U}\exp(\frac{E}{E_U}) \qquad (1.20)$$

where N_t is the trap density, E_0 is the characteristic energy of the band center, E_U is the Urbach energy, and σ is the width of the distribution. Theoreticians often believe that the true form of the trap DOS is a Gaussian distribution, but from experimentation it is observed that the exponential DOS form well describes the localized states in the energy range that affect transport in an operational OFET. In other words, the exponential tail of the trap DOS is not inconsistent with a Gaussian transport DOS.[1] To discern between these two form involves verifying other characteristics of the OFET, such as mobility at different temperatures. This allows for testing the implications of the various competing theoretical transport models.[26] Other forms to fit the trap DOS are also being considered. Possibly that the trap DOS is some combination of both exponential and Gaussian[30] or maybe the true trap DOS cannot be described with a closed form analytical formula. Assuming random distributions of energies and simulating output trap DOS forms might be the best approach in the latter case.[31] Using a tight binding model and assumed

random number distributions has shown reasonable agreement with observed trap DOS in disordered organic polymer systems.

Trapped charges are the empirically observable localized states existing in the active layer, a sort of direct manifestation of the disordered nature discussed in the previous section. Traps are classified depending on their distance in energy from the transport band. Shallow traps are within a few k_BT, close enough to be thermally excited, and deep traps are anything beyond that, are fixed and cannot be freed by thermal excitations. The main sources of charge trapping are usually associated with one of the following: structural defects, chemical impurities, the gate dielectric interface, or thermal motion of molecules.[32] The physics community generally tends to organize these sources of disorder according to whether they are intrinsic or extrinsic to the OSC film. Effects of the gate dielectric and chemical impurities are extrinsic disorder and effects from structural defects and thermal motion are intrinsic disorder. Microstructural complexities can arise from many sources and is not easily related directly to the electronic disorder. The normally considered advantage of material flexibility, the allowed bending in polymer chains or molecular shifts between small molecules, is also a source of off-diagonal disorder in the system. It is common in the comparison between single crystal and polycrystalline OSCs for grain boundaries to be associated with the leading cause of charge trapping. Kaake describes the physics of this well by saying, “Charges are trapped by high-energy grain boundaries, not on them.”[33] Grain boundaries can be controlled through growth kinetics, but they do not explain charge traps that are found in single crystal OSCs.

It is probable that most charge trapping in films can be further mitigated by optimizing fabrication procedures and novel molecular structures. I chose to work towards these ends by carrying out the experiments described in Chapters 3, 4, and 5, with some interesting results. The data from my preliminary research showed that substrate passivation reduces charge trapping related to structural defects by improving growth kinetics. My further studies produced information leading to the conclusion that out-of-plane disorder in layer-by-layer films is a source of interlayer charge trapping. My last project revealed the dynamic nature of operational transistors in trapping charges. When added to the existing body of data, these add to our understanding of charge trapping in the hopes of increasing efficiency in charge transport, expanding the viability of commercially available OSC devices.

1.3 References

1. Z. Bao and J. Locklin, *Organic Field-Effect Transistors*. (CRC Press, Inc., 2007).

2. S. Subramanian, S. K. Park, S. R. Parkin, V. Podzorov, T. N. Jackson and J. E. Anthony, Journal of the American Chemical Society **130** (9), 2706-2707 (2008).

3. C. D. Sheraw, T. N. Jackson, D. L. Eaton and J. E. Anthony, Advanced Materials **15** (23), 2009-2011 (2003).

4. M. M. Payne, S. R. Parkin, J. E. Anthony, C.-C. Kuo and T. N. Jackson, Journal of the American Chemical Society **127** (14), 4986-4987 (2005).

5. O. D. Jurchescu, S. Subramanian, R. J. Kline, S. D. Hudson, J. E. Anthony, T. N. Jackson and D. J. Gundlach, Chemistry of Materials **20** (21), 6733-6737 (2008).

6. S. K. Park, D. A. Mourey, S. Subramanian, J. E. Anthony and T. N. Jackson, Applied Physics Letters **93** (4), 043301 (2008).

7. Y. Mei, M. A. Loth, M. Payne, W. Zhang, J. Smith, C. S. Day, S. R. Parkin, M. Heeney, I. McCulloch, T. D. Anthopoulos, J. E. Anthony and O. D. Jurchescu, Advanced Materials **25** (31), 4352-4357 (2013).

8. C. Wang, H. Dong, W. Hu, Y. Liu and D. Zhu, Chemical Reviews **112** (4), 2208-2267 (2012).

9. V. Coropceanu, J. Cornil, D. A. da Silva Filho, Y. Olivier, R. Silbey and J.-L. Brédas, Chemical Reviews **107** (4), 926-952 (2007).

10. N. W. Ashcroft and N. D. Mermin, *Solid State Physics*. (Holt, Rinehart and Winston, 1976).

11. F. So, *Organic Electronics: Materials, Processing, Devices and Applications*. (CRC Press, 2009).

12. E. C. P. Smits, S. G. J. Mathijssen, P. A. van Hal, S. Setayesh, T. C. T. Geuns, K. A. H. A. Mutsaers, E. Cantatore, H. J. Wondergem, O. Werzer, R. Resel, M. Kemerink, S. Kirchmeyer, A. M. Muzafarov, S. A. Ponomarenko, B. de Boer, P. W. M. Blom and D. M. de Leeuw, Nature **455** (7215), 956-959 (2008).

13. A. Mishra and P. Bäuerle, Angewandte Chemie International Edition **51** (9), 2020-2067 (2012).

14. J.-H. Jou, S. Kumar, A. Agrawal, T.-H. Li and S. Sahoo, Journal of Materials Chemistry C **3** (13), 2974-3002 (2015).

15. S. R. Forrest, Nature **428** (6986), 911-918 (2004).

16. J. Zhao, Y. Li, G. Yang, K. Jiang, H. Lin, H. Ade, W. Ma and H. Yan, Nature Energy **1**, 15027 (2016).

17. H. Sirringhaus, Advanced Materials **21** (38-39), 3859-3873 (2009).

18. F. Dinelli, M. Murgia, P. Levy, M. Cavallini, F. Biscarini and D. M. de Leeuw, Physical Review Letters **92** (11), 116802 (2004).

19. S. M. Sze and K. K. Ng, *Physics of Semiconductor Devices*. (John wiley & sons, 2006).

20. E. G. Bittle, J. I. Basham, T. N. Jackson, O. D. Jurchescu and D. J. Gundlach, Nature Communications **7**, 10908 (2016).

21. A. Ortiz-Conde, F. J. García Sánchez, J. J. Liou, A. Cerdeira, M. Estrada and Y. Yue, Microelectronics Reliability **42** (4–5), 583-596 (2002).

22. G. Horowitz, R. Hajlaoui, H. Bouchriha, R. Bourguiga and M. Hajlaoui, Advanced Materials **10** (12), 923-927 (1998).

23. H.-S. Wong, M. H. White, T. J. Krutsick and R. V. Booth, Solid-State Electronics **30** (9), 953-968 (1987).

24. A. Miller and E. Abrahams, Physical Review **120** (3), 745-755 (1960).

25. N. Tessler, Y. Preezant, N. Rappaport and Y. Roichman, Advanced Materials **21** (27), 2741-2761 (2009).

26. S. Baranovskii, Physica Status Solidi (b) **251** (3), 487-525 (2014).

27. H. Bässler, Physica Status Solidi (b) **175** (1), 15-56 (1993).

28. S. Galindo, M. Ahmadpour, L. G. Gerling, A. Marsal, C. Voz, R. Alcubilla and J. Puigdollers, Organic Electronics **15** (10), 2553-2560 (2014).

29. W. L. Kalb and B. Batlogg, Physical Review B **81** (3), 035327 (2010).

30. W. S. C. Roelofs, S. G. J. Mathijssen, R. A. J. Janssen, D. M. de Leeuw and M. Kemerink, Physical Review B **85** (8), 085202 (2012).

31. J. Rivnay, R. Noriega, J. E. Northrup, R. J. Kline, M. F. Toney and A. Salleo, Physical Review B **83** (12), 121306 (2011).

32. W. L. Kalb, S. Haas, C. Krellner, T. Mathis and B. Batlogg, Physical Review B **81** (15), 155315 (2010).

33. L. G. Kaake, P. F. Barbara and X. Y. Zhu, The Journal of Physical Chemistry Letters **1** (3), 628-635 (2010).

Chapter 2

Experimental Methods and Instrumentation

2.1 Scanning Probe Microscopy

2.1.1 Atomic Force Microscopy

Much of the analysis used for Chapter 3-5 involves data acquired using Atomic Force Microscopy (AFM), a powerful tool for surface analysis that is commonly found in many labs. AFM uses a probe to assess a surface and traces out the morphology in a point by point raster pattern to form comprehensive images. For AFM the probe is situated on the underside of a cantilever that performs a flexural motion as the probe comes into contact with the surface. A laser is centered on the top reflective side the cantilever. The path of the beam then continues from the cantilever to a photodiode sensor. As the probe interacts with the surface, a bend in the cantilever translates to motion of the beam on the photodiode and from this the tip-surface interactions can be precisely measured.

There are many modes that AFM scans can be operated with; the one used for this work is described as dynamic amplitude modulation. Dynamic refers to the fact that the cantilever is oscillated at a distance from the surface, a so called non-contact mode. An advantage of this, as opposed to direct contact used for friction force and conductivity measurements, is that it is non-destructive to the surface. With hard surfaces, like metal, the surface will likely not be damaged by repeated scans. However, OSC films and crystals are held together by weak van der Waals

type interactions and so are very sensitive to deformations either from the tip moving/scratching the surface or molecule sticking to the probe, so non-contact is preferred. This dynamic vertical motion, z, is well modeled by the damped driven harmonic oscillator equation with a perturbation added to account for tip-surface interaction[1],

$$m\ddot{z} + \frac{m\omega_0}{Q}\dot{z} + kz = F_0\cos(\omega t) + F_{ts} \qquad (2.1)$$

where m, the mass; ω_0, the angular resonance frequency; Q, the quality factor; and k, the force constant are all quantities intrinsic to the cantilever. F_0, the driving force, and ω, the angular frequency, are supplied to the cantilever by the AFM. If we ignore the tip-surface interaction, F_{ts}, then Equation 2.1 is solvable analytically and is a good model for the cantilever motion in air at a distance from the surface. A more accurate quantitative description of the AFM cantilever would involve knowing the precise cantilever geometry as well as taking into account the wide variety of different tip-surface interaction forces; such as capillary, adhesive, and electrostatic forces.[1] Nevertheless, this simple model is a good approximation for the tip behavior.

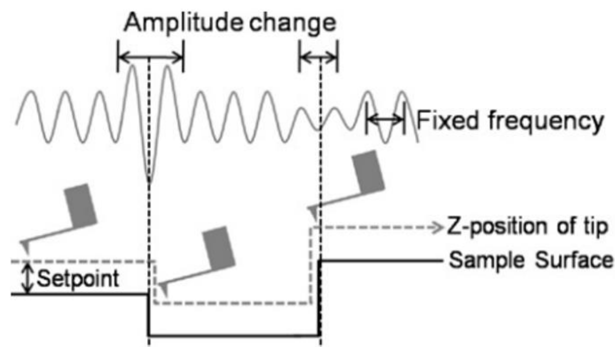

Figure 2.1: Schematic diagram of amplitude modulation atomic force microscopy. This figure is taken from reference [2] of chapter 2.

Amplitude modulation is the way that the surface morphology is calculated from the motion of the probe as it sweeps in a line across the sample surface. Figure 2.1 depicts the major geometric parameters and illustrates the mechanism of amplitude modulation. Set point is a controllable parameter and can be loosely thought of as being inversely proportional to tip-surface force; a small set point equates to a large applied force and a large set point relates to a small force. Z-position of the tip is the measured topography of the surface which is determined by the following process. First the cantilever is oscillated with a fixed frequency, determined by the natural resonance of the cantilever, in near proximity to the surface. As the cantilever sweeps across the surface the amplitude changes with response of the amount of tip-surface force. If the cantilever sweeps over a step down in the surface, then the amplitude will increase. Similarly, if there is a step up then the amplitude will decrease. A feedback loop is set up to regulate the amplitude keeping it constant. So, in either of these two situations the system responds by changing the tip-surface distance to return the amplitude to its original state, moving the tip closer or further from the surface accordingly. This distance between tip and surface is controlled by a piezo-electric attenuator capable of extremely fine motor control. The amount that the tip-sample distance is changed to keep a constant amplitude is the measured height of the sample surface. Another similar process can be achieved by fixing the amplitude and allowing the frequency to vary called frequency modulation. The physics is slightly more complicated for this method but can yield higher surface sensitivity and is thus preferred for ultra-high vacuum AFM systems where atomic resolution is possible.[2]

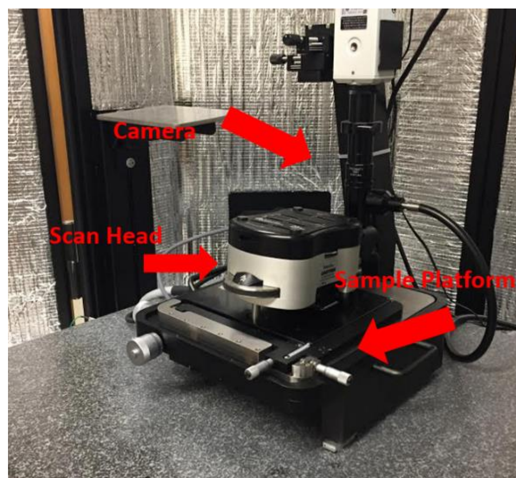

Figure 2.2: Photograph of the MFP-3D AFM used for sample topography and electrical characterization.

Our department uses an MFP-3D from Asylum Research, a very versatile machine in terms of modes of operation and precision of measurement. It is operated in air at room temperature, so a thin contamination layer of hydrocarbons accumulated from the air is assumed to cover all samples and uncontrolled thermal vibrations limit the resolution from resolving single molecules and atoms. The AFM rests on a large granite slab on top of an active shock system and housed in closed-door chamber that all help to counters any acoustic vibrations from interfering with measurements. A camera is used to manually center the laser on the back of the cantilever probe and provides a visual of the sample surface when choosing a location to scan. The cantilever probes used were purchased from Budget Sensors; either Tap300Al-G for standard topography measurements or ElectriMulti75-G.

When operating this AFM there are many parameters that can be adjusted to change the quality of the final image. The main parameters that control image stability are set point, scan size, scan rate, and gain. Each of these parameters must be optimized according to the surface of

the sample. As with all scanning probe microscopy techniques, the probe is what is interacting with the surface and through its behavior in response to given parameters data is obtained about the material surface. This means that the tip integrity and geometry is one of, if not the most, the important factors determining the resolution of the data. If the tip becomes dull then so too will the resolution become dull. If the tip becomes deformed asymmetrically, perhaps from debris sticking to the probe, then a double edge can be observed in the resulting image or geometric shapes of uniform orientation that are nonsensical. During the entire scan the tip should also remain in constant contact with the surface. If any parameters are misaligned, then a variety of artifacts can be observed in the final image. For instance, streaking can occur if the probe temporarily loses contact with the surface.

A discussion of AFM would be incomplete without a discussion of image analysis. Once the data is taken it is rare that only a pretty picture will be enough to qualify as a scientific observation. The virtue of AFM images is that in essence each picture is a matrix of data points as large as the point and line resolution. Root-mean-square (RMS) is a useful and commonly found parameter used to quantify surface roughness,

$$RMS = \sqrt{\frac{1}{n}\sum_{i=1}^{n} {x_i}^2} \qquad (2.2)$$

where x_i is each data point, n is the number of data points. Other canonical formulas of statistical moments should also be considered; such as mean, variance, and skew.

There are common post-processing procedures to alter the image improve the visibility of features and remove simple artifacts from the scanning process. For example, assuming a plane-

fit subtraction to the image can greatly improve the quality of the image. It is rarely the case that the plane that the raster of the AFM is perfectly in line with the plane of the sample. Usually there is a slight gradient in the final topography image from this misalignment that can be adjusted for by a first order xy plane-fit. Another artifact worth mentioning is from hysteresis effects of the piezo attenuator that controls sample-tip distance. Artifacts from this effect can appear in many forms, such as a bowing on one side of the image or a symmetric parabolic shape, and is more difficult to get rid of with post-processing. It is important to be able to identify common artifacts so to not misattribute them to interesting morphology.

2.1.2 Kelvin Probe Force Microscopy

If the cantilever used for AFM has a conductive metal surface, then a potential bias can be applied to obtain local electrical measurements. Kelvin probe force microscopy[3] (KPFM) is the extension of the Kelvin probe adapted for scan probe microscopy. Absolute work function is the difference between the electrochemical potential within and the electrostatic potential outside of a material. Contact potential difference (CPD) is the electrostatic potential difference between points outside and near the surface of two metals in close proximity. If the absolute work function of one of the materials is known, then the other can be determined, but for our purposes relative work function will be enough information. Electrical measurements like this are possible because the short-range forces used to determine topography quickly dissipate according to a van der Waals potential. By retracting the tip slightly (~ 5 nm) from the surface, electrical forces, which are relatively long range, can be observed independent from the tip-surface interactions of AFM described in the previous section.

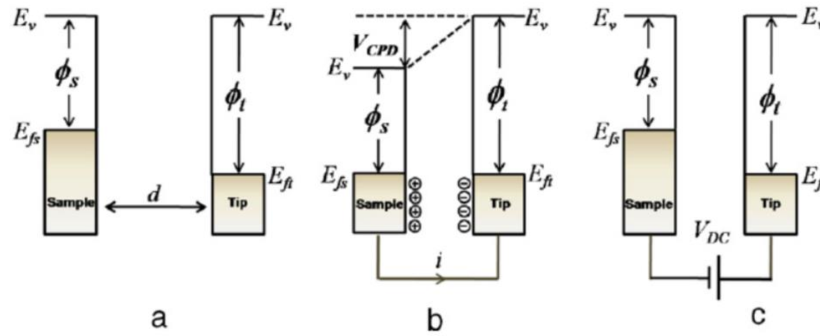

Figure 2.3: Band diagram outline of classic Kelvin Probe. This figure is taken from reference [2] of chapter 2.

Before detailing KPFM, it is best to have a basic understanding of what a Kelvin probe is. This measurement technique is used to measure the CPD between two metal surfaces. Figure 2.3 outlines the basic physics of a Kelvin probe. Two metals of different work function are brought in near proximity of one another, see Figure 2.3a. The two metal are then brought into electrical contact allowing charges to flow between the two metals to a state of equilibrium, see Figure 2.3b. At this point, charges have been displaced from one plate to the other and an electric field is now present between them. The electric field is measured with a potentiometer and a DC bias is now applied to one of the plates to create a null electric field, see Figure 2.3b. Whatever DC bias needed to do this is the CPD between the plates and is identified as the work function difference between the two materials.

For KPFM the probe is not brought into electrical contact with the sample. Instead an AC bias is applied to the tip to generate an oscillating electric field between tip and sample. KPFM acts to minimize this electric field through monitoring the deflection of the cantilever. The electrostatic force generated by this interaction is easily described by the following. From first

principle considerations, the force between a parallel plate capacitor as the distance is varied can be expressed by the formula,

$$F = \frac{1}{2}\frac{dC}{dz}\Delta V^2 \qquad (2.3)$$

where C is the capacitance, ΔV is the potential difference, and z is the distance of separation. Now assume that the potential difference applied to the tip is of the form,

$$V = (V_{DC} - V_{CPD}) + V_{AC} \cdot \sin(\omega t) \qquad (2.4)$$

where the first term is an applied DC bias, V_{DC}, and the contact potential difference, V_{CPD}. The second term of Equation 2.4 characterizes the AC bias applied to the tip. Next substitute Equation 2.4 into Equation 2.3 to get,

$$F = \frac{1}{2}\frac{dC}{dz}[(V_{DC} - V_{CPD}) + V_{AC} \cdot \sin(\omega t)]^2 \qquad (2.5)$$

If one now expands the binomial and organizes by dependence on *ω*, it is apparent that the only term directly proportional to ω can be set equal to zero if $V_{DC} = V_{CPD}$. Thus, the electrostatic force can be minimized by adjusting the value of V_{DC}.

I would like to make note of two important points. One, the charge distribution with KPFM will have an extra negative; this is important for correct interpretations in Chapter 3-5. The origin of this that in the presence of an extra charge, an image charge is formed in the conductive cantilever which is then compensated by the tip bias. So, positive charges will appear negative and negative will appear positive. The second point is that OSC films are not metals, with grounded biases they can be more accurately thought of as insulators.[4] With this realization the measured CPD is *not* just the work function difference between tip and sample, but any stray

fields present will also be convoluted with the CPD. These extra charges could be in the sample, on the tip, or some other extrinsic source. Normally, it is safe to neglect charges on the tip and extrinsic fields as they are usually constant during the entire scan.

2.1.3 Determining Trap DOS Using KPFM

It has been shown that KPFM can be used to directly extract the trap DOS from the surface potential of the channel of an OFET[5]. This experiment has been established in the community as a valid way to measure trap DOS states[6], but only a handful of papers have been written using this process. With standard transistor geometry, as described in Chapter 1, the source and drain electrodes are grounded while the gate bias is slowly shifted. Be fixing the source-drain bias to 0 V the Fermi level of the OSC film is fixed. As the gate bias is increased, the HOMO band is shifted towards the Fermi level. Once the gate bias exceeds the threshold voltage then hole accumulation occurs in the film. The observed surface potential shifts after threshold voltage can be used to directly quantify the trap DOS of the film. The derivation of this relationship, as demonstrated by Tal and Rosenwaks[7], begins with the definition of charge in terms of the density of states, $g(E)$, and the Fermi-Dirac distribution, f_{FD}, written as

$$Q_{film} = q\int_{-\infty}^{\infty} g(E) f_{FD}(E) dE \qquad (2.6)$$

Next, we will define V_{CPD} to be the observed surface potential at a given point relative to the observed surface potential at $V_G = V_{th}$ and then take the derivative of Equation 2.6 with respect to V_{CPD},

$$\frac{dQ_{film}}{dV_{CPD}} = q\int_{-\infty}^{\infty} g(E) \frac{df_{FD}(E)}{dV_{CPD}} dE \qquad (2.7)$$

In this formalism, the Fermi-Dirac distribution is written as,

$$f_{FD}(E) = \frac{1}{1 + \exp(\frac{E - E_{th} - qV_{CPD}}{kT})} \qquad (2.8)$$

where E_{th} is the Fermi level at $V_G = V_{th}$. Taking the derivative of this formula with respect to V_{CPD} is written as,

$$\frac{df_{FD}(E)}{dV_{CPD}} = \frac{q}{kT}\frac{\exp(\frac{E - E_{th} - qV_{CPD}}{kT})}{[1 + \exp\left(\frac{E - E_{th} - qV_{CPD}}{kT}\right)]^2} \qquad (2.9)$$

If the width of Equation 2.9 is much narrower than g(E), then we can express this as a delta function of the form

$$\frac{\exp(\frac{E - E_{th} - qV_{CPD}}{kT})}{[1 + \exp\left(\frac{E - E_{th} - qV_{CPD}}{kT}\right)]^2} = \delta(\frac{E - E_{th} - qV_{CPD}}{kT}) \qquad (2.10)$$

Substituting this into formula 2.7, we now have

$$\frac{dQ_{film}}{dV_{CPD}} = \frac{q^2}{kT}\int_{-\infty}^{\infty} g(E)\delta(\frac{E - E_{th} - qV_{CPD}}{kT})dE \qquad (2.11)$$

Now introduce the following property of the delta function

$$\delta\left(\frac{a}{x}\right) = a\delta(x)$$

to arrive at the formula

$$\frac{dQ_{film}}{dV_{CPD}} = q^2\int_{-\infty}^{\infty} g(E)\delta(E - E_{th} - qV_{CPD})dE \qquad (2.12)$$

Now make use of the fundamental property of the delta function

$$\int_{-\infty}^{\infty} f(x)\delta(x-a)dx = f(a)$$

to get the formula

$$\frac{dQ_{film}}{dV_{CPD}} = q^2 g(E_{th} + qV_{CPD}) \qquad (2.13)$$

Now we can express the DOS in terms of V_{CPD} as

$$g(E_{th} + qV_{CPD}) = \frac{1}{q^2}\frac{dQ_{film}}{dV_{CPD}} \qquad (2.14)$$

Next, we make an assumption about charge neutrality between the charges accumulated in the film being equal to the charges formed at the gate

$$Q_{film} + Q_{gate} = 0$$

and write this into a simple capacitor form

$$Q_{film} = -\frac{C_{ox}}{d_{org}}(V_G - V_{th} - V_{CPD}) \qquad (2.15)$$

where C_{ox} is the oxide capacitance per area and d_{org} is the thickness of the charge accumulation in the film. Finally, substitute Equation 2.15 into Equation 2.14 and rearrange terms to see,

$$g(qV_{CPD}) = \frac{C_{ox}}{d_{org}q^2}[\left(\frac{dV_{CPD}}{d(V_G - V_{th})}\right)^{-1} - 1] \qquad (2.16)$$

This final formula, Equation 2.16, is a powerful tool to determine trap DOS empirically because it makes no assumption on the form of the DOS, as in whether it is exponential of Gaussian. However, the design of the experiment covered in Chapter 5 is to gather many data points to understand deviations of V_{CPD} at each gate bias. In this case the standard deviation for each value of V_{CPD} is large compared to the change in gate bias between each scan. Due to the limited resolution of the derivative of V_{CPD} with respect to V_G, the application of this method of trap DOS extraction to be used in Chapter 5 assumes the exponential form of equation (1.20).

$$\frac{C_{ox}}{d_{org}q^2}\left[\left(\frac{dV_{CPD}}{dV_G}\right)^{-1} - 1\right] = \frac{N_t}{E_U} e^{\frac{-qV_{CPD}}{E_U}} \qquad (2.17)$$

Now, rearrange to solve for the derivative

$$\frac{dV_G}{dV_{CPD}} = \frac{N_t d_{org} q^2}{E_U C_{ox}} e^{\frac{-qV_{CPD}}{E_U}} + 1$$

and integrate from the value of threshold voltage to a given point

$$\int_{th}^{i} dV_G = \int_{th}^{i} \left(\frac{N_t d_{org} q^2}{E_U C_{ox}} e^{\frac{-qV_{CPD}}{E_U}} + 1\right) dV_{CPD}$$

$$\left[V_g(x)\right]_{th}^{i} = \frac{N_t d_{org} q^2}{E_U C_{ox}} \left[\frac{-E_U}{q} e^{\frac{-qV_{CPD}(x)}{E_U}}\right]_{th}^{i} + \left[V_{CPD}(x)\right]_{th}^{i}$$

Lastly, assume V_G(th) and V_{CPD}(th) are equal to zero,

$$V_G = \frac{N_t d_{org} q}{C_{ox}} \left(1 - e^{\frac{-qV_{CPD}}{E_U}}\right) + V_{CPD} \qquad (2.18)$$

Equation (2.18) is a compact analytical formula for to extract the fit parameters of the Urbach energy, E_U, and the trap density, N_t, from the observed surface potential.

2.2 Film Growth

This section is set in the order for which one would make a thin film transistor, as designed for Chapter 5. The film growth methodology is the same for Chapter 3 & 4 with the exception of the Cr/Au deposition outlined in section 2.2.2.

2.2.1 Substrate Prep

Careful cleaning of substrates prior to film growth is very important for reproducible morphology. Any debris on the surface can dramatically change the structure of the OSC film. Periodically during experiments, it is advisable to check the substrate after cleaning before film growth with AFM to have an idea of how many particulates are on the surface. This should be done anyway as a baseline to understand film morphology, but this can also tell you what steps of your cleaning procedures are doing to your substrate.

Substrates for my work were typically purchased from MTI in the form of silicon wafers which were then cut to size using a diamond scribe. The wafers themselves were of crystalline Si (100) with either a native oxide layer or a thick oxide layer of 300 nm. Having a thick oxide is necessary for transistors as the Si acts and the gate electrode and the SiO_2 is the insulating dielectric. Cutting the substrates with a diamond scribe is best done by etching a line on the backside of the wafer and then applying pressure to essentially snap the wafer along this guide-line. This method works quite well if the Si orientation is (100). Si debris are created during this cutting process which can scratch the polished surface of the wafer, so exposure of the polished side of the wafer should minimized during cutting.

Once cut to specified dimensions, the substrates were then washed with a methodical cleaning procedure. The first steps involve sonication, a process by which high frequency acoustic vibrations are used to agitate the substrate submerged in a solution. Approximately 15 minutes of sonication in acetone was followed by another 15 minutes in isopropyl alcohol. In between sonication baths the substrates were individually rinsed with the next solution prior to

submersion. After sonication, the substrates were exposed to UV-ozone for 20 minutes to further decontaminate the surface. Next, the substrates are liberally rinsed with deionized (DI) water. The purity of the water should be as high as possible, DI water sitting in a container degrades over time. Directly after rinsing with water, dry N_2 is used to blow dry the surface. This drying should be most thorough and no droplets should be on the substrates afterward. Nearly all organic matter or residual chemicals from the surface of the substrate should be removed by this process.

The last step to substrate preparation is to treat the surface chemically. This step can have dramatic effects on film growth[8, 9]. Substrate passivation was done using the self-assembling monolayer (SAM) compound hexamethyldisilazane (HMDS). This chemical is most commonly used for photolithography process of Si in industry settings and it is from these sources that the following application recipe has been adapted. Note that HMDS is very sensitive to O_2 and so these steps must be carried out in a N_2 glovebox. First the cleaned substrates are loaded into the glovebox and set on a heating plate for 30 minutes at 120 °C. This step allows for any hydrocarbons on the surface to be evaporated off of the surface exposing the hydroxyl groups. After dehydrating the substrate surface, HMDS is then spin-coated onto the surface. HMDS is dripped onto the substrate, enough to cover it entirely, and the spun at 2000 rpm for 60 seconds. Spinning the sample in this way spreads the HMDS film into a thin uniform layer across the sample and any excess solution is spun off the surface. The finally step is to heat the substrate to 120 °C for another 30 minutes. This last heating step is referred to as activating the SAM.

Heating the HMDS breaks the bonds of the silizane groups which then bond to surface and release ammonia as a byproduct.

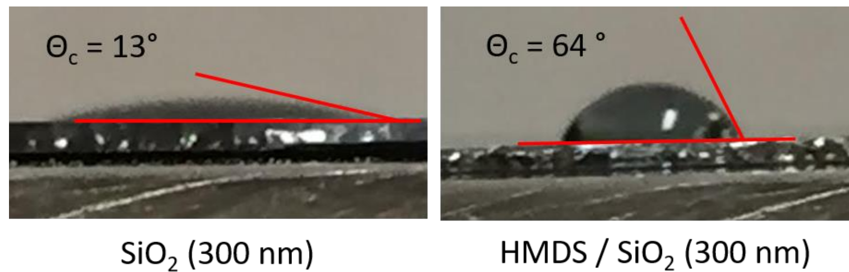

Figure 2.4 – Photograph of water droplet on bare substrate and substrate passivated with HMDS. Contact angle measurement is indicated with red lines.

Measuring contact angle, also known as the sessile drop technique, is a common way to observe the effects of SAM passivation as the surface becomes more hydrophobic with chemical treatment, see figure 2.x. Uniform droplets of DI water were dripped onto the prepared SiO_2 surface using a micropipette and then photographed from a lateral view. From this one can compare the contact angle which is defined as the angle between the surface and the edge of the water droplet. Substrates passivated with HMDS show an average increase in contact angle of 51°, taken from 5 different test on each passivated and un-passivated sample. An increase in contact angle and hydrophobicity is consistent with lowering the surface energy of the substrate. Sample were also heated in vacuum after SAM application with no apparent effect on the contact angle. This was a test to make sure the SAM isn't affected by substrate heating prior to OMBD described in section 2.2.3.

2.2.2 Transistor Electrode Fabrication

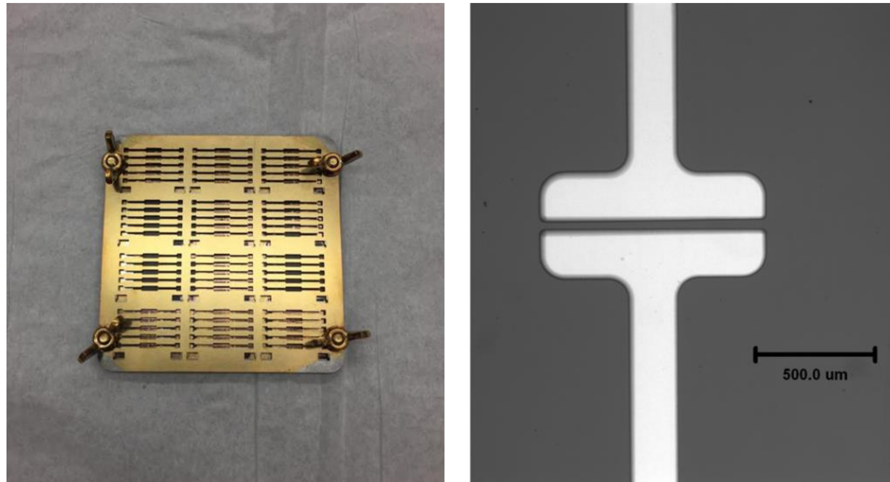

Figure 2.5: (Left) Picture of shadow mask for Au/Cr deposition of source drain electrodes. (Right) Visible light microscope image (x5) of OFET channel.

Directly after the substrates are cleaned they were loaded into a shadow mask purchased from Oscilla for vapor deposition of the source and drain electrodes, see Figure 2.5 (Left). The shadow mask design produced 5 FET channels per substrate, each with variable length ranging from 30-80 µm. When the substrates were loaded into the mask stack, as many as can be fit to conserve materials, there should be minimal gap between them. Any air space will allow for a deformed FET channel as the metal vapor will deviate from the designed transistor dimensions.

Metal depositions were regularly done in our collaborator Dr. Harald Ade's lab for solar cell fabrication, so we used their system to deposit gold (Au) and chromium (Cr). Their evaporation chamber is a MB ProVap 5G purchased from MBRAUN which was situated in a dry

N_2 glovebox, < 0.1 ppm H_2O and < 0.1 ppm O_2. Their Because Au does not readily adhere to the SiO_2 surface, a thin layer of Cr is deposited first. The chromium was evaporated from chrome-plated tungsten rods. Thin high purity Au wire was cut into small pieces, rolled into small balls, and then place in a tungsten boat. High current is run through the tungsten in high vacuum, = 2.5 x 10^{-5} Torr, to heat and evaporate the chromium and gold. Deposition of Cr and Au were preformed sequentially, both monitored individually by quartz-crystal microbalance to monitor flux. Typical nominal thickness of Cr and Au were 5 nm and 100 nm, respectively.

After deposition, the substrates were removed from the shadow mask and inspected individually. The final transistor channel dimensions were measured with a visible light microscope (VLM) that was calibrated for measurements in this range, see Figure 2.5 (Right). This VLM check was also a general quality control assurance prior to deposition of the organic molecules.

2.2.3 Organic Molecular Beam Deposition

Organic molecular beam deposition[10] (OMBD) is the process of thermal sublimation of organic crystals in high vacuum used for film growth. An advantage of OMBD is precise control of film thickness and deposition flux rate. Much of the current studies into making OSC based devices is moving towards solution based for eventual large-scale production in industry. Solution-based depositions certainly has the advantage of being literally printed or deposited in a variety of methods; spin-coating, drop-coating, blade-coating, roll-to-roll printing, etc. But it also introduces the hydrodynamics of the evaporating solution into the growth mode of the layer to be formed. OMBD is also a scalable deposition process that is often overlooked in this regard but is

used currently in some commercial fabrication of organic devices and has been a popular choice in labs for decades[11]. This is the method that will be used in all of the subsequent chapters.

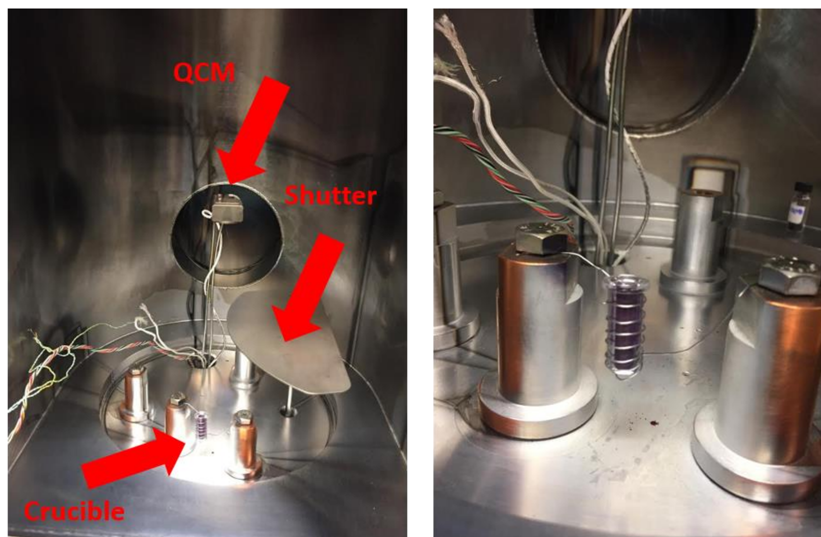

Figure 2.6: Photograph of box chamber used for OMBD process. Photograph of crucible wrapped in tungsten wire.

Our vacuum chamber is named the box chamber and is shown in photographs that are Figure 2.6. The actual chamber was purchased from the Kurt J. Lesker Company and its interior is about 35x35x60 cm^3. A rough pump and turbo pump are used in conjunction to reach an average base pressure of 1-2 x 10^{-6} Torr measured with an ion gauge. To activate the vacuum system, one first turns on the rough pump to clear most of the air from the chamber. After the rough pump settles, you can tell this as the rough pump audibly becomes quieter after about a minute, then the turbo pump is turned on. The turbo pump runs at 1500 Hz when it is up to full spin. Because of the size of the chamber the pump down time to base pressure is approximately 6-8 hours, so we usually just let it run overnight before doing any depositions.

Inside, see figure 2.6 (Left), there is a quartz crystal microbalance (QCM), a manual shutter, heating crucible, and substrate shelf. The basic idea is that crucible heats the molecules to sublimation where they then travel in a straight line upwards toward the substrate above. Having the substrate upside down above the crucible helps prevent contamination from debris falling onto the substrate surface. The shutter blocks the molecules from hitting the substrate so you can control the length of exposure to the molecular beam. Next to the substrate is the QCM which monitors the flux of the beam. As molecules collect on the QCM sensor a slight frequency shift of the quartz natural resonance is measured internally which is then computed into a flux using an assumed density of the material. Any change in temperature will also cause a frequency shift in the QCM, so cooling lines filled with water are used to regulate the temperature. One should make sure the QCM is not blocked by the shutter to make sure you thickness reading is accurate. For our chamber the final thickness calculated by the QCM is approximately half of what is actually on the surface; a factor of geometry that is unique to each chamber.

Organic crystals, usually purchased from Sigma Aldrich or made from the lab of our chemist collaborator John Anthony at the University of Kentucky, is loaded into the quartz crucible, show in Figure 2.6 (Right). Deposition thickness are usually 100 nm or less so the crucible need only be filled about a third of its capacity. A tungsten wire is then wrapped tightly around the crucible over its entire length. The wrap of the wire is important for good growth. If the wire is not tight around the crucible, then you will be wasting power heating the vacuum instead of the quartz. Also, the wire should be wrapped from the bottom all the way to the top for the crucible. If the wire does not cover the bottom, then you will once again be wasting power. If

the wire does not reach the top, then the molecules have a tendency to condensate near the end of the crucible length which eventually leads the forming of a blockage preventing proper sublimation. Out-gassing the molecules is important, particularly with a fresh batch, prior to depositing onto the substrate. This is done by slowing raising the power supply connected to the crucible while also monitoring the chamber pressure for any sudden changes. Sudden changes in pressure is indicative of bubbles of gas being locked into the organic crystal that are suddenly being released. While increasing power to the crucible it is also crucial to be observing the flux output by the QCM. Once you have a stable flux, then you are ready to remove the shudder and deposit molecules onto the substrate.

Heating the substrate during deposition can dramatically affect the morphology of the organic crystals. In the case of 6T, if the substrate is at room temperature during deposition the resulting crystals have a face-on orientation. But, if the substrate is heated to 120 °C during deposition then the 6T molecules prefer a standing-upright orientation with respect to the surface and the growth mode becomes layer-by-layer. In-situ heating can be a powerful tool to manipulate the final morphology of the film.

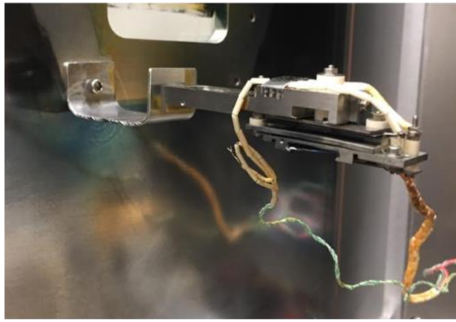

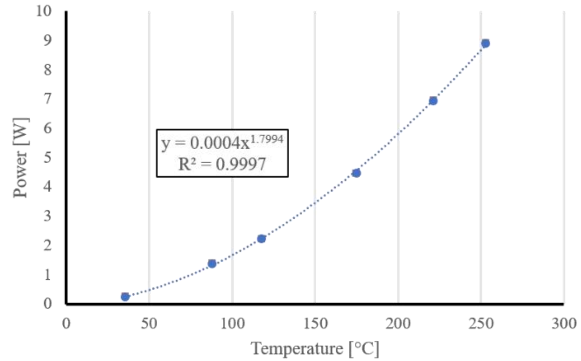

Figure 2.7: (Left) Picture of substrate heater. (Right) Results of heater calibration under vacuum. The data is well fit by a power law.

I installed a substrate heater to the box chamber described previously to allow us this control of 6T morphology. To calibrate the substrate heater an alumel-chromel thermocouple was attached to a substrate. The place of contact when you connect the alloys alumel and chromel has a resistance dependent on temperature in such a way that the temperature at the point where the two wires cross by using a common multimeter. The temperature was calibrated by incrementally increasing the power to the heater and then observed the response of the thermocouple. For each change in power the heater was given about 60 minutes to settle to that new temperature. From this is found that at least 30 minutes should be given to allow the heater to reach a stable 120 °C. The data points in figure 2.x are of the settled temperature after thermal equilibrium. A secondary, permanent, thermocouple was later installed attached directly to the heating arm. This data was compared to the in-situ thermocouple and found to be in reasonable agreement.

2.3 Other Analysis Methods

2.3.1 Grazing-Incidence Wide-Angle X-ray Scattering

Most morphology analysis in this work is preformed using AFM, but a disadvantage of scanning probe analysis is that it can only measure surface features of the sample. In order to characterize the internal structure of organic crystals Grazing-Incidence Wide-Angle X-ray Scattering (GIWAXS) provides meaningful insight. The basic physics of GIWAXS measurements is that a beam of x-rays are directed at the sample with a fixed angle of incidence. Photons in the beam travel through the film and reflect off the substrate creating an interference pattern as it exits again from the film. Data is analyzed from the diffraction peaks, which are in reciprocal space, created from the scattered beam hitting a 2D detector. Using a 2D detector allows for measurement of both in-plane and out-of-plane structures with respect to the substrate. For a trained expert, analysis of the scattering peaks can tell a lot of information regarding the crystal structure of the sample.[12] Defined sharp spots and rings are associated with a well-defined crystallographic orientation with respect to the substrate, as opposed to broad, streaking features which are telling of anisotropy in the material. NCSU does not have a synchrotron to generate these x-rays so samples made in our lab were sent off for analysis at beamlines at either Stanford or UC Berkeley. GIWAXS data is used in both Chapters 3 and 4 to help characterize the crystallographic orientation of OSC films.

2.3.2 Probe Station

To analyze transistor characteristics a ST-500 series probe station purchased from Janis. There are a total of four-probes and a metal chuck are usable and the chamber itself is floated

using compressed air to minimize ambient vibrations during measurements. Under normal conditions one would use two of the probes to make contact with the source and drain electrodes and then use the metal chuck to supply a gate bias to the sample. As procedure, to make the gate contact one would scratch the backside of the Si substrate to remove an area of the oxide. Then the scratches are covered with a thin layer of silver paint to make a permanent contact. The system is also capable of low-temperature cooling using recirculated liquid He and has a vacuum pump capable of reaching a base pressure around 10^{-5} Torr. However, all measurements reported in this work were done in air at room temperature to replicate the similar conditions used during KPFM scanning. A Keithley 4200-SCS semiconductor characterization system was used as a voltage supply as well as parameter analyzer. As a voltage supply the Keithley 4200-SCS is capable of using large DC voltages and pulses and is highly sensitive to small currents. Transfer characteristics were taken in the linear regime with low drain-source bias and the gate was normally varied from 0 to -70 V. The system is also pre-loaded with many other settings for a wide variety of experiments to make normally complex analysis easy to use.

2.4 References

1. R. Garcıa and R. Perez, Surface Science Reports **47** (6), 197-301 (2002).

2. W. Melitz, J. Shen, A. C. Kummel and S. Lee, Surface Science Reports **66** (1), 1-27 (2011).

3. M. Nonnenmacher, M. P. O'Boyle and H. K. Wickramasinghe, Applied Physics Letters **58** (25), 2921-2923 (1991).

4. J. L. Neff and P. Rahe, Physical Review B **91** (8), 085424 (2015).

5. O. Tal, Y. Rosenwaks, Y. Preezant, N. Tessler, C. K. Chan and A. Kahn, Physical Review Letters **95** (25), 256405 (2005).

6. W. L. Kalb and B. Batlogg, Physical Review B **81** (3), 035327 (2010).

7. O. Tal and Y. Rosenwaks, The Journal of Physical Chemistry B **110** (50), 25521-25524 (2006).

8. M.-H. Yoon, C. Kim, A. Facchetti and T. J. Marks, Journal of the American Chemical Society **128** (39), 12851-12869 (2006).

9. S. R. Walter, J. Youn, J. D. Emery, S. Kewalramani, J. W. Hennek, M. J. Bedzyk, A. Facchetti, T. J. Marks and F. M. Geiger, Journal of the American Chemical Society **134** (28), 11726-11733 (2012).

10. F. Schreiber, Physica Status Solidi (a) **201** (6), 1037-1054 (2004).

11. S. R. Forrest, Nature **428** (6986), 911-918 (2004).

12. P. Müller-Buschbaum, Advanced Materials **26** (46), 7692-7709 (2014).

Chapter 3

Intrinsic Charge Trapping Observed as Surface Potential Variations in diF-TES-ADT Films

Benjamin C. Hoffman,[†‡] Terry McAfee,[†‡] Brad R. Conrad,[‡⁑] Marsha A. Loth,[※] John E. Anthony,[※] Harald W. Ade,[†‡] and Daniel B. Dougherty[†‡]

† Department of Physics, North Carolina State University, Raleigh, North Carolina 27695, United States
‡ Organic and Carbon Electronics Lab (ORaCEL), North Carolina State University, Raleigh, North Carolina 27695, United States
⁑ Department of Physics and Astronomy, Appalachian State University, Boone, North Carolina 28608, United States
※ Department of Chemistry, University of Kentucky, Lexington, Kentucky 40506, United States

This chapter is based on the following publication: B.C. Hoffman, T. McAfee, B.R. Conrad, M.A. Loth, J.E. Anthony, H.W. Ade, and D.B. Dougherty. ACS Applied Materials and Interfaces **8**, 21490-21496 (2016).

Abstract

Spatial variations in surface potential are measured with Kelvin probe force microscopy for thin films of 2,8-diflouro-5,11-bis(triethylsilylethynyl)anthradithiophenes (diF-TES-ADT) grown on SiO_2 and silane-treated SiO_2 substrates by organic molecular beam deposition. The variations are observed both between and within grains of the polycrystalline organic film and are quantitatively different than electrostatic variations on the substrate surfaces. The skewness

of surface potential distributions is larger on SiO_2 than on HMDS-treated substrates. This observation is attributed to the impact of substrate functionalization on minimizing intrinsic crystallographic defects in the organic film that can trap charge.

3.1 Introduction

Many organic electronic materials[1-3] take advantage of π-conjugated orbitals to encourage intermolecular charge transport and control excitations within devices. The widespread interest in conjugated organic semiconducting molecules, which has been fueled by their ease of processability and manufacturing potential, makes them viable for commercial devices such as light-emitting diodes[4, 5] and photovoltaic systems.[6-8]

Charge mobility is often quoted as the holistic indicator of organic electronic material performance despite the fact that the complexities of charge transport are often device and test specific.[9] The transfer integrals coupling different molecules in organic solids are typically small in comparison to inorganic semiconductors, such as silicon, which often results in relatively smaller mobilities.[10] This intrinsic limitation places a premium on optimizing charge transport in devices. To further compound the issue, the prevalence of structural and associated electronic disorder in what is called soft organic materials means that improving transport mechanisms involves both molecular (synthetic) and solid-state (processing) design.

Electronic disorder in organic semiconductor devices gives rise to a broadened distribution of polarization energies that can create localized charge traps.[10] These traps can be intrinsic in origin, as in the case of structural defects that can generate a local lattice constant perturbation. Charge traps can also be generated by extrinsic forces within a specific molecular

solid, such as with chemical impurities, material decomposition, or device related interfaces including electrodes or gate materials. Characterization of charge traps has been a long-standing pursuit in the field,[11] and numerous observations with different tools have led to important phenomenological understanding. Measurements of charge trapping are usually performed by transport measurements in a transistor geometry or by sensitive optical spectroscopy. In this paper, we focus on the significance of spatial variations in surface potential as an indicator of localized trapped charges in ungated organic molecular films created by an organic molecular beam growth process.

The intrinsic origins of charge traps can often be correlated to the grain boundaries of polycrystalline films that form a high potential barrier inhibiting charge motion.[12] While some studies[13, 14] have indicated that charges are trapped directly on the boundaries, an increase in trapped charge density within the domain and away from the boundary also fits within the paradigm of observation.[12] The effect of grain boundaries on charge mobility is still controversial. While some groups conclude that grain boundaries are expected to dictate charge transport,[15] other experiments have shown relatively high mobilities through films with relatively small domains.[16] Furthermore, shallow traps have been shown to arise from molecular sliding of single monolayers of pentacene[17] where vertical displacements relative to the substrate create local defects even though an overall uniform 2D crystal packing is maintained. It is evident that structural defects are also a source of intrinsic charge trapping.

An extrinsic cause of charge trapping arises from the interface between the molecule and the substrate. At the dielectric interface, randomly oriented dipoles can affect local site energies

and increase the surface energy.[18] Reduction of trap states has been demonstrated through the use of self-assembled monolayers (SAMs) that alter the surface state of the substrate prior to molecule deposition.[19] Controlling charge trapping by changing the surface chemistry of a substrate is well studied,[20] and these effects can be observed directly in measured electronic density of states. By passivating the silicon substrate surface with the SAM hexamethyldisilazane (HMDS) prior to deposition of pentacene, trap states are shown to be alleviated[21] by reducing the density of states in the gap. A quantitative model[22] involving static dipole disorder has been proposed to address this relationship between the dielectric and active layer that promotes mobility with the use of SAM. The physics of charge transfer at this interface is of paramount importance to thin-film transistor (TFT) design since most charge transport occurs in the first few monolayers next to the dielectric.[23]

Such devices are an example of when charge traps can originate *extrinsically* from the electrostatic impact of charged impurities in the dielectric. Extrinsic effects can be even more pronounced in the case of 2D transistors[24] and self-assembled monolayer transistors[25] where the channel is only a single molecular layer in contact with the gate. However, as noted by Kalb et al., the nature of the gate dielectric can also influence the growth morphology of the TFT channel and this can lead to *intrinsic* structural charge traps in the organic film in addition to the direct dielectric-induced traps.[18] In this paper, we focus attention on spatially inhomogeneous surface potentials in an important emerging class of organic semiconductors that arise from such substrate-controlled growth defects intrinsic to the organic film. Using Kelvin probe microscopy

(KPFM), our experiments visualize surface potential variations due to traps which differ dramatically from the variations present in the gate dielectric.

Scanning probe microscopy has already proven to be a useful tool to study the Coulombic influence of traps in organic films in a transistor geometry.[14, 26] For example, Marohn and coworkers saturated a thin-film transistor composed of pentacene with a large gate voltage potential and then observed the long lifetimes of lingering charges by use of frequency-modulation electric force microscopy (FM-EFM). The length scale of study indicates that the charge traps are not homogeneously distributed throughout the active layer, and instead, the different domains hold charges of different magnitudes. Further investigation using time-resolved KPFM into the lifetimes of transient charge traps indicates that their cause is due to extrinsic atmospheric impurities in the film.[27] These various observe transient charge trapping. By contrast, in this paper, we focus on surface potential variations in an ungated organic thin film as a probe of charge traps in a relatively static system.

The class of semiconductor in our experiments is the functionalized anthradithiophenes that have shown a very promising combination of transport performance and versatile processability. Specifically, the molecule used for this study is the hole transporting organic semiconductor 2,8-diflouro-5,11-bis(triethylsilylethynyl)anthradithiophenes (diF-TES-ADT).[28] This optimized variant of TIPS-pentacene with an anthradithiophenes backbone is fluorinated to enhance crystallization. Published results indicate a mobility as high as 1.5 $cm^2/V \cdot s$ when spin-coated for thin-film transistor devices[29] and single crystal devices exhibit an even greater mobility as high as 6 $cm^2/V \cdot s$.[30] Other studies have focused on optimizing blends of diF-TES-

ADT to better understand the effects of charge traps on transport.[31] Transistors have also been used to measure the surface potential gradient across a channel under drain-source bias,[32] which identified the grain boundaries as a limiting factor for charge transport across long multigrain channels while short channels were dominated by the interface of the film with the electrodes.

The contents of this paper will describe for the case of diF-TES-ADT further study of the effects of grain boundaries and the interfacial effect of organic thin films with dielectrics on electrostatic properties related to charge trapping. Scanning probe microscopy reveals that surface potential inhomogeneity is distinct from the topography of the complex organic microcrystal morphology. Variations in surface potential can be observed with high lateral resolution to characterize intrinsic charge distribution within an individual domain and among many. The primary results of this paper is that the statistical distribution of surface potential within the film is different from that of the potential distribution of the substrate but can be quantitatively change through substrate functionalization. This indicates that, for the ADT molecules considered here, the role of SAM functionalization is to determine the intrinsic structural defect density in the active organic layer.

3.2 Experimental Methods

Atomic force microscopy (AFM) and KPFM measurements were carried out using a commercial instrument (Asylum MFP-3D). Film topography was observed in standard noncontact mode using commercial cantilevers (Budget Sensors Tap300E-G). We used KPFM[33] to observe the contact potential difference (CPD) between the electrically conductive AFM tip and the thin film sample. The KPFM measurement begins with a topographic line scan, and then

the tip is slightly retracted from the sample and the topography is traced again at the new distance to sense predominantly long-range electrostatic forces given in Equation 3.1. The noncontact KPFM measurement geometry is most simply modeled by the electrostatic force equation[34]

$$F = \frac{1}{2}\frac{dC}{dz}[(V_{DC} - V_{CPD}) + V_{AC} \cdot \sin(\omega t)]^2 \qquad (3.1)$$

where electrostatic force F_{es} is determined by applying a bias V_{Tip} and an oscillating voltage V_{AC} to the scan probe. A lock-in amplifier is able to minimize the electrostatic force by adjusting V_{Tip} to balance the contact potential difference V_{CPD} of the samples surface so that their potential difference ($V_{Tip} – V_{CPD}$) is null over each point of a raster scan. Subsequently, the CPD of the surface is mapped with the corresponding topography. Thus, interrelation between surface topography and surface potential maps can be identified.

It is important to note that, when measuring a conductive surface, the CPD is ideally the work function difference between tip and sample. However, if the sample is a semiconductor (as in the present study), any other fields present,[35] such as point charges located on sample within either the organic domain or the bulk of the substrate, must be taken into consideration by the inclusion of additional terms within Equation 3.1. Any charges within the film will induce an image potential within the scan probe that will offset the observed CPD. Because this charge induced signal is observed via an image potential, the resulting perturbation from the relative work function will be of opposite magnitude to the true sign of the charges present in the sample.[36, 37] Previous work has used Monte Carlo simulations to directly connect inhomogeneous charge trap distributions with surface potential variations and their statistical distributions.[38]

During image scans, the silicon substrate was held at the grounded potential of 0 V to stabilize any transient charge flow. Such conditions have been used in other studies[39] to analyze the relative surface potentials between SAM and organic films. All scans in this study were recorded with 512 by 512 points and lines resolution of sizes either $(2\ \mu m)^2$ or $(10\ \mu m)^2$ at slow speeds (≤ 0.2 Hz) to ensure that time-dependent charging effects were negligible. The comparison of trace and retrace scans allows for the confirmation of scanning measurement stability and reproducibility. Care to preserve the tip integrity was used by maximizing the set point used during operation. The cantilever raster during CPD measurements was engages 5 nm from the sample surface measured during topography. To increase resolution of the CPD measurements, low amplitude of the cantilever oscillation was used during scans.

Silicon substrates were cleaned by sonication in acetone and isopropyl alcohol, followed by UV ozone treatment, sonication in deionized water, and finally blow-drying with dry N_2. For samples treated with HMDS, prior to deposition, the substrate was first heated to 120 °C in a dry N_2 environment for 30 minutes to activate the SAM. Cleanliness of substrates was confirmed by AFM to ensure minimal residual particulates and debris.

DiF-TES-ADT films were grown by standard organic molecular beam deposition[40] (OMBD) in a high-vacuum chamber at pressures of ~ 10^{-7} Torr. A molecular flux of ~ 0.1 Å/s for deposition was continually monitored by a quartz crystal microbalance (QCM), and the diF-TES-ADT source material was evaporated from a quartz crucible. Prior to deposition, the source material was purified just below the sublimation temperature to promote the removal of impurities.

For crystallographic experiments, grazing-incidence wide-angle x-ray scattering (GIWAXS) patterns were collected at beamline 7.3.3 at the Advanced Light Source.[41] Simulated scattering calculations[42] were used to compare measured peak patterns with known bulk crystal orientations. All samples fabricated and analyzed for this study were also measured with GIWAXS to ensure reproducibility.

3.3 Results and Discussion

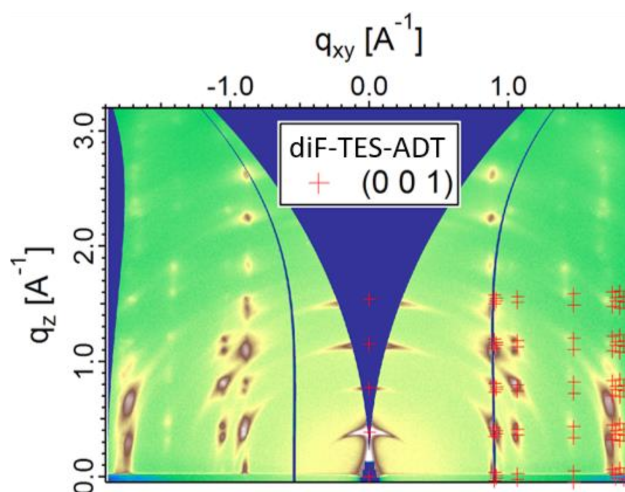

Figure 3.1: A characteristic GIWAXS result of a thick film (~ 100 nm) with HMDS-treated substrate. Simulated scatter points of known crystal orientation, displayed as red crosses, suggest a uniform (001) orientation.

The thickness of diF-TES-ADT thin films was varied from an incomplete substrate coverage, with a nominal deposition of 10 nm, to a relatively thick film with complete substrate coverage, with a nominal deposition of 100 nm. For both cases, CPD variations are discussed in relation to the observed topography as measured by KPFM. It is important to note that crystal orientation influences the ionization energy of molecular structures[43] and, therefore, must be

taken into account when considering the CPD morphology of our samples. For all samples, GIWAXS measurements showed that the diF-TES-ADT films grown by OMBD were of the uniform orientation (001) with respect to the substrate, as seen in the GIWAXS of a thick film (~ 100 nm) with an HMDS-treated substrate of Figure 3.1. This observation is an interesting comparison to the reported diF-TES-ADT crystals formed by spun-cast solution where both (001) and (111) crystallites are observed.[44] Evidently, the OMBD growth kinetics promotes only a single crystallite orientation compared to the complex kinetics that can occur during solution casting. This uniform orientation resulting from OMBD film growth was also seen for thick films of diF-TES-ADT on Au (111) substrates.[45] Given the observation of uniform orientation, the ionization energy of the diF-TES-ADT microcrystals, which is the largest factor determining the work function, will be spatially uniform across different domains.

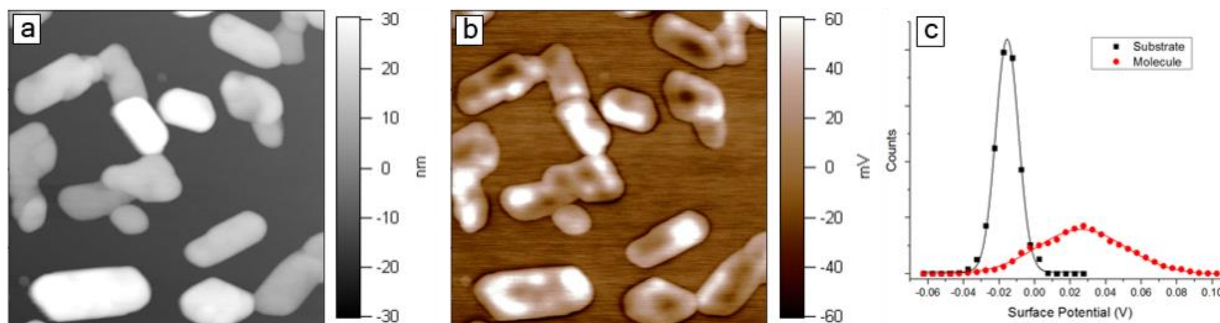

Figure 3.2: $(2\ \mu m)^2$ (a) topography and (b) surface potential images of diF-TES-ADT crystallites on a native SiO_2 substrate grown via organic molecular beam deposition. Part (c) is a histogram of surface potential image (b) with separate data sets of intensity for the substrate and the molecule. The points indicate the true data, while the solid line is a single Gaussian peak fit to the data.

As seen in the $(2\ \mu m)^2$ AFM scan of Figure 3.2a, since the diF-TES-ADT thin films were grown to a nominal thickness of 10 nm on native SiO_2, isolated molecular islands could be

studied with easy reference to the substrate. The 3D islands visible in Figure 3.2a are typically 30-40 nm in height, which are taller than the nominal reading of the QCM during growth due to the apparent 3D island growth mode on SiO_2.

Upon inspection of the $(2\ \mu m)^2$ KPFM scan of Figure 3.2b, it is immediately apparent that the local variations in surface potential can be associated with both intragrain and intergrain surface potential differences with the diF-TES-ADT microcrystals. While the surface potential of the substrate should generally be flat, deviations that are observed are likely attributable to measurement noise or charge traps in the native oxide.[46] A steep drop in surface potential is evident as a dark halo on the outermost edge of the some domains in the surface potential image. This is an artifact attributable[37] to the tip-surface geometry as the tip interacts with the crystal domain from the side and detects an increased area of influence. In contrast, intragrain surface potential variations ~ 100 mV, a magnitude notable larger than that previously observed in some thin films of pentacene,[46] are not attributable to such topographic effects. These variations are interpreted as an intrinsic charge trap distribution across the microcrystal domains. A pattern of lowered surface potential accumulated on the domain is never directly observed on the grain boundary edge. It is also apparent in Figure 3.2b that the magnitude of intragrain variations is significantly greater than any change in CPD along the intersection of multiple grains.

Figure 3.2c is a histogram depicting the potential distribution of Figure 3.2b for comparison of the magnitudes of the potential variations. The histogram was created by setting a threshold mask in topography to isolate the substrate from the molecular domains, which was then copied over onto the CPD image. These two data sets were then both filtered into 5 mV bins

and then fit with a single peak Gaussian. Considering these separate features, the substrate has a comparatively smooth surface potential with a standard deviation of 8.2 mV, and the organic microcrystals have an increased standard deviation of 26.3 mV. The surface potential distribution of the native oxide silicon substrate makes for a concise comparison to the broad CPD variations of the diF-TES-ADT domains. There is a potential difference of ≈ 40 mV between the average values of the substrate and molecular crystallites, a value comparable to that reported for other molecular films.

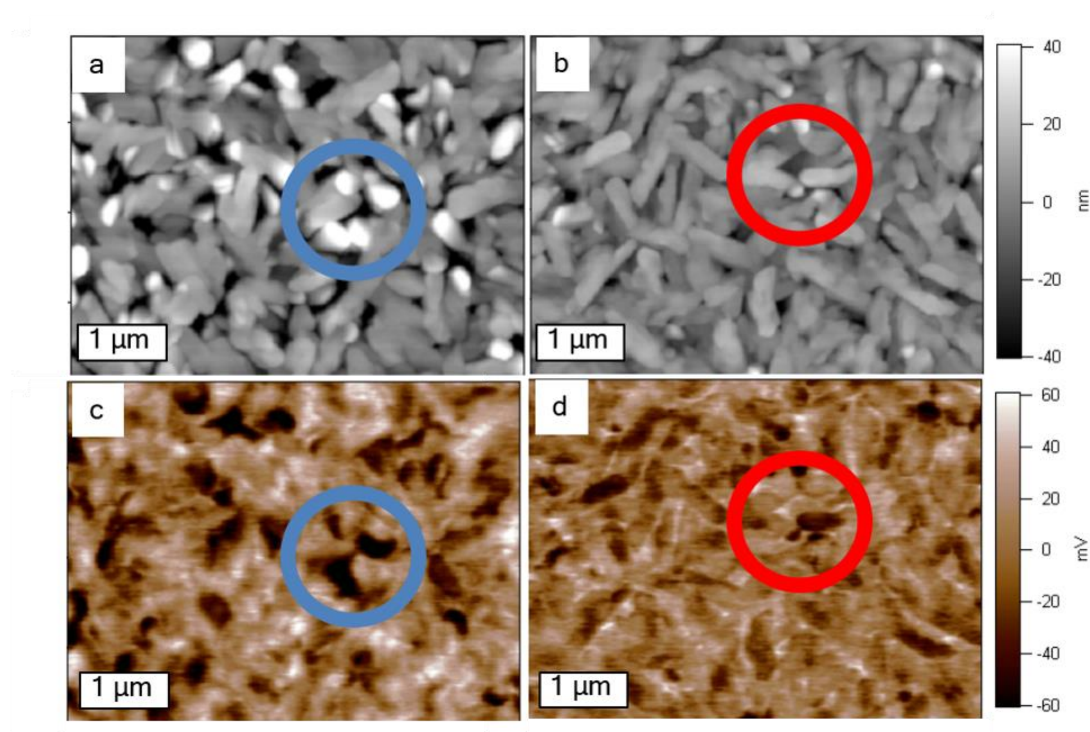

Figure 3.3: Images (a) and (b) are topography scans, whereas (c) and (d) are surface potential images of complete diF-TES-ADT coverage of silicon substrate. Images (a) and (c) correspond to films grown on an untreated substrate, whereas (b) and (d) are films grown on a substrate treated with HMDS. All images display 1 μm scale bars.

Thicker films, of a nominal 100 nm thickness, with complete substrate coverage were grown to assess intrinsic surface potential variation in device-relevant structures, as shown in the topography of Figure 3.3a and the KPFM of Figure 3.3c. The scans shown in Figure 3.3a,c are from untreated SiO_2 substrates, whereas scans shown in Figure 3.3b,d are from HMDS-treated substrates. The surface potential variations that are present in both the treated substrate thin film of Figure 3.3c and the untreated substrate thin film of Figure 3.3d are qualitatively similar to those seen in the observations of the isolated domains in Figure 3.2b. In addition, the effects of treating the SiO_2 substrate with HMDS can be seen in Figure 3.3b,d. The topography of the films on the treated substrates consists of crystallites that are more elongated than on the untreated substrates. Treated films display a smaller root-mean-square (RMS) roughness value of 9.3 ± 0.3 nm, whereas untreated films display an RMS roughness of 17.4 ± 0.3 nm. Thus, Figure 3.3 topography shows that the HMDS treatment of the substrate promotes better long-range crystallinity in the diF-TES-ADT films.

KPFM images reveal that topography does not single determine the distribution of the inhomogeneous aggregation of static charges, a finding also observed with pentacene films.[47] For example, in some areas, the vertical height in topography is correlated to lowered surface potential. This can be seen within the associated blue circles in Figure 3.3, where regions of lighter contrast in topography correspond to regions of locally dark contrast in surface potential. By contrast, areas that are similar in topography but have opposite contrast in surface potential are also observed, illustrated on the left- and right-hand sides in the red circles in Figure 3.3b,d. The HMDS treatment significantly lowers the magnitude of these surface potential variations,

which is apparent from the RMS surface potential variations of 16.4 ± 0.6 mV for films on the treated substrate compared to 25.9 ± 0.3 mV for the untreated sample.

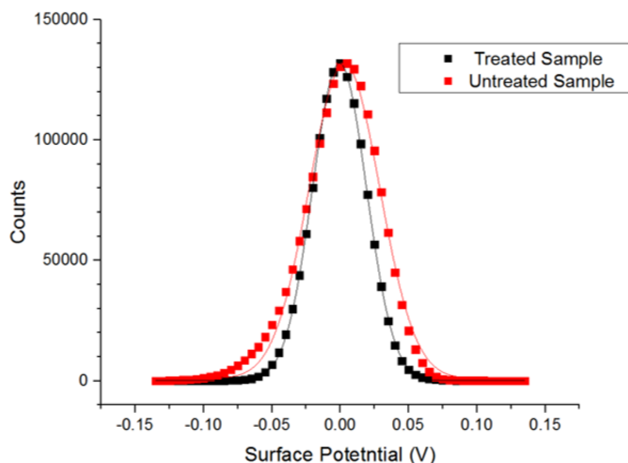

Figure 3.4: Histogram of surface potential values for a set of compiled KPFM scans. The HMDS-treated substrate (untreated) data displayed by black (red). The boxes indicate the true data, while the solid line is a single peak Gaussian fit to these points.

For a quantitative comparison of the potential variations in the films grown on different substrate, the statistical distribution of surface potential was extracted from KPFM data. The image data of five different (10 μm)^2 KPFM images for each substrate were compiled and compared through a normalized histogram, as seen in Figure 3.4 (individual scans that compose Figure 3.4 can be found in the Supporting Information, Figure 3.5). Each scan was centered about its mean surface together for analysis. A single peak Gaussian has been fit to each group of data to illustrate the deviation from a normal curve. The surface potential data of the untreated sample (red squares) are significantly skewed left, whereas the HMDS-treated sample displays a significantly smaller skew and is better approximated by a single Gaussian peak. Skew can be quantified directly from the pixel values of each CPD images using the standard formula

$$skew = \frac{1}{N}\sum_{i=1}^{N}\left(\frac{x_i - \mu}{\sigma}\right)^3 \qquad (3.2)$$

where x_i is the pixel value at each point on the KPFM image, N is the total number of points, μ is the mean, and σ is the standard deviation. This numerical measure has been used for organic electronic materials recently to quantify inhomogeneous charge distributions,[38] and we take the same approach here. Averaged distribution for the HMDS-treated sample is -0.24 ± 0.03, whereas the untreated sample has a CPD distribution skewness of -0.57 ± 0.04.

Negative skewness of the surface potential distribution is indicative of an increased population of hole-type charge regions from the organic material dispersed across the film, which is perceived by the scanned probe as a negative deviation from the relative work function.[36] The observed trend in skewness of surface potential is *not* repeated under similar analysis of sample topography, where the values are -0.62 ± 0.16 and -0.07 ± 0.11 for the treated and untreated sample, respectively. A possible interpretation of the difference in skew values of topography is that the treated sample consists of generally uniform crystallite heights with the spaces between domains contributing to a negative skew. The heights for the untreated sample are not uniform, and the spaces between crystallites have less weight within the distribution. Regardless, this comparison of skew values indicates that the skew reduction in measured CPD is a unique feature of the surface potential of the film and not determined by topographic features (which clearly also depend on substrate treatment). Moreover, the bare substrate CPD distributions without diF-TES-ADT films are much more narrow and do not show the observed trend in skewness (see, e.g., Figure 3.2c). Thus, the differences in the shape of the surface

potential distributions do not simply arise from the electrostatic landscape of the underlying substrate. To determine the quantitative relationship between the skew and charge carrier population, a simulation involving all internal/external fields as well as the tip-sample geometries could be used.[37] A simulation of this type is not the focus of this paper, but relevant quantities obtained from our observations could be used as an empirical reference for future computational studies.

The surface potential distribution on isolated domains clearly shows that intrinsic charge traps do not have a tendency to accumulate sharply on the grain boundary,[12, 37] but can occur anywhere within such structures. The specifics of boundary formation and the physical mechanism by which charges are trapped ultimately determine the spatial distribution of the surface potential variations. Even so, grain boundaries still play an important role in optimizing TFTs, where there is evidence[32] of a potential barrier at the interface of large diF-TES-ADT grains that exists under source-drain bias. Furthermore, dynamic charge trapping stimulated by gate bias stressing also points to grain boundaries as a place of charge localization.[14] These complementary observations illustrate a more comprehensive interpretation for the distribution of charge traps as they vary between states of excess charge introduced during gate stressing and the relatively quiescent ungated conditions reported here.

Though charge trapping can be caused by extrinsic factors, such as chemical impurities, the evidence presented highlights the impact of intrinsic influences, such as the gate dielectric interface and randomly situated imperfections within film crystallinity. The beneficial use of SAM does not screen the electrostatic landscape of the substrate in our measurements. Instead, it

evidently creates an enhanced interface for the lower trap density film growth by increasing the surface energy, leading to improved interaction among neighboring molecules.[48] Intrinsic defects within the film crystal lattice that originate from growth processes nucleated at this interface can be as important as extrinsic electrostatic factors.[27] Indeed, our observations here show that their effect is not negligible and can lead to surface potential variations comparable in size to the disordered broadened density of states in typical organic materials.[21, 48]

3.4 Summary and Conclusions

In summary, we have observed spatial variations in surface potential in (001)-oriented diF-TES-ADT films grown by OMBD that are attributed to randomly distributed charge traps that locally distort the surface potential from the uniformity expected for (001) crystal faces. Surface potential variations are observed using KPFM both within individual organic crystalline domains and between different grains. The length scale associated with these variations is on the order of 100s of nanometers. Most importantly, the statistical distribution in energy of these potential variations is observed to be very different than the supporting substrate but nevertheless to depend upon whether the substrate has been treated with an HMDS SAM. Thus, we assign the microscopic origin of these charge traps as intrinsic structural defects within the organic crystallites that form kinetically during growth. The key conclusion is that the role of the SAM in this particular film is evidently to optimize OMBD growth kinetics for minimal structure-induced charge trap formation and not to directly screen charges within the gate dielectric as has been found for some other organic films.[21] In fact, this comparison highlights the unusual

complexity of organic electronic materials and device optimization: the ultimate effect of processing strategies is not always predictable.

Disorder and associated charge traps are often the crucial determining factor in electronic and optoelectronic device performance.[3, 18, 49] In any individual material system, there is a complex interplay between processing strategies and microscopic origins of charge traps. Perhaps the most instructive comparison is between the OMBD films we describe and solution cast films of diF-TES-ADT such as described by Li et al.[44] In solution casting, there is seen significant film orientation disorder for which different casting or solvent annealing strategies may be necessary to mitigate charge trap formation. By contrast, OMBD films have a single crystallographic orientation with respect to the substrate, but still show charge traps that are evidently closely connected to growth kinetics. As the organic electronics community creates and characterizes increasingly complex new materials, such as the functionalized anthradithiophenes[28] described here, it is imperative to identify the microscopic nature of key defects. Though charge trapping is complex and can arise from various physical processes,[18] the strategies described here can be used to quantify intrinsic charge trapping to further control and mitigation.

Acknowledgments

Film growth and scanned probe microscopy was funded by NSF CAREER award DMR-1056861, and GIWAXS measurements at the Advanced Light Source were funded by the U.S. Department of Energy, OS BES, MSE (DE-FG02-98ER45737). The Advanced Light Source is supported by the Director, Office of Science, Office of Basic Energy Sciences, of the U.S.

Department of energy under Contract No. DE-AC02-05CH11231. Special thanks to beamline 7.3.3 Staff Alexander Hexemer and Eric Schaible for help with data acquisition and maintenance. Material synthesis was supported by the National Science Foundation (CMMI-1255494).

3.5 Supporting Information

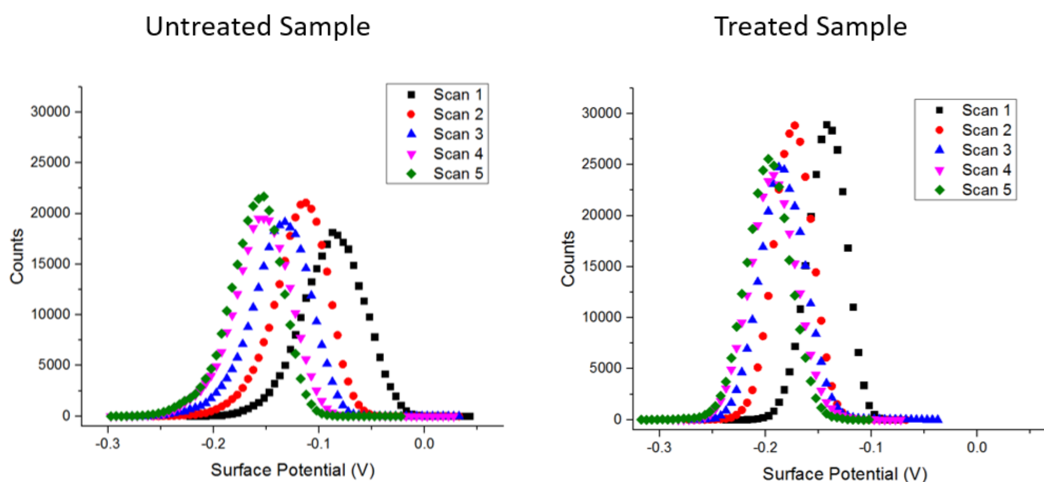

Figure 3.5: Individual surface potential histograms that comprise Figure 3.4 in the main text. The data from each scan was distributed into 5 mV bins.

The above diagrams are taken from surface potential data of the nominally 100 nm films. $(10\ \mu m)^2$ scans were taken with $(512)^2$ point resolution at 5 different locations for both the untreated (right) and treated (left) substrate. The native oxide silicon substrates were both cleaned with the same procedures noted in the main text and the treated substrate was passivated with Hexamethyldisilazane (HMDS) prior to organic molecular beam deposition. diF-TES-ADT was deposited onto both substrates simultaneously to ensure equal film thickness between samples. To create Figure 4 in the main text, each histogram of the set was centered about its

mean and then added together. Differences in mean for individual scans is attributed the change in tip-sample capacitance as the location of scan changes. This is a typical feature of KPFM where the absolute work function of the cantilever tip is usually unknown and subject to subtle shifts.

3.6 References

1. C. Wang, H. Dong, W. Hu, Y. Liu and D. Zhu, Chemical Reviews **112** (4), 2208-2267 (2012).

2. A. Mishra and P. Bäuerle, Angewandte Chemie International Edition **51** (9), 2020-2067 (2012).

3. N. Tessler, Y. Preezant, N. Rappaport and Y. Roichman, Advanced Materials **21** (27), 2741-2761 (2009).

4. S. Reineke, F. Lindner, G. Schwartz, N. Seidler, K. Walzer, B. Lussem and K. Leo, Nature **459** (7244), 234-238 (2009).

5. J.-H. Jou, S. Kumar, A. Agrawal, T.-H. Li and S. Sahoo, Journal of Materials Chemistry C **3** (13), 2974-3002 (2015).

6. C. J. Brabec, S. Gowrisanker, J. J. M. Halls, D. Laird, S. Jia and S. P. Williams, Advanced Materials **22** (34), 3839-3856 (2010).

7. Y. Lin, Y. Li and X. Zhan, Chemical Society Reviews **41** (11), 4245-4272 (2012).

8. J. Zhao, Y. Li, G. Yang, K. Jiang, H. Lin, H. Ade, W. Ma and H. Yan, Nature Energy **1**, 15027 (2016).

9. E. G. Bittle, J. I. Basham, T. N. Jackson, O. D. Jurchescu and D. J. Gundlach, Nature Communications **7**, 10908 (2016).

10. M. Schwoerer and H. C. Wolf, in *Organic Molecular Solids* (Wiley-VCH Verlag GmbH, 2008), pp. 217-305.

11. M. Pope and C. E. Swenberg, Annual Review of Physical Chemistry **35** (1), 613-655 (1984).

12. L. G. Kaake, P. F. Barbara and X. Y. Zhu, The Journal of Physical Chemistry Letters **1** (3), 628-635 (2010).

13. K. Puntambekar, J. Dong, G. Haugstad and C. D. Frisbie, Advanced Functional Materials **16** (7), 879-884 (2006).

14. M. J. Jaquith, J. E. Anthony and J. A. Marohn, Journal of Materials Chemistry **19** (34), 6116-6123 (2009).

15. S. Verlaak, C. Rolin and P. Heremans, The Journal of Physical Chemistry B **111** (1), 139-150 (2007).

16. W. Kalb, P. Lang, M. Mottaghi, H. Aubin, G. Horowitz and M. Wuttig, Synthetic Metals **146** (3), 279-282 (2004).

17. J. H. Kang, D. d. S. Filho, J.-L. Bredas and X.-Y. Zhu, Applied Physics Letters **86** (15), 152115 (2005).

18. W. L. Kalb, S. Haas, C. Krellner, T. Mathis and B. Batlogg, Physical Review B **81** (15), 155315 (2010).

19. S. R. Walter, J. Youn, J. D. Emery, S. Kewalramani, J. W. Hennek, M. J. Bedzyk, A. Facchetti, T. J. Marks and F. M. Geiger, Journal of the American Chemical Society **134** (28), 11726-11733 (2012).

20. M.-H. Yoon, C. Kim, A. Facchetti and T. J. Marks, Journal of the American Chemical Society **128** (39), 12851-12869 (2006).

21. S. Yogev, E. Halpern, R. Matsubara, M. Nakamura and Y. Rosenwaks, Physical Review B **84** (16), 165124 (2011).

22. T. Richards, M. Bird and H. Sirringhaus, The Journal of Chemical Physics **128** (23), 234905 (2008).

23. F. Dinelli, M. Murgia, P. Levy, M. Cavallini, F. Biscarini and D. M. de Leeuw, Physical Review Letters **92** (11), 116802 (2004).

24. J. J. Brondijk, W. S. C. Roelofs, S. G. J. Mathijssen, A. Shehu, T. Cramer, F. Biscarini, P. W. M. Blom and D. M. de Leeuw, Physical Review Letters **109** (5), 056601 (2012).

25. W. S. C. Roelofs, S. G. J. Mathijssen, R. A. J. Janssen, D. M. de Leeuw and M. Kemerink, Physical Review B **85** (8), 085202 (2012).

26. E. M. Muller and J. A. Marohn, Advanced Materials **17** (11), 1410-1414 (2005).

27. T. Hallam, C. M. Duffy, T. Minakata, M. Ando and H. Sirringhaus, Nanotechnology **20** (2), 025203 (2009).

28. S. Subramanian, S. K. Park, S. R. Parkin, V. Podzorov, T. N. Jackson and J. E. Anthony, Journal of the American Chemical Society **130** (9), 2706-2707 (2008).

29. S. K. Park, D. A. Mourey, S. Subramanian, J. E. Anthony and T. N. Jackson, Applied Physics Letters **93** (4), 043301 (2008).

30. O. D. Jurchescu, S. Subramanian, R. J. Kline, S. D. Hudson, J. E. Anthony, T. N. Jackson and D. J. Gundlach, Chemistry of Materials **20** (21), 6733-6737 (2008).

31. S. Hunter, J. Chen and T. D. Anthopoulos, Advanced Functional Materials **24** (38), 5969-5976 (2014).

32. L. C. Teague, B. H. Hamadani, O. D. Jurchescu, S. Subramanian, J. E. Anthony, T. N. Jackson, C. A. Richter, D. J. Gundlach and J. G. Kushmerick, Advanced Materials **20** (23), 4513-4516 (2008).

33. M. Nonnenmacher, M. P. O'Boyle and H. K. Wickramasinghe, Applied Physics Letters **58** (25), 2921-2923 (1991).

34. W. Melitz, J. Shen, A. C. Kummel and S. Lee, Surface Science Reports **66** (1), 1-27 (2011).

35. J. L. Neff and P. Rahe, Physical Review B **91** (8), 085424 (2015).

36. B. D. Terris, J. E. Stern, D. Rugar and H. J. Mamin, Physical Review Letters **63** (24), 2669-2672 (1989).

37. A. Hinaut, F. Chaumeton, D. Martrou and S. Gauthier, in *Imaging and Manipulation of Adsorbates Using Dynamic Force Microscopy: Proceedings from the AtMol Conference Series, Nottingham, UK, April 16-17, 2013*, edited by P. Moriarty and S. Gauthier (Springer International Publishing, Cham, 2015), pp. 131-151.

38. P. B. Hoffmann, A. G. Gagorik, X. Chen and G. R. Hutchison, The Journal of Physical Chemistry C **117** (36), 18367-18374 (2013).

39. D. J. Ellison, B. Lee, V. Podzorov and C. D. Frisbie, Advanced Materials **23** (4), 502-507 (2011).

40. F. Schreiber, Physica Status Solidi (a) **201** (6), 1037-1054 (2004).

41. H. Alexander, B. Wim, G. James, S. Eric, G. Eliot, K. Rick, M. Alastair, C. Matthew, R. Bruce and P. Howard, Journal of Physics: Conference Series **247** (1), 012007 (2010).

42. D.-M. Smilgies and D. R. Blasini, Journal of Applied Crystallography **40** (4), 716-718 (2007).

43. S. Duhm, G. Heimel, I. Salzmann, H. Glowatzki, R. L. Johnson, A. Vollmer, J. P. Rabe and N. Koch, Nature Materials **7** (4), 326-332 (2008).

44. R. Li, J. W. Ward, D.-M. Smilgies, M. M. Payne, J. E. Anthony, O. D. Jurchescu and A. Amassian, Advanced Materials **24** (41), 5553-5558 (2012).

45. S. M. Huston, J. Wang, T. McAfee, M. Loth, J. E. Anthony, H. W. Ade, B. R. Conrad and D. B. Dougherty, Crystal Growth & Design **15** (2), 822-828 (2015).

46. Y. Wu, G. Haugstad and C. D. Frisbie, The Journal of Physical Chemistry C **118** (5), 2487-2497 (2014).

47. M. Tello, M. Chiesa, C. M. Duffy and H. Sirringhaus, Advanced Functional Materials **18** (24), 3907-3913 (2008).

48. S. Yogev, R. Matsubara, M. Nakamura, U. Zschieschang, H. Klauk and Y. Rosenwaks, Physical Review Letters **110** (3), 036803 (2013).

49. R. Noriega, J. Rivnay, K. Vandewal, F. P. V. Koch, N. Stingelin, P. Smith, M. F. Toney and A. Salleo, Nature Materials **12** (11), 1038-1044 (2013).

Chapter 4

Temperature Controlled Interlayer Disorder in Ultrathin Films of α-Sexithiophene

Benjamin C. Hoffman,[†‡] Terry Mcafee,[‡⁑] Sara Pazoki,[†‡] Aubrey Apperson,[†‡] Brendan O'Connor,[‡※] and Daniel B. Dougherty[†‡]

[†] Department of Physics, North Carolina State University, Raleigh, North Carolina 27695, United States
[‡] Organic and Carbon Electronics Lab (ORaCEL), North Carolina State University, Raleigh, North Carolina 27695, United States
[⁑] Tulane University, New Orleans, Louisiana 70118, United States
[※] Department of Mechanical and Aerospace Engineering, North Carolina State University, Raleigh, North Carolina 27695, United States

Abstract

The surface potential difference between the first and second layer of α-sexithiophene (6T) films on silane passivated SiO_2 is observed using Kelvin Probe Force Microscopy. The relative surface potential changes sign depending on whether the films are grown at 70°C or 120°C substrate temperature. Complementary wide angle X-ray scattering observations show that this difference can be interpreted as the result of a higher concentration of interlayer hole traps due to poor out-of-plane ordering in films deposited at lower temperature. Molecular sliding and shifts in tilt angle are proposed as the microscopic origin of out-of-plane disorder leading to trapped charges.

4.1 Introduction

The rise of organic semiconducting (OSC) electronics has brought much excitement from its use of synthetically produced novel materials, where electronic and optical properties can be tuned using molecular substitutions[1, 2]. Solid state processing of these materials can be carried out at low temperatures over large areas offering a low-energy production alternative to traditional inorganic semiconductor devices[3, 4]. A challenge is that charge transport between OSC small molecules, even in a well-ordered crystal, is determined by weak interactions susceptible to charge trapping from a wide variety of sources[5] and complicated by many competing interactions[6].

The organic field-effect transistor (OFET) has proved to be a useful device to probe electronic properties of small molecule films and single crystals. Remarkably, fully-functional transistors with only a single monolayer have been created[7, 8]. Moreover, these structures can be engineered to form complex integrated circuits[9]. In all OFET's, the active layer in the channel is known to be very close to the insulating dielectric where the gate bias is applied. By studying OSC's which exhibit layer-by-layer growth, where the first monolayer completes coverage prior to the onset of the second layer, it has been directly shown that charge transport occurs primarily in the first two monolayers nearest the dielectric[8]. After the second monolayer, the field effect mobility in an α-sexithiophene transistor saturates and subsequent layers do not enhance charge transport. This present report will address the electrostatic traps that occur at the interface between the first and second layer in similar α-sexithiophene films.

The organic small molecule α-sexithiophene (6T) is a conjugated oligomer that is a close relative of polythiophene polymers. 6T has been studied extensively in organic thin film transistors[10, 11] where it has been used to address fundamental questions such as temperature dependence of carrier mobility[12], shifting threshold voltages from gate stress[13] and thickness[14], the impact of sidechain substitutions[15], and the 2D to 3D electronic transition related to film thickness[16]. Outside of transistors, 6T has also been used in photovoltaic devices as a model donor layer[17] and for use of pre-patterning to control morphology.[18, 19] Substrate induced polymorphism[20] has been widely reported in films of 6T. Capable of forming many possible structures[21], 6T films are sensitive to deposition flux[8, 22], substrate temperature[23, 24], and other parameters[25, 26] resulting in many complex combinations of co-existing phases.

In this paper, we apply Kelvin Probe Force Microscopy to the first and second layers of 6T films grown on silane passivated SiO_2 substrates. We show that the electrostatic potential difference between the first and second layer changes sign and magnitude when the substrate growth temperature is increased from 70 °C to 120 °C. Grazing incidence X-ray scattering observations on the same films show that this difference can be attributed to the out-of-plane disorder in films deposited at lower temperature. The significance of this finding is in clarifying the magnitude of electrostatic effects that can be caused by minor interlayer disorder in organic transistors.

4.2 Experimental Methods

All substrates used in this experiment were 300 nm thick $Si0_2$ on n-type doped Si (100) cleaned by acetone sonication, isopropyl sonication, UV ozone, DI water rinse, and then blown

dry with N_2. Substrates were chemically treated with hexamethyldisilazane (HMDS) to enhance film growth. They were heated at 120°C for 30 min., spin-coated with HMDS (2000 rpm for 60 sec.), and then heated again (120°C for 30 min.) in a dry glove box with $O_2 < 10$ ppm, $H_20 < 0.1$ ppm. Water contact angle measurements exhibit a 50±1° increase after HMDS passivation, indicating an overall reduction in surface free energy of the substrate. This effect persists even after vacuum annealing under the same conditions employed during film growth.

Molecular films were grown using organic molecular beam deposition[27] (OMBD). Substrates were loaded into a vacuum chamber (2.0×10^{-6} Torr) suspended upside down above a quartz crucible wrapped with tungsten wire and filled with 6T molecule purchased commercially (Sigma-Aldrich). Prior to deposition, the substrate was heated and allowed 30 min. to thermally equilibrate. An in-situ thermocouple attached to the substrate heater was used to confirm the temperature during deposition. The crucible was then heated to facilitate molecular sublimation while a quartz crystal microbalance (QCM) near the substrate was used to monitor flux (~ 0.03 Å/s). Film thickness was controlled via manual shutter during stable flux conditions. Organic films produced by this method are well-ordered and exhibit layer-by-layer type growth, enabling precise control of morphology.

Sample topography and surface potential were characterized simultaneously using Amplitude-Modulated Kelvin Probe Force Microscopy[28] (AM-KPFM) with a commercial instrument (MFP-3D, Asylum Research) and conductive cantilever probes (Budget Sensors ElectriMulti75-G) as described in a previous report[29]. During the scan, a bias = 0V was applied to the silicon substrate and slow scan speeds (= 0.3 Hz) were used to mitigate any dynamic

charging. Trace and retrace scans were compared to ensure scan stability. The height retracted to determine the contact potential difference (CPD) is 5 nm and the scan resolution is 1024 x 1024 points and lines. Several different regions of the sample were checked to ensure homogeneity across the film. Multiple samples were fabricated under identical conditions to confirm the reproducibility of reported effects.

It should be noted that if the sample being scanned with KPFM is a metal, then the CPD equates simply to the work function difference between the tip and sample.[30] In the case of OSC films the interpretation of CPD is more complex and any charges on the tip or in the film will contribute to the observed surface potential.[31] Furthermore, these observed excess charges will be of opposite sign than those that are actually present in the film[32] due to the image potential formed in the probe itself. In this context, KPFM images can be related to the distribution of trapped charge in the film.[29]

Grazing-incidence wide-angle x-ray scattering (GIWAXS) data was collected at the Stanford Synchrotron Radiation Light Source (SSRL) beam line 11–3 with an area detector (Rayonix mar CCD225), an energy of 12.735 keV, and an incidence angle of ≈ 0.12°. KPFM scans were conducted prior to GIWAXS analysis to prevent beam damage from influencing measurements.

4.3 Results and Discussion

This study focuses on ultrathin 6T films grown on substrates heated to 70°C and 120°C during OMBD. Substrate temperature was varied to control interlayer ordering and to vary the complex distribution of competing structural phases.[24] Films deposited at both temperatures were grown to the same nominal thickness under the same conditions with an AFM-calibrated QCM

reading. In some disordered areas of the films the exposed substrate is sometimes visible further confirming the film thickness.

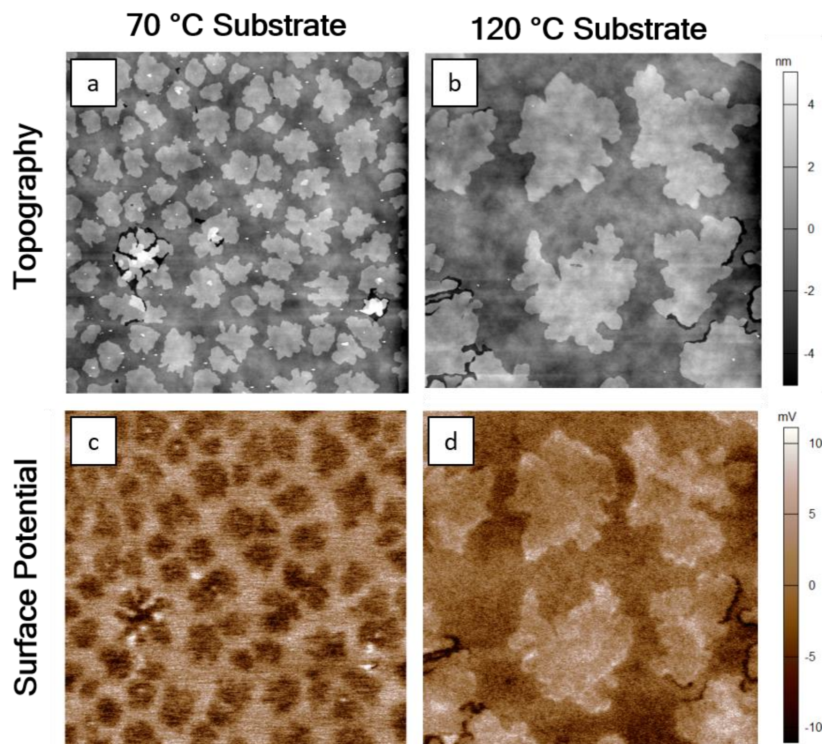

Figure 4.1: (10 μm)^2 images (a) and (b) are topography and the corresponding surface potential scans are (c) and (d). The sample grown on 70 °C substrate are (a) and (c) while the 120 °C substrate sample is shown in (b) and (d).

Figure 1 shows KPFM scans of two samples grown at different temperatures. Topography (Figures 1a and 1b) scans show an incomplete bilayer on top of a nearly complete monolayer in which the morphology is consistent with previous reports.[33, 34] Generally, the root-mean-square (RMS) roughness of the films is around 1.54 nm with little difference between roughness of the monolayer and bilayer. This roughness is statistically higher than that of the bare substrate, which is approximately 0.72 nm. The increase in roughness within the film is

attributed to the existence of concurrent phases in the OSC film. The underlying substrate is visible in some small areas of morphological disorder which reveal the HMDS/SiO_2 substrate underneath, but the first monolayer coverage is nearly complete. Substrate temperature has a clear impact on growth kinetics, apparent from the bilayer island size and bilayer nucleation density. Films grown on the higher temperature substrate have markedly larger bilayer islands. The CPD maps in Figure 1c and 1d shows that the electrostatic landscape is strongly affected by the different film growth conditions. Both surface potential distributions in the CPD images have been normalized and displayed with the same range. Only relative magnitudes within individual images are considered and absolute CPD value variation between samples is not considered. For the lower deposition temperature sample, the bi-layer islands exhibit a lower surface potential than the surrounding monolayer, while the reverse is apparent in the higher temperature samples. Surface potential differences are observed to be -4.9 ± 3.6 mV, 4.2 ± 3.2 mV between means of the first and second layer for the 70°C and 120°C samples, respectively. Similar studies of pentacene thin films[35] have concluded that bilayer islands are generally of higher surface potential than the underlying mono-layer. The implications of these shifts in interlayer surface potentials will be considered further in subsequent paragraphs, but we will first describe structural characterization of the films in Figure 1.

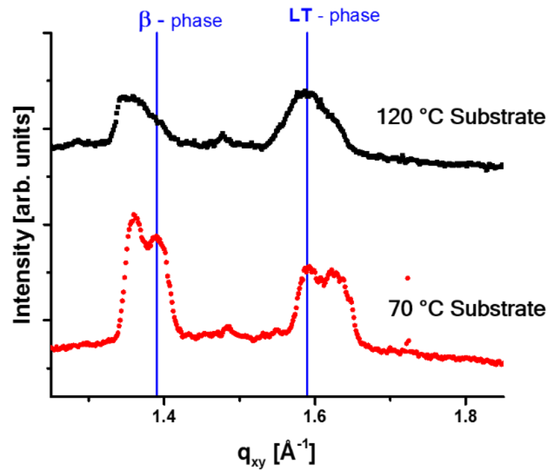

Figure 4.2: In-plane GIWAXS data of 6T grown with different substrate temperatures; red data points for the 70 °C sample and black points for 120 °C sample. The blue lines indicate the values associated with the β and LT (020) phases of 6T.

Characterization by GIWAXS provides important information about the crystal structure and ordering associated with the samples observed with AFM and KPFM. As shown in Figure 2, evidence for both expected polymorphs for 6T, the β (q_{xy} = 1.39 $Å^{-1}$) and LT (020) (q_{xy} = 1.59 $Å^{-1}$) phases, are present in the in-plane data for the thin films. This polymorphism in the range of the studied substrate temperature is in agreement with earlier published GIWAXS observations even in the ultrathin film regime considered here.[24] The so-called LT phase[36] corresponds to a thermodynamically stable upright orientation. The β-phase[22] is also upright but is less stable and associated with a frozen smectic state that is slightly preferred in the first few layers.

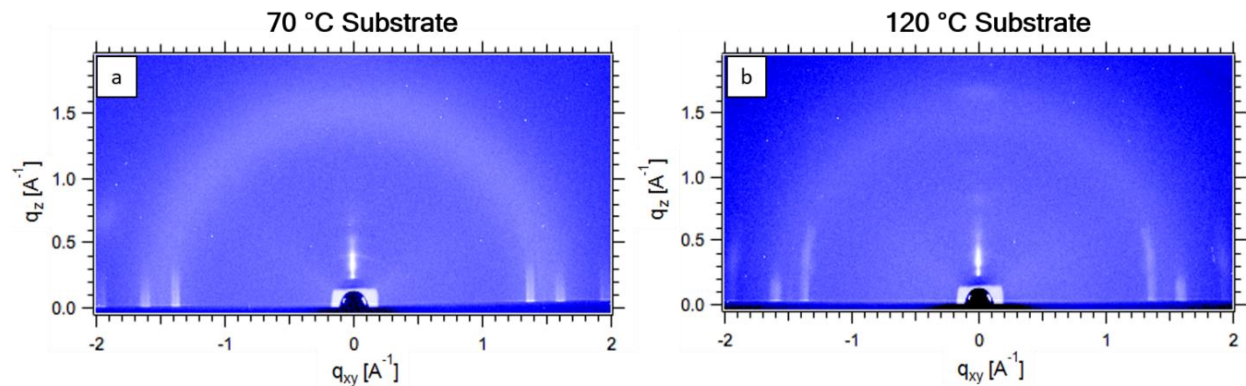

Figure 4.3: 2D WAXS data associated with the 70 °C sample (a) and the 120 °C sample (b).

Considering the full 2D scattering pattern from GIWAXS, as shown in Figure 3, there are significant differences in the out-of-plane scattering peaks observed for the 120 °C compared to the 70 °C sample. This is seen in Figure 3a and 3b by comparing the scattering intensity near the vertical q_z axis. For the 70 °C sample, see Figure 3a, the only structure intersecting the q_z axis is a diffuse ring, which is from the 300 nm $Si0_2$ layer on the substrate surface. By contrast, several isolated scattering spots are present along the q_z axis for the 120 °C film, see figure 3b. Having little out-of-plane order in the 70 °C bilayer film indicates there is little crystal structure alignment between the two layers of the sample[37]. In other words, there is far less out-of-plane order for the film deposited at 70 °C. It is also worth mentioning that there is no evidence for flat-lying molecules based on the absence of diffraction peaks in the low in-plane q_{xy}

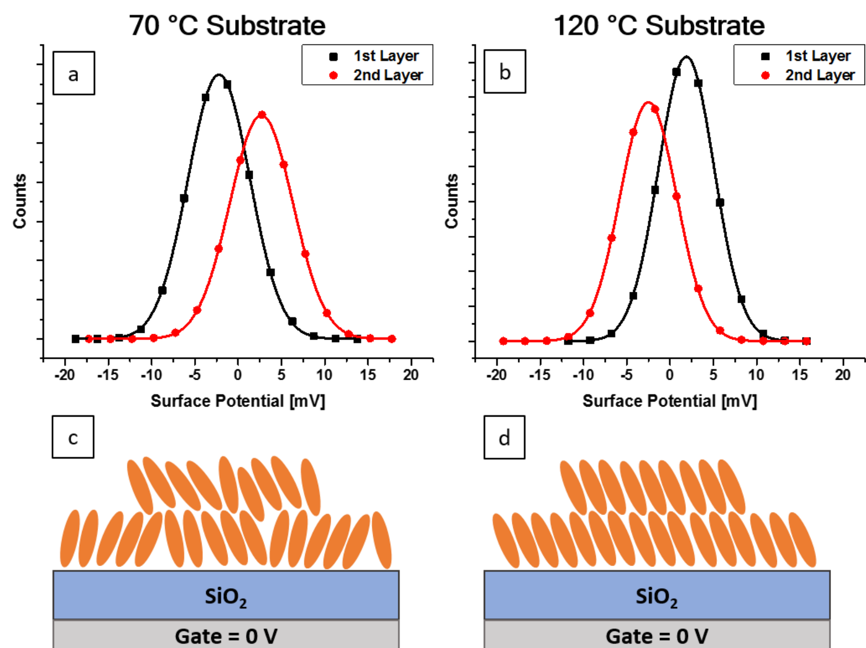

Figure 4.4: (a) and (b) are histograms of surface potential data shown in figures (1c) and (1d), respectively, with data separated between the 1st and 2nd monolayers. (c) and (d) are schematics of the proposed model to explain the shifts in surface potential.

Figures 4a and 4b are histograms of the surface potential data shown in Figure 1c and 1d, respectively. A mask was created over the topography scan, Figure 1a and 1b, to isolate morphological features which then was copied onto the surface potential scan. By doing this, the tip-sample contact potential difference of the mono- and bi-layer can be analyzed separately. Next, all the surface potential data was multiplied by negative one in order to represent the true sign of the charges.[38] These distributions of CPD data associated with the separate layers are fit by single-peak Gaussians indicated by the solid red and black lines in the histogram graphs. Relating these histogram results to the GIWAXS observations, Figure 4c and 4d are schematic depictions of the origin of electrostatic potential differences for different deposition

temperatures. The films grown at a higher substrate temperature are more well-ordered in the out-of-plane direction. By contrast, the lack of order in the out-of-plane direction for films deposited at 70 °C can be presumed to lead to interlayer charge traps. Indeed, the negative potential difference observed between the first and second layer is consistent with an accumulation of holes near the low temperature bilayer islands.

The idea that vertical disorder in molecular positions relative to the substrate in a very thin layer can lead to charge traps has precedence in the literature.[39] Kang et al, showed evidence for point molecular sliding defects in pentacene monolayers.[40] Semi-empirical calculations attributed the origin of shallow trap states to these defects. Subsequently, molecular sliding defects have been found in a number of different systems.[41, 42] In the case of 6T, sliding defects were seen to have negligible effect in comparison to extrinsic factors, using scanning tunneling spectroscopy (STS) measurements with ~10 meV experimental precision.[42] This observation on a different type of 6T is still possibly consistent with the picture we have developed here since the interlayer potential differences between first and second layer are small. The connection between KPFM and STS is not quantitative since the STS studies probe density of states not surface potential.

There is another important connection to consider: the orientation dependence of electrostatic potential outside of anisotropic small molecules. Duhm et al. have shown using photoemission and calculations that the anisotropy of potential outside of 6T can lead to significant orientation-dependence of ionization potentials.[25] Small random variations in 6T tilt angle in the two layers in our study could give rise to the lack of out-of-plane order and

associated potential variations. Our experiments cannot distinguish between the two possible microscopic origins of out-of-plane disorder (molecular sliding or random tilt angle) and we see no reason why both would not be significant contributors to the observed behavior. The crucial point is that very subtle microscopic structural details can give rise to notable electrical effects near the active (accumulation) region of an organic thin film transistor.

4.4 Summary and Conclusion

Ultrathin films of the organic molecule 6T are produced with OMBD on an SiO_2 substrate that is heated during the growth. By changing the substrate temperature during deposition, the CPD of bilayer islands observed using KPFM reverses sign with respect to the monolayer. GIWAXS scattering peaks show that films grown at lower temperature, which exhibit lower relative bilayer surface potential by KPFM, also have poor out-of-plane order. This illustrates the electrostatic impact of small interlayer disorder that can trap charge and modify local electrostatic potentials.

Interlayer potential difference caused by disorder are very significant for field effect transistor operation, which is controlled by only a few layers near the gate dielectric. Evidently, relatively minor changes in processing conditions can lead to measurable qualitative changes in interlayer electrostatics. The device impact of these electrostatic details remain to be characterized and would be best assessed in the context of small-molecule 2D transistors such as described by Brondijk et al.[16] A simple hypothesis derived from our observations is that the trap density in the 2D channel would be sensitive to film growth temperature. However, the fact that interlayer potential differences change sign in our experiments suggests that more precise

modeling of the density of trap states may be required to capture all of the effects of interlayer disorder.

Acknowledgments

Film growth and scanned probe microscopy was funded by NSF CAREER award DMR-1056861. GIWAXS measurements at the Stanford Synchrotron Radiation Lightsource (SSRL) were funded by NSF CAREER award CMMI-1554322. SSRL is a directorate of SLAC National Accelerator Laboratory, and an Office of Science User Facility operated for the U.S. Department of Energy Office of Science by Stanford University. We gratefully thank Dr. Michael F. Toney and Dr. R. Joseph Kline for their assistance with the X-ray diffractions measurements.

4.5 References

1. C. Wang, H. Dong, W. Hu, Y. Liu and D. Zhu, Chemical Reviews **112** (4), 2208-2267 (2012).

2. P. M. Beaujuge and J. M. J. Fréchet, Journal of the American Chemical Society **133** (50), 20009-20029 (2011).

3. F. C. Krebs, T. Tromholt and M. Jorgensen, Nanoscale **2** (6), 873-886 (2010).

4. A. C. Arias, J. D. MacKenzie, I. McCulloch, J. Rivnay and A. Salleo, Chemical Reviews **110** (1), 3-24 (2010).

5. W. L. Kalb, S. Haas, C. Krellner, T. Mathis and B. Batlogg, Physical Review B **81** (15), 155315 (2010).

6. N. Tessler, Y. Preezant, N. Rappaport and Y. Roichman, Advanced Materials **21** (27), 2741-2761 (2009).

7. G. S. Tulevski, Q. Miao, M. Fukuto, R. Abram, B. Ocko, R. Pindak, M. L. Steigerwald, C. R. Kagan and C. Nuckolls, Journal of the American Chemical Society **126** (46), 15048-15050 (2004).

8. F. Dinelli, M. Murgia, P. Levy, M. Cavallini, F. Biscarini and D. M. de Leeuw, Physical Review Letters **92** (11), 116802 (2004).

9. E. C. P. Smits, S. G. J. Mathijssen, P. A. van Hal, S. Setayesh, T. C. T. Geuns, K. A. H. A. Mutsaers, E. Cantatore, H. J. Wondergem, O. Werzer, R. Resel, M. Kemerink, S. Kirchmeyer, A. M. Muzafarov, S. A. Ponomarenko, B. de Boer, P. W. M. Blom and D. M. de Leeuw, Nature **455** (7215), 956-959 (2008).

10. G. Horowitz, D. Fichou, X. Peng, Z. Xu and F. Garnier, Solid State Communications **72** (4), 381-384 (1989).

11. G. Horowitz, F. Garnier, A. Yassar, R. Hajlaoui and F. Kouki, Advanced Materials **8** (1), 52-54 (1996).

12. G. Horowitz, R. Hajlaoui and P. Delannoy, J. Phys. III France **5** (4), 355-371 (1995).

13. H. L. Gomes, P. Stallinga, F. Dinelli, M. Murgia, F. Biscarini, D. M. d. Leeuw, T. Muck, J. Geurts, L. W. Molenkamp and V. Wagner, Applied Physics Letters **84** (16), 3184-3186 (2004).

14. F. V. Di Girolamo, C. Aruta, M. Barra, P. D'Angelo and A. Cassinese, Applied Physics A **96** (2), 481-487 (2009).

15. F. Garnier, A. Yassar, R. Hajlaoui, G. Horowitz, F. Deloffre, B. Servet, S. Ries and P. Alnot, Journal of the American Chemical Society **115** (19), 8716-8721 (1993).

16. J. J. Brondijk, W. S. C. Roelofs, S. G. J. Mathijssen, A. Shehu, T. Cramer, F. Biscarini, P. W. M. Blom and D. M. de Leeuw, Physical Review Letters **109** (5), 056601 (2012).

17. K. Cnops, B. P. Rand, D. Cheyns, B. Verreet, M. A. Empl and P. Heremans, Nature Communications **5**, 3406 (2014).

18. C. Lorch, R. Banerjee, J. Dieterle, A. Hinderhofer, A. Gerlach, J. Drnec and F. Schreiber, The Journal of Physical Chemistry C **119** (40), 23211-23220 (2015).

19. G. D'Avino, L. Muccioli and C. Zannoni, Advanced Functional Materials **25** (13), 1985-1995 (2015).

20. A. O. F. Jones, B. Chattopadhyay, Y. H. Geerts and R. Resel, Advanced Functional Materials **26** (14), 2233-2255 (2016).

21. R. G. Della Valle, E. Venuti, A. Brillante and A. Girlando, The Journal of Physical Chemistry A **112** (29), 6715-6722 (2008).

22. A. Moser, I. Salzmann, M. Oehzelt, A. Neuhold, H.-G. Flesch, J. Ivanco, S. Pop, T. Toader, D. R. T. Zahn, D.-M. Smilgies and R. Resel, Chemical Physics Letters **574**, 51-55 (2013).

23. B. Servet, G. Horowitz, S. Ries, O. Lagorsse, P. Alnot, A. Yassar, F. Deloffre, P. Srivastava and R. Hajlaoui, Chemistry of Materials **6** (10), 1809-1815 (1994).

24. C. Lorch, R. Banerjee, C. Frank, J. Dieterle, A. Hinderhofer, A. Gerlach and F. Schreiber, The Journal of Physical Chemistry C **119** (1), 819-825 (2015).

25. S. Duhm, G. Heimel, I. Salzmann, H. Glowatzki, R. L. Johnson, A. Vollmer, J. P. Rabe and N. Koch, Nature Materials **7** (4), 326-332 (2008).

26. L. Pithan, C. Cocchi, H. Zschiesche, C. Weber, A. Zykov, S. Bommel, S. J. Leake, P. Schäfer, C. Draxl and S. Kowarik, Crystal Growth & Design **15** (3), 1319-1324 (2015).

27. S. Kowarik, A. Gerlach and F. Schreiber, Journal of Physics: Condensed Matter **20** (18), 184005 (2008).

28. M. Nonnenmacher, M. P. O'Boyle and H. K. Wickramasinghe, Applied Physics Letters **58** (25), 2921-2923 (1991).

29. B. C. Hoffman, T. McAfee, B. R. Conrad, M. A. Loth, J. E. Anthony, H. W. Ade and D. B. Dougherty, ACS Applied Materials & Interfaces **8** (33), 21490-21496 (2016).

30. A. Subrahmanyam and S. Kumar, *The Kelvin Probe for Surface Engineering: Fundamentals and Design*. (Ane Books, 2010).

31. J. L. Neff and P. Rahe, Physical Review B **91** (8), 085424 (2015).

32. A. Hinaut, F. Chaumeton, D. Martrou and S. Gauthier, in *Imaging and Manipulation of Adsorbates Using Dynamic Force Microscopy: Proceedings from the AtMol Conference Series, Nottingham, UK, April 16-17, 2013*, edited by P. Moriarty and S. Gauthier (Springer International Publishing, Cham, 2015), pp. 131-151.

33. M. A. Loi, E. da Como, F. Dinelli, M. Murgia, R. Zamboni, F. Biscarini and M. Muccini, Nature Materials **4** (1), 81-85 (2005).

34. E. Da Como, M. A. Loi, F. Dinelli, M. Murgia, F. Biscarini, R. Zamboni and M. Muccini, Synthetic Metals **155** (2), 287-290 (2005).

35. Y. Wu, G. Haugstad and C. D. Frisbie, The Journal of Physical Chemistry C **118** (5), 2487-2497 (2014).

36. G. Horowitz, B. Bachet, A. Yassar, P. Lang, F. Demanze, J.-L. Fave and F. Garnier, Chemistry of Materials **7** (7), 1337-1341 (1995).

37. P. Müller-Buschbaum, Advanced Materials **26** (46), 7692-7709 (2014).

38. F. Fuchs, F. Caffy, R. Demadrille, T. Mélin and B. Grévin, ACS Nano **10** (1), 739-746 (2016).

39. L. G. Kaake, P. F. Barbara and X. Y. Zhu, The Journal of Physical Chemistry Letters **1** (3), 628-635 (2010).

40. J. H. Kang, D. d. S. Filho, J.-L. Bredas and X.-Y. Zhu, Applied Physics Letters **86** (15), 152115 (2005).

41. D. B. Dougherty, W. Jin, W. G. Cullen, J. E. Reutt-Robey and S. W. Robey, Applied Physics Letters **94** (2), 023103 (2009).

42. J. Wang and D. B. Dougherty, Journal of Vacuum Science & Technology B, Nanotechnology and Microelectronics: Materials, Processing, Measurement, and Phenomena **32** (3), 030601 (2014).

Chapter 5

Shallow Charge Trap Instability After Transition in a 2-Dimensional Organic Field Effect Transistor

Benjamin C. Hoffman,[†‡] Sara Pazoki,[†‡] Aubrey Apperson,[†‡] and Daniel B. Dougherty[†‡]

[†] Department of Physics, North Carolina State University, Raleigh, North Carolina 27695, United States
[‡] Organic and Carbon Electronics Lab (ORaCEL), North Carolina State University, Raleigh, North Carolina 27695, United States

Abstract

In an investigation into the electronic structure of an operational 2-dimensional organic field effect transistor (2D OFET) of α-sexithiophene (6T), surface potential distributions were measured with KPFM for a range of gate biases. This is traditionally done by measuring the surface potential of a single point and shifting the bias of the sample incrementally. By scanning a large area and then shifting the applied biases, the spatial variations can be better quantified. ‘On’ and ‘off’ states are observed in the mean surface potential from each image and the transition between these regimes is used to compute the trap density of states (DOS). Histograms of CPD in the ‘on’ and ‘off’ regions reveal two distinct peaks related to the intrinsic work function and deep trap states. The data collected shows that the ‘off’ regime is static whereas the ‘on’ regime is dynamic and screens the presence of deep traps. This dynamic ‘on’ state

shows active trapping and thermal release of shallow trap states. Most previously collected data does not include a clear view of this trait, and researchers whose data does allow for observation of this process have tended to leave the results underemphasized in their overall assessment of charge traps.

5.1 Introduction

Even with major advances in organic electronics in previous decades, there are still many gaps in the scientific community's understanding of charge transport in disordered organic semiconductor (OSC) systems. For instance, we know that electronic disorder, manifesting as localized trap states, fundamentally limits charge transport[1, 2], but even single crystal devices with high mobility show the presence of these trap states.[3, 4] Nevertheless, there are many sophisticated theories regarding the charge transport in these OSC systems, which have been successful describing their mobility dependence on various parameters, like applied fields and temperature.[1] In transistors, charge accumulation occurs near the dielectric interface in the first several monolayers[5] so 2-dimensional organic field effect transistors (2D OFETs) are of particular interest. The goal of this report is to further our understanding of shallow trap dynamics through gate bias dependent surface potential analysis of the electronic transition at threshold voltage an operational 2D OFET.

For as much success as there has been with fabrication of ultrathin film OFETs[6] there is still uncertainty regarding charge transport and the role of electronic disorder in the regime nearest the interface.[7, 8] For example, Brondijk et al. showed that 2D confinement in the linear regime of OFET operation is possible using a single monolayer of small molecules to form the

active layer of a bottom-gate OFET channel.[7] Thicker films in the linear regime have 3D transport characteristics.[7] A later transport investigation in the saturation regime found that thick polymer films in a top-gate OFET geometry showed only 2D transport.[8] Though these two results are at odds, there are many subtle experimental differences between them that confuses a final conclusion to whether or not 2D confinement is always the case for OFETs. Nevertheless, charge distribution nearest the dielectric is an important regime that requires further investigation.

The small organic molecule used in this report is α-sexithiophene (6T), a benchmark molecule in the field of organic electronics used for many seminal works.[9, 10] 6T films are highly sensitive to many processing variables which has allowed for tuning of film properties accordingly, such as optimized mobility[11-13] and is actively studied for applications in both transistors[7] and photovoltaic devices[14]. 6T films can be controlled to grow in a layer-by-layer fashion which enables direct access to the monolayers closest to the dielectric interface. This growth process made this molecule the choice for the influential OFET transport studies mentioned previously that investigated layer dependent mobility[5] and 2D confinement.[7]

To measure the local surface potential of the ultrathin OSC films Kelvin probe force microscopy (KPFM) was used.[15] KPFM measures the local variation in work function and any trapped charge density in an organic film.[16, 17] Further studies using KPFM of organic films in a OFET geometry established a method to quantitatively measure the trap density of states (DOS) by manipulating the Fermi level of the active layer.[18, 19] This method involves grounding the source and drain and then using the gate bias to shift the HOMO with respect to the Fermi

energy. With sufficiently negative gate bias, V_{th}, the Fermi level, E_F, of the electrodes shifts into the highest occupied orbital-derived band of the active layer and thus holes begin to accumulate in the channel. After V_{th}, further decreasing the gate bias, V_G, causes a change in the number of holes accumulated in the active layer. Assuming a simple capacitor model and charge neutrality, this change in hole concentration, Δp, can be approximated by,

$$\Delta p = \frac{C_{ox}}{d_{org} q} [\Delta V_G - \Delta V_{SP}] \qquad (5.1)$$

where C_{ox} is the oxide capacitance per area, d_{org} is the thickness of the organic film, q is the elementary charge, ΔV_G is the difference between the applied V_G and V_{th}, and ΔV_{SP} is the difference between the measured V_{CPD} and the CPD at V_{th}. Assuming that the derivative of the Fermi-Dirac distribution with respect to the observed shift in energy can be approximated as a delta function, one can derive the following equation to calculate the trap DOS,

$$g(E) = \frac{\Delta p}{\Delta E_{HOMO}} = \frac{C_{ox}}{d_{org} q^2} \left[\left(\frac{dV_{CPD}}{dV_G} \right)^{-1} - 1 \right] \qquad (5.2)$$

where the density of states is a function of energy, $E = qV_{CPD}$. This analytic expression assumes nothing about the actual shape of the DOS and depends only on observable parameters.

The trap density of states (DOS) is a parameter well known to provide insight into charge transport as it relates to microstructure and energy level alignment.[20] This topic is of importance not only to transistors but to organic solar cells as well, where trap states can be related to the open circuit voltage[21]. The first uses of KPFM by to determine trap DOS demonstrated the effects of molecular doping to be a broadening of the DOS distribution and the introduction of smaller peaks indicating a complex electronic structure.[22] Smaller peaks in the range of shallow

traps can be alleviated through use of chemical passivation of the substrate as is consistent with improved growth kinetics enhancing device performance.[23, 24] For a scanned probe investigation of OFETs having a 2D film is important as only the first several layers contribute to charge transport and subsequent layers can lead to charge screening and the analysis becomes convoluted with bulk properties of the film.[19]

Charge carriers tunnel between localized and delocalized shallow trap states as they traverse from source to drain electrodes which is a process that limits optimal mobility. This trapping and detrapping of charge carriers can result in electrical noise in the transport current and is particularly relevant as a contributor to ubiquitous low frequency flicker (or 1/f) noise.[25] Carrier number fluctuations that result in 1/f noise have been correlated to microstructure[26] and general device performance[27] by using chemical treatment to control film growth kinetics. Furthermore, the highest noise level is associated with a gate bias near the threshold voltage.[27] Device geometry is also correlated with 1/f noise, but this is has been shown to be related to a higher concentration of defects at the metal-organic interface of the electrodes.[28] In light of these studies, charge trapping dynamics related to 1/f noise is a valuable predictor of device performance even though the origins of the defects can be complex.

In this chapter, the electrostatics of the OSC molecule 6T is studied in a 2D OFET geometry to investigate the CPD dependence on gate bias. In the ‘on’ regime, defined by a stabilized mean surface potential after threshold voltage, KPFM scans reveal a significant amount of CPD noise that is independent of any topographic cross-talk. This noise is related to the 1/f noise associated with charges tunneling between localized and delocalized states. Surface

potential data of the active layer around electronic transition at the threshold voltage reveals unique insights into the spatial resolution of shallow charge trap dynamics in a 2D OFET.

5.2 Experimental Methods

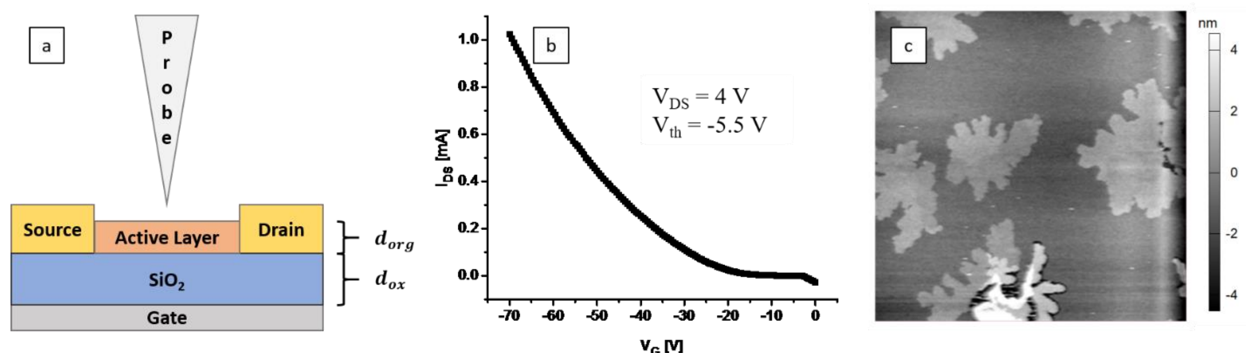

Figure 5.1: (a) Schematic of bottom-gate contact transistor geometry with AFM probe. (b) Transfer curve demonstrating operational transistor with measured threshold voltage. (c) Example topography image from featured scan series.

Samples in this study were bottom-gate OFET with alpha-sexithiophene as the active layer, a schematic of this configuration is depicted in Figure 5.1a. Silicon (100) wafers with 300 nm SiO_2 (from MTI) were cut and then cleaned with acetone, isopropyl, UV-O_3 exposure, DI water, and then blown dry with N_2. Clean substrates were then passivated with HMDS to enhance film growth. Source and drain electrodes, 5 nm Cr followed by 100 nm Au, were thermally evaporated, chamber pressure = 2.3 x 10^{-5} Torr, onto the substrates through a low density OFET shadow mask (Oscilla) to form channels with length and width of 25 µm and 950 µm, respectively. 6T was then deposited onto the FET chip using organic molecular beam deposition[29] in a chamber with a base pressure = 1.8 x 10^{-6} Torr. During deposition, the substrate was heated to 120 C and the temperature was monitored with an in-situ thermocouple. A QCM

was used to monitor the flux, = 0.03 Å/s, during the deposition and nominal deposition thickness, = 10 nm, which was controlled via manual shutter. The actual thickness of the resulting film in terms of completed monolayers was finely tuned with repeated growths and verified with AFM topography measurements.

Before and after KPFM analysis the transistor was measured in air with a probe station and Figure 5.1b shows the transfer characteristic for the OFET reported in this study. Transfer characteristics measured in the linear regime, V_{DS} = -4 V, show a clearly working transistor comparable to other published 6T linear transfer characteristics.[30] Linear regime was chosen over saturation to try and create a more similar measurement to the KPMF DOS procedure where drain and source are grounded. The threshold voltage was calculated using a second-derivative method where the first maximum of the derivative of the transconductance corresponds to a threshold voltage of V_{th} = -5.5 V [31, 32]. This value is in agreement with observations made with KPFM discussed in the results.

Dynamic AM-KPFM measurements were obtained with an MFP-3d in air using conductive cantilevers from budget sensors (ElectriMulti-75). For KPFM scans, both topography and contact potential difference (CPD) between sample and tip are measured point by point in a raster pattern over a given area. Measuring CPD is done by minimizing the electric field between tip and sample at a distance 5 nm retracted from the surface. The meaning of this value is singularly the work function difference if the sample is a metal, but any fields can be of influence in OSCs including any extra charge associated with the film. In analysis of CPD data, negative

one was multiplied to data to represent the true charge of the sample instead of the image potential which is recorded during KPFM measurement.

To directly measure the DOS of the trap states computable with Equation 5.2, a series of scans were recorded while varying the gate bias incrementally from $V_g = 0$ to -20 V by -0.1 V steps between scans. Figure 5.1c is a representative (8 μm)^2 topography image from the analyzed series of images described in the following paragraphs. A Keithley 2400 Sourcemeter was used to control source, drain, and gate biases. Before the first image, a negative bias was applied to the channel to turn the transistor on and evacuate any charges accumulated in the channel. The design of the shadow mask was for source/drain contacts that extend towards the edge of the substrate away from the channel. This allowed our use of an ORCA holder (Asylum Research) to continuously ground the source and drain but not interfere with the scanning process. The cantilever was aligned perpendicular to the length of the channel to mitigate stray field interaction from the electrodes with the tip during the electrical measurements. Long-term scan stability was ensured by using active vibration dampening shocks on a granite slab and housed in an acoustically insulating closed chamber. By tracking features in topography, drift during measurement was found to be negligible under stable conditions, only a few pixels during the entire scan series.

5.3 Results & Discussion

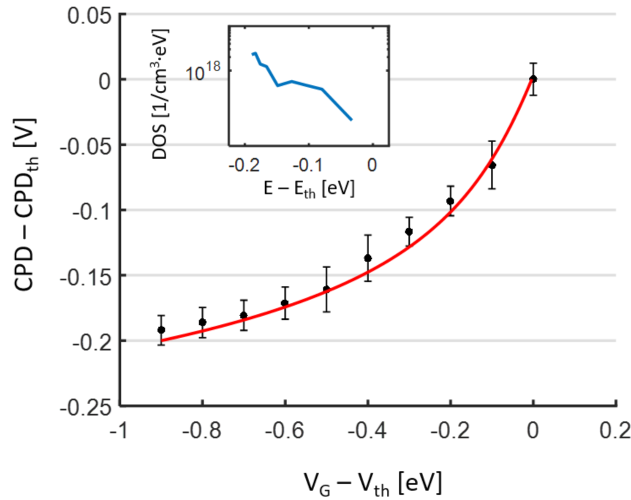

Figure 5.2: Observed surface potential at a given gate bias dependence relative to threshold voltage. The black data points are the mean and standard deviation of each individual KPFM scan. The red line is the exponential DOS fit described in Equation 5.4. The inset graph is the DOS computed directly from the average CPD values using Equation 5.2.

To quantify spatial variations in CPD, each image from the series was considered as a whole. Surface potential statistics from each image are valuable for the large number of data points, 256^2, contained. The black data points and error bars in the main plot of Figure 2 are the mean and standard deviation values of CPD associated with each image. By computing the numerical derivative of these means, Equation 5.2 can be applied to calculate the trap density of states. The results of this calculation are shown in the inset graph of Figure 5.2. Trap DOS shapes provide valuable information regarding the electronic disorder associated with OSC films. Because the standard deviation is large compared to the step size of V_G between images, error propagated through Equation 5.2 is large. As a way to avoid the extra error from fitting to the computed numerical derivative data we instead assumed a form of the DOS and then transformed

this fit to the observable Vg and CPD. The form of g(E) we assumed was an exponential according the widely-accepted formula,[33]

$$g(qV_{CPD}) = \frac{N_t}{E_U} e^{\frac{-qV_{CPD}}{E_U}} \qquad (5.3)$$

where the variable N_t is the trap density and E_U is the associated Urbach energy. Using Equation 5.3 as an ansatz for Equation 5.2 with the origin at the measured threshold voltage has the following analytical form,

$$V_G = \frac{N_t d_{org} q}{C_{ox}} \left(1 - e^{\frac{-qV_{CPD}}{E_U}}\right) + V_{CPD} \qquad (5.4)$$

The result of this fit calculation can be seen as the red line plotted in Figure 5.2, using fit parameters values of $E_U = 54.4 \pm 5.0$ meV and $N_t = (2.94 \pm 0.92) \times 10^{15}$ cm^{-3}. From the fit parameter, the characteristic temperature, T_0, is calculated to be 631 ± 58 K, a range which agrees well with transport measurements 6T 2D OFETs with similar fabrication.[7] Further analysis of the transfer characteristics shown in Figure 5.1b, using the 2D drain current approximation for large gate biases developed by Brondijk et al.[7], also yields a consistent characteristic temperature of 592 K.

Although there is debate in the OFET field regarding the analytic shape of the trap DOS,[34] our results can be fit by the assumed exponential DOS. These fit parameters compare well to most other KPFM trap DOS studies,[22, 23] but N_t is several orders of magnitude low compared DOS measurements by other transport experiments.[35] This order of magnitude is more in the range of trap DOS observed in the bulk of single crystal OSCs.[4] The discrepancy is perhaps due to the second monolayer acting to screen some of the charges from being observed

by the scan probe, which may account for KPFM trap DOS results with higher N_t that uses a SAM as the active layer.[19] Another possibility for the discrepancy in trap density is that transport measurements occur through the source-drain electrodes where traps are known to accumulate[28] which may not be observed in the local shifts in CPD in the center of the channel.

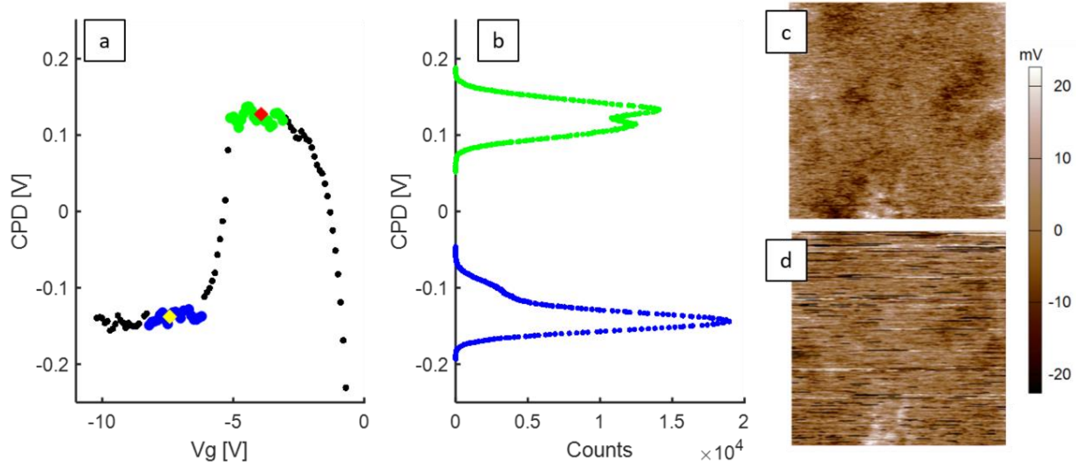

Figure 5.3: (a) Extended graph of measured average surface potential at each gate bias. (b) Compiled histograms of 20 images, each, where the green (blue) points correspond to the green (blue) highlighted points in (a). (c) and (d) are representative (8 μm)^2 surface potential images matching the red and yellow diamonds in (a), respectively.

Figure 5.3a extends the observed dependence of surface potential on gate bias, as described for main plot of Figure 5.2, to show the surface potential behavior before and after the transition region that is used to calculate the trap DOS. We assign 3 clear regimes to this graph: the 'off' regime from $V_G = 0$ V to -5.1 V, the trap regime analyzed in figure 2 from $V_G = -5.2$ V to -6.1 V, and the 'on' regime starting from $V_G = -6.2$ V. Under low gate bias the field induced in the active layer begins to draw in hole carriers to the trap states, which is reflected in the positive gradient observed. This trend stabilizes indicating that all trap states are filled prior to onset of

V_{th}. The point where the 6T HOMO is first accessed is V_G = -5.2 V, which we assign to be the threshold voltage. This value obtained from KPFM is in reasonable agreement with the threshold voltage value extrapolated from the transfer characteristics, V_G = -5.5 V, described in Section 5.2. As hole accumulation occurs in this transition region the observed surface potential becomes increasingly negative. This counterintuitive result makes sense in the context that the free charges being introduced in this region act to screen the charges in deep traps as described previously in EFM studies of the Marohn group.[36] After the transition states where trap DOS is calculated, the gate bias is continually screened by the free charges in the accumulation layer since the Fermi energy is situated directly in the HOMO band above the mobility edge.

Histograms of 20 images in the stable 'on' and 'off' regimes are shown in Figure 3b. Vertical axes of Figure 5.3a and 5.3b are set to the same range and the data points are color coded green (blue) for the 'on' ('off') regimes for easy comparison. The distribution of CPD from each KPFM images can be thought of as a sampling of the charge concentration at given gate bias. It is clear that right before threshold voltage, the green data points in Figure 5.3a, all deep trap states should be occupied prior to the onset of hole accumulation at the threshold voltage. In this 'off' regime near the depletion voltage two distinct peaks are observed in the green CPD histogram of Figure 5.3b. The more negative peak is assigned to be the work function of 6T while the more positive peak we assign to trapped charges. In the 'on' regime indicated by the blue data points in Figure 5.3a and 5.3b, there is a marked decrease in the peak associated with trapped charges. The persistence of a secondary peak in the blue CPD histogram of Figure 5.3b this is detrimental to charge transport since this is the regime of conduction. Figure 5.3b

histograms are both well fit by double Gaussian peaks separated by 0.028 (0.033) V for the 'off' ('on') regimes. This separation is in the range of k_BT indicating a relationship to thermal excitations. We note that in the transition regime the tendency towards single or double peaks in the CPD histograms switches between a double and single peak seemingly at random.

The most important new observation in these experiments is that, beginning in the transition regime and continuing throughout the 'on' state, the surface potential images appear markedly "noisier". Corresponding topography images do *not* show this tendency indicating that this is a purely electrostatic effect and not the tip quality degrading over time. We conclude that this imaging instability in the 'on' regime is due to charges trapping and de-trapping many times over the duration of a single scan. This is the same physical process leading to 1/f noise.[26, 27] Figures 5.3c and 5.3d are representative surface potential images from the 'off' and 'on' regimes respectively to show the onset of noise near threshold.

In the 'off' regime, the KPFM images do show some correlation for deep traps to accumulate at the incomplete third monolayer islands, visible as the dark spots in Figure 5.3c, but this is not a direct correspondence. The observation of inhomogeneous deep trap grouping is comparable to those found by the Marohn group's scanned probe investigations into deep traps under similar bias conditions,[36] which concludes that grain boundaries alone are not a predictor of charge trapping. As previously mentioned, from the shifting CPD histograms in Figure 5.3.b, it was determined that the influence of hole accumulation acted to screen the deep traps. It is these added carriers that contribute to the observed noise since they can be trapped and detrapped on time scales faster than the imaging time. The scans that visibly show the most noise occur

near threshold voltage, which is an observation in agreement with 1/f noise measurements related to gate bias dependence.[27] Our data showing the impact of coexisting free and trapped charges on surface potential enriches the known device data by providing a framework for future advances in mobility and DOS calculations.[1, 37]

5.4 Summary and Conclusions

Kelvin probe force microscopy (KPFM) was used in this research to measure surface potential distributions for a range of gate biases in an effort to investigate the electronic structure of an operational 2-dimensional organic field effect transistor (2D OFET) of α-sexithiophene (6T). The decision was made here to scan a large area of the surface of the active layer and then shift the applied biases, in lieu of the traditional method which is to measure the surface potential of a single point and shift the bias of the sample incrementally. This permitted the use of the standard deviation of CPD to quantify error in the trap DOS calculation. The transition between the 'on' and 'off' regimes of the active layers was used to compute the trap density of states (DOS). The experiment resulted in data showing the static nature of the 'off' regime with respect to the 'on' regime, which was relatively dynamic and shown to screen the presence of deep traps. We attribute noise observed in surface potential scans in the stable 'on' regime to active trapping and thermal release.

The data collected by this experiment yielded some interesting results that thus far have been primarily background in the reporting of results from other research projects.[36] This aspect of free charges screening the gate is a finding worth emphasizing as it is highly demonstrative of the dynamicity of shallow charge trapping. The gate bias dependent CPD histograms illustrate

the screening of deep traps by free carriers and the observed noise after threshold voltage implies active tunneling between localized and delocalized states. Coexisting carrier types such as this has precedence in literature in Hall transport measurements.[37] The impact of active trapping and detrapping of charges has precedent explaining 1/f noise observed in the drain current,[26, 27] but here it is related to the surface potential observed with KPFM, a connection that has not previously been made. Although 1/f noise shows dependence on the contacts under bias, the dynamics of trap and release are apparent from surface potential analysis indicating that this is an intermolecular effect intrinsic to the film's microstructure. Mitigating this 1/f noise by 'trap healing' has been shown in other reports[38] and exemplifies the importance of our results observing the effects of shallow trap dynamics for device optimization and theoretical considerations.[1, 37]

Acknowledgements

This study was funded by NSF CAREER award DMR-1056861.

5.5 Supplemental Material

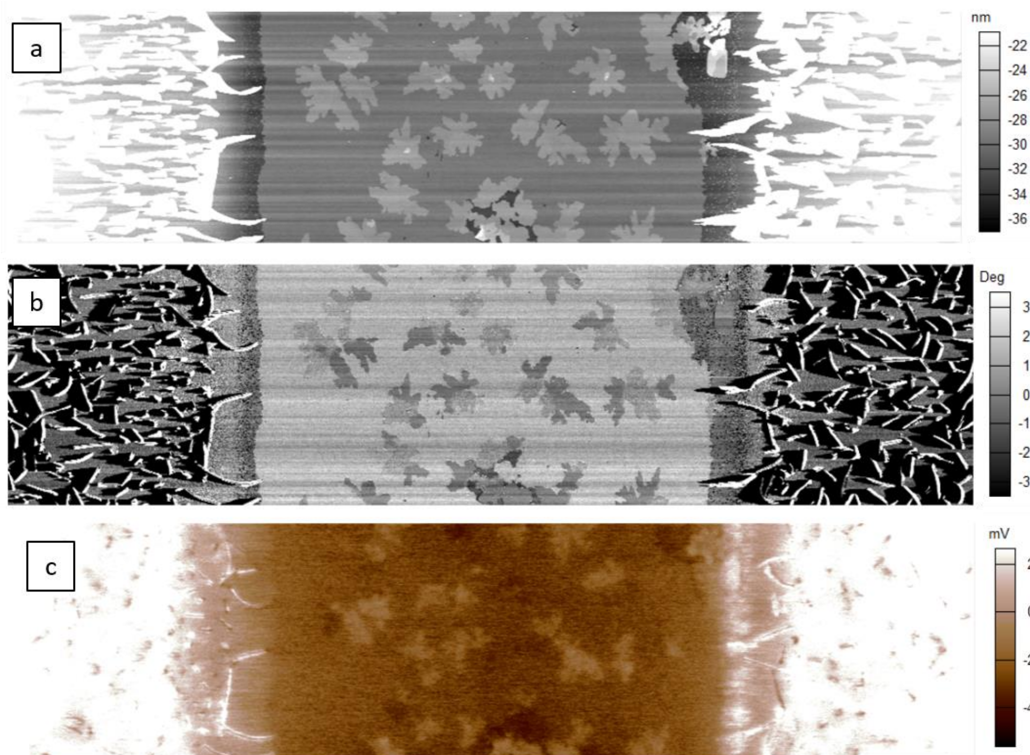

Figure 5.4: (a), (b), and (c) are 10x40 μm^2 images of topography, phase, and CPD, respectively, characterizing the length of the OFET channel at V_G = 0V.

In Figure 5.4 is a KPFM scan of the entire 6T OFET channel with V_G = 0 V. Figure 5.4a is of the topography shows uniform 6T coverage over the length of the entire channel with an apparent alternate growth mode of 6T occurring on top of the Au interface of the electrodes. Figure 5.4b depicts the phase contract of the film and Figure 4.4c is the surface potential. Note the unique light and dark regions of 6T in the islands that are an incomplete third monolayer within the channel which is observable in the phase and CPD, but not the topography. Such observed contrasts are similar to KPFM observations of bi-layer pentacene.[16] But, for our case the contrast seems likely to be due to 6T phase segregation.[12]

5.6 References

1. S. D. Baranovskii, Physica Status Solidi (b) **251** (3), 487-525 (2014).

2. N. Tessler, Y. Preezant, N. Rappaport and Y. Roichman, Advanced Materials **21** (27), 2741-2761 (2009).

3. V. Podzorov, E. Menard, J. A. Rogers and M. E. Gershenson, Physical Review Letters **95** (22), 226601 (2005).

4. W. L. Kalb, S. Haas, C. Krellner, T. Mathis and B. Batlogg, Physical Review B **81** (15), 155315 (2010).

5. F. Dinelli, M. Murgia, P. Levy, M. Cavallini, F. Biscarini and D. M. de Leeuw, Physical Review Letters **92** (11), 116802 (2004).

6. E. C. P. Smits, S. G. J. Mathijssen, P. A. van Hal, S. Setayesh, T. C. T. Geuns, K. A. H. A. Mutsaers, E. Cantatore, H. J. Wondergem, O. Werzer, R. Resel, M. Kemerink, S. Kirchmeyer, A. M. Muzafarov, S. A. Ponomarenko, B. de Boer, P. W. M. Blom and D. M. de Leeuw, Nature **455** (7215), 956-959 (2008).

7. J. J. Brondijk, W. S. C. Roelofs, S. G. J. Mathijssen, A. Shehu, T. Cramer, F. Biscarini, P. W. M. Blom and D. M. de Leeuw, Physical Review Letters **109** (5), 056601 (2012).

8. A. J. Kronemeijer, V. Pecunia, D. Venkateshvaran, M. Nikolka, A. Sadhanala, J. Moriarty, M. Szumilo and H. Sirringhaus, Advanced Materials **26** (5), 728-733 (2014).

9. G. Horowitz, D. Fichou, X. Peng, Z. Xu and F. Garnier, Solid State Communications **72** (4), 381-384 (1989).

10. B. Servet, G. Horowitz, S. Ries, O. Lagorsse, P. Alnot, A. Yassar, F. Deloffre, P. Srivastava and R. Hajlaoui, Chemistry of Materials **6** (10), 1809-1815 (1994).

11. A. O. F. Jones, B. Chattopadhyay, Y. H. Geerts and R. Resel, Advanced Functional Materials **26** (14), 2233-2255 (2016).

12. C. Lorch, R. Banerjee, C. Frank, J. Dieterle, A. Hinderhofer, A. Gerlach and F. Schreiber, The Journal of Physical Chemistry C **119** (1), 819-825 (2015).

13. L. Pithan, C. Cocchi, H. Zschiesche, C. Weber, A. Zykov, S. Bommel, S. J. Leake, P. Schäfer, C. Draxl and S. Kowarik, Crystal Growth & Design **15** (3), 1319-1324 (2015).

14. K. Cnops, B. P. Rand, D. Cheyns, B. Verreet, M. A. Empl and P. Heremans, Nature Communications **5**, 3406 (2014).

15. M. Nonnenmacher, M. P. O'Boyle and H. K. Wickramasinghe, Applied Physics Letters **58** (25), 2921-2923 (1991).

16. Y. Wu, G. Haugstad and C. D. Frisbie, The Journal of Physical Chemistry C **118** (5), 2487-2497 (2014).

17. B. C. Hoffman, T. McAfee, B. R. Conrad, M. A. Loth, J. E. Anthony, H. W. Ade and D. B. Dougherty, ACS Applied Materials & Interfaces **8** (33), 21490-21496 (2016).

18. O. Tal and Y. Rosenwaks, The Journal of Physical Chemistry B **110** (50), 25521-25524 (2006).

19. W. S. C. Roelofs, S. G. J. Mathijssen, R. A. J. Janssen, D. M. de Leeuw and M. Kemerink, Physical Review B **85** (8), 085202 (2012).

20. R. Häusermann, K. Willa, B. Blülle, T. Morf, A. Facchetti, Z. Chen, J. Lee and B. Batlogg, Organic Electronics **28**, 306-313 (2016).

21. S. Galindo, M. Ahmadpour, L. G. Gerling, A. Marsal, C. Voz, R. Alcubilla and J. Puigdollers, Organic Electronics **15** (10), 2553-2560 (2014).

22. O. Tal, Y. Rosenwaks, Y. Preezant, N. Tessler, C. K. Chan and A. Kahn, Physical Review Letters **95** (25), 256405 (2005).

23. S. Yogev, E. Halpern, R. Matsubara, M. Nakamura and Y. Rosenwaks, Physical Review B **84** (16), 165124 (2011).

24. Y. Zhang, D. Ziegler and M. Salmeron, ACS Nano **7** (9), 8258-8265 (2013).

25. A. McWhorter, Semiconductor Surface Physics, 207-228 (1957).

26. O. D. Jurchescu, B. H. Hamadani, H. D. Xiong, S. K. Park, S. Subramanian, N. M. Zimmerman, J. E. Anthony, T. N. Jackson and D. J. Gundlach, Applied Physics Letters **92** (13), 132103 (2008).

27. L. Ke, S. B. Dolmanan, L. Shen, C. Vijila, S. J. Chua, R.-Q. Png, P.-J. Chia, L.-L. Chua and P. K.-H. Ho, Journal of Applied Physics **104** (12), 124502 (2008).

28. Y. Xu, T. Minari, K. Tsukagoshi, J. Chroboczek, F. Balestra and G. Ghibaudo, Solid-State Electronics **61** (1), 106-110 (2011).

29. S. Kowarik, A. Gerlach and F. Schreiber, Journal of Physics: Condensed Matter **20** (18), 184005 (2008).

30. H. Gomes, P. Stallinga, F. Dinelli, M. Murgia, F. Biscarini, D. De Leeuw, T. Muck, J. Geurts, L. Molenkamp and V. Wagner, Applied Physics Letters **84** (16), 3184-3186 (2004).

31. A. Ortiz-Conde, F. J. García Sánchez, J. J. Liou, A. Cerdeira, M. Estrada and Y. Yue, Microelectronics Reliability **42** (4–5), 583-596 (2002).

32. H.-S. Wong, M. H. White, T. J. Krutsick and R. V. Booth, Solid-State Electronics **30** (9), 953-968 (1987).

33. M. C. J. M. Vissenberg and M. Matters, Physical Review B **57** (20), 12964-12967 (1998).

34. J. O. Oelerich, D. Huemmer and S. D. Baranovskii, Physical Review Letters **108** (22), 226403 (2012).

35. W. L. Kalb and B. Batlogg, Physical Review B **81** (3), 035327 (2010).

36. E. M. Muller and J. A. Marohn, Advanced Materials **17** (11), 1410-1414 (2005).

37. H. T. Yi, Y. N. Gartstein and V. Podzorov, Scientific Reports **6**, 23650 (2016).

38. B. Lee, Y. Chen, D. Fu, H. T. Yi, K. Czelen, H. Najafov and V. Podzorov, Nat Mater **12** (12), 1125-1129 (2013).

Chapter 6

Conclusions and Outlook

Because increasing the commercial viability of OSC devices has such potential in terms of low-energy production and novel devices, such as single monolayer transistors,[1] there has already been much research into optimizing figures of merit in these systems. Charge traps are a major form of interference that induce recombination, scattering centers, and diminishing mobility.[2] Previous research has identified several key sources of defects in the molecular structure of OSC materials that lead to such charge trapping, among them grain boundaries, chemical impurities, structural defects, and interfacial effects.[3, 4] Accounting for and minimizing all these defects has greatly improved the performance of OSC devices even without knowing the theoretical limit that these systems can be pushed towards. Still, charge traps are identified even within the highest preforming single crystal OSCs.[3, 5] The goal of this research is to begin to close the gaps in knowledge regarding influences and origins of charge trapping observed through surface potential distributions.

This research into charge trapping within organic semiconducting (OSC) films using scanning probe microscopy has allowed for several meaningful observations relevant to the organic electronics community. The first part of the research, growing diF-TES-ADT molecules[6] on silicon substrates with native oxide layers, allowed observation of the uniqueness in the variation on the surface potential of OSC crystallites as compared to the variations in the substrate. In thick films the chemical passivation of the substrate reduces the surface potential variations, parametrized by skew, and so the source of contact potential variations is assigned to

be intrinsic defects, as opposed to screening charges in the substrate oxide.[3] Distinguishing the origin of electronic disorder is important for effective mitigation and the methodology is a useful strategy for quantifying the effects of charge trapping.

The second part involved growing 1.5 monolayer films of α-sexithiophene (6T) on silicon substrates with a thick oxide layer at various temperatures. Relative surface potential variations found between the first and second layers of samples with lower substrate temperatures are inverted with respect to relative surface potential variations found between the two layers of samples with a higher substrate temperature. Grazing-incidence wide-angle x-ray scattering (GIWAXS) data collected on those films shows that there is no out-of-plane order for the lower temperature sample. We identify this out-of-plane disorder as the source of interlayer charge trapping between the first and second monolayers of the 6T films. This shows how subtle changes in processing can have dramatic effects on interlayer charging which is important for the potential impact on device performance and trap state calculations.[7]

The final research project involved scanning a large area of the surface of the active layer of 6T in a transistor and then shifting the applied gate bias in order to yield data relating to shallow charge trap states.[8] Trap density of states (DOS) computed from the mean and standard deviation of surface potential from each scan enabled calculation of the Urbach energy and trap density with quantified error. Surface potential data collected from that experiment led to the conclusion that charge trapping is a dynamic state for an operational transistor in the ‘on’ regime. Implications of this discovery have context toward establishing an electrical noise baseline in high performance transport experiments, e.g. recent Hall effect measurements.[9] Also, this

reinforces the coexistence of both free and trapped charges in the accumulation region, which is important for comparison between Hall and field effect mobilities.[10] Combined, these experiments identify some key physical effects of charge trapping as it relates to the interface between the OSC material and the substrate.

While the addition of this data to the growing body of research on the electronic properties of OSC materials will aid in the community's understanding of OSCs as a whole, there is still much work to be done with regards to the testing and analysis of the materials under different conditions, accounting for different variables and environments. While there may be fundamental limits to eliminating charge-trapping caused by the weak interactions that bind molecules together, there surely is room for improvement in the efficiency of charge transport. Experiments done under grounded gate bias conditions, such as clear evidence of orientation dependent work function[11] in polymorphic films or on the impact of structural defects on surface potential for relatively thick films would contribute further to our comprehension of charge trapping origins. Also, further temperature controlled transport measurements[12] in conjunction with the analysis techniques presented in Chapter 5 would be useful to cross-check the trap DOS calculation. Together this work contributed to the scientific community's conception of charge trapping in OSC materials observed through surface potential measurements, furthering the quest to mitigate their influence on charge transport.

6.1 References

1. E. C. P. Smits, S. G. J. Mathijssen, P. A. van Hal, S. Setayesh, T. C. T. Geuns, K. A. H. A. Mutsaers, E. Cantatore, H. J. Wondergem, O. Werzer, R. Resel, M. Kemerink, S. Kirchmeyer, A. M. Muzafarov, S. A. Ponomarenko, B. de Boer, P. W. M. Blom and D. M. de Leeuw, Nature **455** (7215), 956-959 (2008).

2. N. Tessler, Y. Preezant, N. Rappaport and Y. Roichman, Advanced Materials **21** (27), 2741-2761 (2009).

3. W. L. Kalb, S. Haas, C. Krellner, T. Mathis and B. Batlogg, Physical Review B **81** (15), 155315 (2010).

4. R. Noriega, J. Rivnay, K. Vandewal, F. P. V. Koch, N. Stingelin, P. Smith, M. F. Toney and A. Salleo, Nature Materials **12** (11), 1038-1044 (2013).

5. V. Podzorov, E. Menard, J. A. Rogers and M. E. Gershenson, Physical Review Letters **95** (22), 226601 (2005).

6. S. Subramanian, S. K. Park, S. R. Parkin, V. Podzorov, T. N. Jackson and J. E. Anthony, Journal of the American Chemical Society **130** (9), 2706-2707 (2008).

7. J. J. Brondijk, W. S. C. Roelofs, S. G. J. Mathijssen, A. Shehu, T. Cramer, F. Biscarini, P. W. M. Blom and D. M. de Leeuw, Physical Review Letters **109** (5), 056601 (2012).

8. O. Tal and Y. Rosenwaks, The Journal of Physical Chemistry B **110** (50), 25521-25524 (2006).

9. B. Lee, Y. Chen, D. Fu, H. T. Yi, K. Czelen, H. Najafov and V. Podzorov, Nat Mater **12** (12), 1125-1129 (2013).

10. H. T. Yi, Y. N. Gartstein and V. Podzorov, Scientific Reports **6**, 23650 (2016).

11. S. Duhm, G. Heimel, I. Salzmann, H. Glowatzki, R. L. Johnson, A. Vollmer, J. P. Rabe and N. Koch, Nature Materials **7** (4), 326-332 (2008).

12. W. L. Kalb and B. Batlogg, Physical Review B **81** (3), 035327 (2010).

Appendices

Appendix A

Glossary of Key Terms

Amorphous Solid: A solid with the absence of long-range order that characterizes a crystal. Often referred to as a glass.

Atomic Force Microscopy: A form of scanning probe microscopy where the force between sample and probe is observed through the flexural motion of a cantilever probe. Abbreviated as AFM

Band Gap: A term from electronic band structure that describes a range of energies that a electrons in a solid quantum mechanically not allowed to have.

Chemical Composition: For a single substance, this refers to the relative amounts of elements the substance consists of. For a mixture of substances, this refers to concentration of each component of the mixture.

Chemical Potential: Thermodynamic quantity referring to the change in internal energy due to a chemical reaction of phase transition. Defined to be equal to the Fermi level at zero Kelvin.

Conduction Band: The lowest unoccupied energy band situated above the Fermi level.

Contact Potential Difference: The electrostatic potential difference between points outside and near the surface of two metals. Abbreviated as CPD.

Crystal Growth: Process of crystallization after nucleation where atoms or molecules are added to the characteristic arrangement of the structure.

Crystal Phase: Different crystal structures in a polymorph solid.

Density of States: Parameter describing the number of states for an interval of energy that are available to be occupied per unit volume and energy. Abbreviated as DOS.

Electrostatic Force Microscopy: A mode of atomic force microscopy where a voltage bias is applied to a conductive cantilever probe to measure electrostatic attractive and repulsive forces related to charges in the sample. Abbreviated as EFM.

Energy Band: A term from electronic band structure that describes a range of energies that a electrons in a solid quantum mechanically allowed to have.

Exciton: An electronically neutral quasiparticle describing the bound state of an electron and hole attracted to one another through Coulombic interaction.

Field-Effect Transistor: A device which uses an electric field generated from a gate contact to control the conductivity between source and drain electrodes. Abbreviated as FET.

Fermi Level: The total chemical potential of the electrons. Associated with highest kinetic energy of electrons in a solid, but can be positioned within the band gap.

Grazing-Incidence Wide-Angle X-ray Scattering: Uses x-rays with a fixed angle of incidence to create diffraction peaks useful for crystallographic analysis. Abbreviated as GIWAXS.

Grain Boundary: Defects in crystal structure that is the interface between two crystallites in a polycrystalline material.

Highest Occupied Molecular Orbital: Roughly analogous to the valence band for inorganic semiconductors. Abbreviated as HOMO

Ionization Energy: The energy required to remove an electron leaving behind a cation.

Kelvin Probe Force Microscopy: A mode of atomic force microscopy where a dynamic electrical bias is applied to a conductive cantilever such that the electric field between tip and sample is minimized. Abbreviated as KPFM, KPM, or SKPM.

Light-Emitting Diode: A device which uses the recombination of electrons with holes to produce photons, a process known as electroluminescence, whose wavelength of is determined by the band gap of the semiconductor. Abbreviated as LED.

Lowest Unoccupied Molecular Orbital: Roughly analogous to the conduction band for inorganic semiconductors Abbreviated as LUMO.

Nucleation: Process of the first cluster forming toward crystal growth. Can be either heterogeneous or homogenous depending on if it forms from a surface defect.

Organic Compound: Molecules that are generally composed of Sulfur, Nitrogen, Oxygen, and in particular Carbon. All known living organisms are based on organic compounds.

Phase Transition: The transformation from one molecular structure to another.

Photovoltaics: A device which uses incident photons to excite electrons across the band gap and create an electric potential within the active material. Abbreviated as PV.

Polaron: A quasiparticle describing the interaction between electrons and atoms in a lattice as atoms shift from their equilibrium position and screen the electron. This generally increases effective mass of the electron and lowers its mobility.

Polymorphism: Refers to a crystalline solid with two or more distinct crystal structures.

Polycrystalline: A solid made up of many smaller crystallites of variable size and orientation. Also referred to as multicrystalline.

Scanning Probe Microscopy: A large branch of microscopy where a probe is used to form images of a sample surface topography by using a feedback loop to maintain a constant tip-sample distance as the probe raster scans the sample. Abbreviated as SPM.

Semiconductor: Materials with a Fermi level positioned within band gap such that it normally acts as an insulator but can be manipulated to behave as a conductor. The band gap of insulators is more wide than typical semiconductors and the Fermi level of conductors is positioned within an energy band.

Single Crystal: A solid with crystal lattice that extends unbroken to the edge of the sample with no internal grain boundaries. Also referred to as monocrystalline.

Surface Energy: Excess energy from the disruption of molecular bonds at the surface of a material compared to its bulk. Related to the work required to split a material creating two surfaces.

Texture: Degree of preferred orientation among a distribution of crystallites in a polycrystalline solid.

Valence Band: The highest occupied energy band situated above the Fermi level.

Work Function: The difference between the electrochemical potential within and the electrostatic potential outside of a material.

Appendix B

MATLAB Code for DOS Analysis in Chapter 5

This is all the code to make the Figures 5.2 and 5.3. In order to use this code I will assume that each of the KPFM images has been converted into .txt files. The first three programs are functions that should be stored in the main directory of MATLAB code. The fourth program is used to analyze all the data. Program 5 and 6 out Figures 5.2 and 5.3, respectively.

Program 1:

```
function [ po_re, po_name ] = pull_po( filename, horz_res,
tab_iter)
%pull_po For mass importing sections of matricies from .txt
files (tab
%delimited) from igor.
%   This program seperates the wanted tab of data (from the igor
exported
%   .txt file), returns it in addition to a nice name. tab_iter
referes to
%   the tab the data you want is on in igor.  vert_res referes
to the
%   number of lines the image was taken with.

% This work supported by NSF Career Award DMR -1056861.
%% Begin Code
% format long  % should a high precision be needed, uncomment
this command
%% Seperate out the wanted data
t = load(filename);
% where does the wanted data begin?
begin = horz_res*(tab_iter-1);
% Do the matrix concatenation
po_re = t((begin+1):(begin+horz_res),:);
```

```
%% Make the caller a nice variable name to go with it
hld = strsplit(filename, '.');
po_name = strcat('po_', hld(1,1));

end
```

Program 2:

```
function [dataA, stdA] = data_std(A, square,limited_len,
pointAx, pointAy,DriftStart,DriftFinish)
%DATA_STD Works in conjunction with test2 to gather data, find
st. dev. and
%perform avg on points from kpfm endgame DOS
%   Detailed explanation goes here

%% Create array for data from pointA
dataA = zeros(1,limited_len);
% Create array for st. dev from pointA
stdA = zeros(1,limited_len);

%Linear Drift Stuff
LDx = int16(linspace(DriftStart(1),DriftFinish(1),limited_len))-
DriftStart(1);
LDy = int16(linspace(DriftStart(2),DriftFinish(2),limited_len))-
DriftStart(2);

% Average a square of points with PointA in the upper left
points = zeros(1,square*square); % create an array to hold the
points per image that will be averaged.
for i = 1:limited_len  %iterate through all the images
    l = 1; % start a counter for the array of averages
    for j = 0:square-1
        for k = 0:square-1
            points(l) = A(pointAx+j+LDx(i), pointAy+k+LDy(i),
i);
            l = l+1;
        end
    end
    dataA(i) = sum(points);
    dataA(i) = dataA(i)/(square*square);
    stdA(i) = std(points);
end
end
```

Program 3:

```
function [ master, names, num_images ] = batch_pull_po_ui()
%batch_pull_po_ui Function Does the same as batch_pull_po but
with a UI
%rather than being all command line based
% Function extracts a folders .txt data into MatLab
%   Master contains all the matricies, names contains the names
of the
%   files that have been added, num_images is exactly what you
think it is.
%% dependacies
    % pull_po()
%It extracts a folders .txt data into MatLab using pull_po()
%   See notes on pull_po(), this is an addition to that that
does that for
%   an entire folder and names things appropriately.
%example batch_pull_po('C:\Documents and
Settings\computation\Desktop\testfolder', 512, 10)

% This work supported by NSF Career Award DMR -1056861.

%% Begin Code
waitfor(msgbox('The entire folder you select next prompt will be
added to the workspace.  Be sure only the neccesary files are in
the folder.','Caution: This may take awhile'));
pause(.01);

% ui input for path
k = 1;
while k >= 1
    [FileName,path] = uigetfile('*.txt','Select a file inside
the folder which contains the .txt igor files.');
    if k ==2  %provide an early termination path
        fprintf('Alright.  Exiting requested fucntion.\n')
        return
    elseif FileName == 0
       f = errordlg('You have to select a file in a folder...
It doesn''t matter which file inside the folder you pick, the
file path is all I care about.','Hey now...');
       waitfor(f);
       k =k+1;
    else break;
```

```
    end
end

x = inputdlg('What tab in Igor was the Potential data on?', 'Tab
in Igor', [1,40], {'10'});
tab_iter = str2double(x);

x = inputdlg(sprintf('You may have to go back and check the file
in Igor. \n1. Open the file in igor (full AFM version)\n2. In
the window of height trace, click on the "N" \n3. Report the
number under "ScanLines"'), 'Igor Lines', [1,40], {'64'});
vert_res = str2double(x);

x = inputdlg(sprintf('You may have to go back and check the file
in Igor. \n1. Open the file in igor (full AFM version)\n2. In
the window of height trace, click on the "N" \n3. Report the
number under "ScanPoints"'), 'Igor Points', [1,40], {'256'});
horz_res = str2double(x);

clear vars x
% we are now finished grabbing the inputs
%%
cd(path); % change directory back to where we started
strut = dir('*.txt');
len = length(strut);


%% time warning
if (len>=50)
    time = len*0.5/60;
    f = warndlg(strcat('You have more than 50 items, this could
take more than  ', num2str(time), ' min at 0.5 seconds per
item.'),'Caution');
    waitfor(f);
    pause(.01);
else
end
tic
%% Do the job
master = zeros(horz_res, vert_res, len); % create an array to
hold all the matricies
names = cell(1,len); % create an array to hold all the image
names
```

```
for i = 1:len
    fprintf('Extracting %s \n', strut(i,1).name);
    try
        [a1,a2] = pull_po(strut(i,1).name, horz_res, tab_iter);
%a1 returns with matrix
    catch ME
        if (strcmp(ME.identifier,'MATLAB:badsubscript')) % catch
an error and suggest to the user the cause
            f = errordlg('There appears to be a .txt igor file
with a different number of columns.  Make sure all the tune igor
files have been removed.  Also, verify all data was taken at the
same resolution. Remove all files that do not conform to this
and re-run the program.', 'Error in pull_po: scan points
error');
            waitfor(f)
            rethrow(ME)
        end
    end
    a2 = strcat(a2);
    names(i) = a2; % add the name to the cell array 'names'
    try
        master(:,:,i) = a1;
    catch ME
        if
(strcmp(ME.identifier,'MATLAB:subsassigndimmismatch')) % catch
an error and suggest to the user the cause
            f = errordlg('There appears to be a .txt igor file
with a different number of rows.  Make sure all the tune igor
files have been removed.  Also, verify all data was taken at the
same resolution. Remove all files that do not conform to this
and re-run the program.', 'Error in pull_po: scan lines error');
            waitfor(f)
            rethrow(ME)
        end
        if
(strcmp(ME.identifier,'MATLAB:load:numColumnsNotSame')) % catch
an error and suggest to the user the cause
            f = errordlg('There appears to be a .txt igor file
with an inconsistent number of columns.  Make sure all the tune
igor files have been removed.  Also, verify all data was taken
at the same resolution. Remove all files that do not conform to
this and re-run the program.', 'Error in batch_pull_ui: scan
columns error');
```

```
            waitfor(f)
            rethrow(ME)
        end
    end
    fprintf('Done\n')
    pause(0.01)
end
num_images = len;
fprintf('\nHey hey! Finished!\n')
fprintf('Returning %d items.\n', len)
toc
fprintf('That''s %d seconds per item.\n', toc/len)
end
```

Program 4:

```
%% Generate Data

% calculate the DOS info from a KPFM voltage bias run
% prgram will load necessary files from igor .txt files
% This work supported by NSF Career Award DMR -1056861.

clearvars -except A B len % reset most variables
close all % close any open plots

%% Define for Vg_CPD
%pointAx = 63;
%pointAy = 63;
%square = 3;
ImSq = 256;          % P&L Resolution
ScSz = 8;                    %units of micrometer

PointX = 128;
PointY = 128;
SqSz = 124;                        %Square Size 'Integer'
V_start = 0; % starting voltage in kpfm sweep
V_end = -20;
%name_output = sprintf('[%d,%d]',PointX,PointY);

DriftStart = [86,168];
DriftFinish = [85,166];

pointAx = PointX - SqSz;  %point to be monitored
```

```
pointAy = PointY - SqSz;
square = 2*SqSz+1;  % average the point A with sides of length
"square" w/ the point in the upper left
Perc = 100*(square^2)/(ImSq^2);  % percent of image
Area = ScSz*square/ImSq;

%% import data using batch_pull_poX
% line below runs only if A, B, or len does not exist to prevent
having to
% reimport variables and take up lots of time. Use clearvars to
clear all
% variables if necessary.
if (exist('A', 'var')==0) || (exist('B', 'var')==0) ||
(exist('len', 'var')==0)  % run this code only if A, B, or len
does not exist
    [A,B,len] = batch_pull_po_ui();
end

%% Find desired point in Data set (A)
V = linspace(V_start,V_end, len); % create array for gate bias
% find data for point A: uses data_std.m file/function

try % grab the data for point A (out of the A matrix) and check
to make sure it is inside the data set
    [dataA, stdA] = data_std(A, square, len, pointAx,
pointAy,DriftStart,DriftFinish);
catch ME
    if (strcmp(ME.identifier,'MATLAB:badsubscript')) % catch an
error and suggest to the user the cause
        k = size(A);
        f = errordlg({['The point entered for A appears to be
out of the range of the matrix of aquired data.  Reduce this (x
=' num2str(pointAx) ',y =' num2str(pointAy) ' ) coordinate to be
inside the (scanlines = ' num2str(k(1)) ', scanpoints = '
num2str(k(2)) ') range.'],  ['Note: range may also be exceeded
when doing square averaging.']}, 'Error: Point A Out of Range');
        waitfor(f)
        clear vars k
    end
    rethrow(ME)
end

%% Normalize Data
```

```
Vg_CPD(:,1) = V; % correct names to confirm
Vg_CPD(:,2) = dataA;
Vg_CPD(:,3) = stdA;
```

Program 5:

```
%% Vg_CPD graph with exp DOS fit and DOS inset

clearvars -except A B len Vg_CPD % reset most variables
close all % close any open plots

%% CPD Plot Data

close all
figure('color','w')
hold on

pt_i = 53;          %range start values
pt_f = 62;          %range final value
%pt_h = 48;         %highlights point
Vg_off = 5.2;       %offset value
CPD_off = 0.0801;   %offset value

%DTitle  = title ('Figure');
%DXLabel = xlabel('Vg [V]');
%DYLabel = ylabel('CPD [V]');

%% Fit Parameters

clearvars VG E E_g g der

N_t = 2.4e15;
E_u = 0.053;
VG(1) = -0.9;

E_i = -0.2;        %start CPD
E_f = 0;            %end CPD
step = 0.001;

n_nu = pt_f - pt_i +1 ;       % # of observed points
m_nu = 3;        % # of fit parameters

%% Other Parameters
```

```
Vg_nrm = Vg_CPD(pt_i:pt_f,1)+Vg_off;
CPD_nrm = (-1)*(Vg_CPD(pt_i:pt_f,2)+CPD_off);
variance = Vg_CPD(pt_i:pt_f,3).^2;
img_num = pt_f-pt_i + 1;

C_ox = 1.151e-4;
d_org = 5e-9;
q = 1.6e-19;
k = 1.4e17;
%conversion = 1.6e-19;
conversion = (1e-6)*(1.6e-19);
prefactor = C_ox/(d_org*q^2);

%% Calculate DOS

dVg = diff(Vg_nrm);
dSP = diff(CPD_nrm);
SP_DOS(:,1) = CPD_nrm(1:end-1)+dSP/2;

DOS = conversion*prefactor*(((dSP./dVg).^(-1))-1);
SP_DOS(:,2) = DOS;

%% Assumed Function

E = (E_i:step:E_f);
E_g = (E_i+step/2:step:E_f+step/2);
sz_E = size(E);
g = N_t/E_u*exp(-E_g/E_u);
der = g/(prefactor*conversion) + 1;
for i=2:sz_E(2)
    VG(i,1)=VG(i-1,1)+(der(i)*(E(i)-E(i-1)));
end

%% Reduced Chi Squared

chi_sqr = 0;

for j =1:img_num
    tmp = abs(VG-Vg_nrm(j));
    [idx idx] = min(tmp);
    chi_sqr = chi_sqr + ((CPD_nrm(j)-E(idx))^2)/(variance(j));
end
```

```
nu = n_nu - m_nu;
RCSS = chi_sqr/nu;

%% CPD Data

%D = line(Vg_CPD(pt_i:pt_f,1),Vg_CPD(pt_i:pt_f,2));
%D = errorbar(Vg_CPD(pt_i:pt_f,1)+Vg_off,(-
1)*(Vg_CPD(pt_i:pt_f,2)+CPD_off),Vg_CPD(pt_i:pt_f,3));
D = errorbar(Vg_nrm,CPD_nrm,Vg_CPD(pt_i:pt_f,3));
D.LineStyle = 'none';
D.Marker = '.';
D.MarkerSize = 18;
D.Color = 'k';
D.LineWidth = 1;

%% Fit Data

Dfit = line(VG,E);
%Dfit.Marker = 'o';
%Dfit.MarkerSize = 15;
Dfit.LineWidth = 2;
Dfit.Color = 'r';
%legend('fitted points','fit line');

%% Axis Properties

ax1 = gca;
ax1.LineWidth = 1.8;
%ax.YScale = 'log';
ax1.XMinorTick = 'off';
ax1.YMinorTick = 'off';
ax1.YGrid = 'on';
ax1.FontSize = 15;
%ax.XLim = [-8.5 -3];
%ax.YLim = [-0.13 0.15];

%set(gcf, 'PaperPositionMode', 'auto'); %does something?

%% Inset plot of trap DOS

axes('Position',[.30 .65 .25 .25])
box on
```

```
E = line(SP_DOS(:,1),SP_DOS(:,2));
%E.LineStyle = 'none';
E.LineWidth = 2;
%E.Marker = '.';
%E.MarkerSize = 12;
%E.Color = 'k';

ax2 = gca;
ax2.LineWidth = 1.5;
ax2.YScale = 'log';
ax2.XMinorTick = 'off';
ax2.YMinorTick = 'on';
ax2.XGrid = 'off';
ax2.FontSize = 12;
ax2.XLim = [-0.225 0.025];
ax2.YLim = [2e16 1e19];
```

<u>Program 6:</u>

```
%% Vg_CPD Graph with CPD Histograms

pt_i = 53;      %defines transition region
pt_f = 62;
del = 20;       %points outside transition region

%% Generate Histogram

pt_trap = (pt_i:pt_f);    %traps points
h = histogram(A(:,:,pt_trap));
hx = -1*(h.BinEdges(1:end-1) + diff(h.BinEdges)/2);
hy = h.Values;

pt_H = ((pt_f+1):(pt_f+del+1));
hH = histogram(A(:,:,pt_H));
hHx = -1*(hH.BinEdges(1:end-1) + diff(hH.BinEdges)/2);
hHy = hH.Values;

pt_L = (pt_i-del-1:pt_i-1);
hL = histogram(A(:,:,pt_L));
hLx = -1*(hL.BinEdges(1:end-1) + diff(hL.BinEdges)/2);
hLy = hL.Values;
```

```
%% Plot Histogram

close all
Fig = figure('color','w');
Fig.Position = [150 100 900 500];
hold on

subplot(1,2,2)
DXLabel = xlabel('Counts');
DYLabel = ylabel('CPD [V]');
%DTitle  = title ('Figure');

%g = line(hy,hx);
%g.LineStyle = 'none';
%g.Marker = '.';
%g.MarkerSize = 15;
%g.Color = 'r';
%g.LineWidth = 1;

gH = line(hHy,hHx);
gH.LineStyle = 'none';
gH.Marker = '.';
gH.MarkerSize = 15;
gH.Color = 'b';
gH.LineWidth = 1;

gL = line(hLy,hLx);
gL.LineStyle = 'none';
gL.Marker = '.';
gL.MarkerSize = 15;
gL.Color = 'g';
gL.LineWidth = 1;

ax = gca;
ax.LineWidth = 1.8;
%ax.YScale = 'log';
ax.XMinorTick = 'off';
ax.YMinorTick = 'off';
ax.XGrid = 'off';
ax.FontSize = 15;
%ax.XLim = [-0.2 0.2];
ax.YLim = [-0.25 0.25];
```

```
%% Plot CPD Data

subplot(1,2,1)
hold on

pt_vi = 6;  %range start values
pt_vf = 103;  %range final value

%DTitle  = title ('Figure');
DXLabel = xlabel('Vg [V]');
DYLabel = ylabel('CPD [V]');

%% DOS Data
%k=1000 %scake x-axis
D = line(Vg_CPD(pt_vi:pt_vf,1),-1*Vg_CPD(pt_vi:pt_vf,2));
%D =
errorbar(Vg_CPD(pt_i:pt_f,1),Vg_CPD(pt_i:pt_f,2),Vg_CPD(pt_i:pt_
f,3));
D.LineStyle = 'none';
D.Marker = '.';
D.MarkerSize = 18;
D.Color = 'k';
D.LineWidth = 1;

%% Highlight Point

%D_h = scatter(Vg_CPD(pt_trap,1),Vg_CPD(pt_trap,2));
%D_h.Marker = 'o';
%D_h.MarkerFaceColor = 'r';
%D_h.MarkerEdgeColor = 'r';
%D_h.SizeData = 80;

D_hH = scatter(Vg_CPD(pt_H,1),-1*Vg_CPD(pt_H,2));
D_hH.Marker = 'o';
D_hH.MarkerFaceColor = 'b';
D_hH.MarkerEdgeColor = 'b';
D_hH.SizeData = 60;

D_hL = scatter(Vg_CPD(pt_L,1),-1*Vg_CPD(pt_L,2));
D_hL.Marker = 'o';
D_hL.MarkerFaceColor = 'g';
D_hL.MarkerEdgeColor = 'g';
D_hL.SizeData = 60;
```

```
D_h1 = scatter(Vg_CPD(40,1),-1*Vg_CPD(40,2),'filled');
D_h.Marker = 'o';
D_h.MarkerFaceColor = 'k';
D_h.MarkerEdgeColor = 'k';
D_h.SizeData = 80;

D_h2 = scatter(Vg_CPD(75,1),-1*Vg_CPD(75,2),'filled');
D_h.Marker = 'o';
D_h.MarkerFaceColor = 'k';
D_h.MarkerEdgeColor = 'k';
D_h.SizeData = 80;

%% Axis Properties

ax = gca;
ax.LineWidth = 1.8;
%ax.YScale = 'log';
ax.XMinorTick = 'off';
ax.YMinorTick = 'off';
ax.XGrid = 'off';
ax.FontSize = 15;
ax.XLim = [-11 0];
ax.YLim = [-0.25 0.25];

%set(gcf, 'PaperPositionMode', 'auto'); %does something?
```